2014

# Synthesis, Characterization, and Theoretical Studies of Fluorescent GUMBOS and NanoGUMBOS

Chengfei Lu
*Louisiana State University and Agricultural and Mechanical College*, clu2@lsu.edu

SYNTHESIS, CHARACTERIZATION, AND THEORETICAL STUDIES OF
FLUORESCENT GUMBOS AND NANOGUMBOS

A Dissertation

Submitted to the Graduate Faculty of the
Louisiana State University and
Agricultural and Mechanical College
in partial fulfillment of the
requirements for the degree of
Doctor of Philosophy

in

The Department of Chemistry

by
Chengfei Lu
B.S., East China Normal University, 2001
M.M., Shanghai Jiao Tong University, 2006
August 2014

*To my wife, Yujie Wang, for her support, encouragement and steadfast love.*

*To my mother, Zhongying Tao, and my sublings, Hui Lu, for their support over the years.*

*To my parents-in-law, Kaihua Wang and Mingfeng Gao, for their trust and support.*

*To my daughter, Daisy W. Lu*

# ACKNOWLEDGMENTS

I am truly grateful to the following people for their generosity and support:

I sincerely thank my major professor, Prof. Isiah M. Warner, for his guidance, encouragement and patience throughout this project.

I thank my Ph.D. committee members: Profs. Samuel D. Gilman, Kermit Murray, Donghui Zhang, Giovanna Aita, and Kenneth A Lopata for their time and helpful suggestions regarding this dissertation.

Dr. Susmita Das, Dr. Min Li, and Dr. Noureen Siraj, for sharing their knowledge with me. Thank you for the helpful discussions and review of my manuscripts.

Dr. Cheri McFerrin and Dr. Lucy W. Kiruri for sharing their knowledge of computational chemistry with me.

Dr. Bilal El-Zahab, Dr. Farhana Hasan, Dr. Priyadarshini Pathak and Dr. Paul K. S. Magut for their time, support, and helpful suggestions regarding this dissertation work.

Dr. Ning Deng, Dr. Chun Wang, and Dr. Fangzhi Huang for their support and discussion.

Warner Research Group for their dynamic discussions, support, and friendship over the years.

# TABLE OF CONTENTS

# LIST OF ABBREVIATIONS

| Abbreviation | Name |
| --- | --- |
| AOT | sodium bis(2-ethylhexyl)sulfosuccinate |
| BETI | bis(perfluoroethylsulfonyl)imide |
| bmim | 1-Butyl-3-methylimidazolium |
| BSA | bovine serum albumin |
| CCD | charge-coupled device |
| CD | circular dichroism |
| CGMD | coarse grain molecular dynamics |
| CGTO | contracted Gaussian type orbitals |
| CI | carbazole-imidazolium |
| $Col_h$ | hexagonal columnar |
| DCM | dichloromethane |
| DFT | density functional theory |
| DSC | differential scanning calorimetry |
| Dy | dysprosium |
| EA | electron affinity |
| EDG/EWG | electron donating/withdrawing groups |
| ESP | electrostatic potential surfaces |
| ETL | electron-transporting layers |
| eV | electron volt |
| GTO | Gaussian type orbitals |

| | |
|---|---|
| GUMBOS | group of uniform materials based on organic Salts |
| $H_{cf}$ | crystal field |
| $H_{ee}$ | electron-electron interaction |
| HF | Hartree- Fock |
| HOMO | highest unoccupied molecular orbital |
| $H_{so}$ | spin-orbit coupling |
| HTL | hole-transporting layers |
| ICG | indocyanine green |
| ICT | intramolecular charge transfer |
| ILCs | ionic liquid crystals |
| ILs | ionic liquids |
| IP | ionization potential |
| L-CPL | left-handed circularly polarized light |
| $Ln^{III}$ | trivalent lanthanide ions |
| LUMO | lowest unoccupied molecular orbital |
| MD | molecular dynamics |
| MFILCs | multi-functional ionic liquid crystals |
| MOs | molecular orbitals |
| MTT | 3-(4,5-dimethylthiazol-2-yl)-2,5-diphenyltetrazolium bromide |
| N | nematic |
| $N_{col}$ | columnar nematic |
| $N_D$ | discotic nematic |

| | |
|---|---|
| NIR | near-infared |
| NMR | nuclear magnetic resonance |
| $NTf_2$ | bis(trifluoromethanesulfonyl)imide |
| OLEDs | organic light-emitting diodes |
| OTf | trifluoromethane sulfonate |
| PCM | polarized continuum model |
| PEG | polyethylene glycol |
| $PF^{6-}$ | hexafluorophosphate Ion |
| POM | polarized optical microscopy |
| R-CPL | right-handed circularly polarized light |
| SCN | thiocyanate |
| Sm | smectic |
| SmA | smectic A |
| $SmA_2$ | smectic $A_2$ |
| SmB | smectic B |
| SmC | smectic C |
| SmT | smectic T |
| SQUID | superconducting Quantum Interference Device |
| STO | slater type orbitals |
| TDDFT | time-dependent density functional theory |
| TEM | transmission electron microscopy |
| $\mu_{eff}$ | effective magnetic moment |

# ABSTRACT

In this dissertation, novel fluorescent materials, which are referred to as a **g**roup of **u**niform **m**aterials **b**ased on **o**rganic **s**alts (GUMBOS) are synthesized, characterized, and studied for different applications. GUMBOS are solid state organic salts having melting points from 25 ℃ to 250 ℃. Similar to ionic liquids, GUMBOS are highly tunable and can be designed for specific applications by incorporating multiple-functions into a single ion pair by selection of cation-anion combinations.

Chapter 2 is a discussion of the synthesis and characterization of a PEGylated IR786 GUMBOS. These GUMBOS are prepared by a two-step synthesis procedure followed by a facile anion exchange approach. These GUMBOS were found to form nano- and meso-scale GUMBOS in aqueous solution via self-assembly. Optical properties of nano- and meso-scale GUMBOS were investigated and results indicate that anions, such as $NTf_2$ and AOT, play a significant role in improving the photostability of PEG786 GUMBOS. In addition, these nano- and meso-scale GUMBOS resist nonspecific binding to proteins. PEGylation of the original IR786 leads to reduced cytotoxicity.

Chapter 3 is a discussion of preparation and characterization of multifunctional ionic liquid crystals composed of (-)-N-Methylephedrine ((-)MeEph) based cation and dysprosium based anion. The cation is obtained by covalently linking an alkyl chain to the nitrogen of (-)MeEph and the anion is a complex consisting of $Dy^{3+}$ and $SCN^{-1}$. The (-)MeEph based cation provides the compounds with mesomorphic and chiral properties, and the anion affords paramagnetism and luminescence. These compounds are found to exhibit enhanced luminescence intensities in a liquid crystalline state.

In chapter 4, theoretical studies of carbazole-imidazolium based GUMBOS are performed to investigate the electronic and photophysical properties. In particular, Density Functional Theory (DFT) is used to optimize the geometry of these GUMBOS at ground state, while Time Dependent Density Functional Theory (TDDFT) is used to calculate the optical properties of GUMBOS. Studies demonstrate that anions play an important role in determining the geometries of GUMBOS, and in turn affect the HOMO and LUMO configurations as well as electronic and optical properties.

# CHAPTER 1 INTRODUCTION

## 1.1 Ionic Liquids

Ionic liquids (ILs) are low melting point (<100℃) organic salts composed entirely of ions, which make them highly tunable for specific applications.[1, 2, 3, 4] ILs possess a number of unique properties, including negligible vapor pressure, good thermal stability, wide liquid temperature range, considerable electric conductivities, wide electrochemical window, and enhanced solvation interactions with both polar and nonpolar compounds. Due to their unique and advantageous properties, ILs have been widely studied for a variety of applications (figure 1.1) .[5]

**Analytics:**
- Matrices for mass spectrometry
- Gas chromatography column
- Stationary phase of HPLC

**Solvents:**
- Organic reaction and catalysis
- Biocatalysis
- Nanoparticle synthesis
- Polymerization
- Extraction

**Electrochemistry:**
- Electrolyte in batteries
- Metal plating
- Solar panels
- Fuel cells
- Ion repulsion

**Heat Storage:**
- Thermal fluids

**Application of Ionic Liquids**

**Liquid crystals:**
- Displays

**Engineering:**
- Coating
- Lubricants
- Plasticisers
- Dispersing agents

**Biological uses:**
- Biomass processing
- Drug delivery
- Biocides
- Personal care

**Physical chemistry:**
- Thermodynamic
- Refractive index
- Binary and ternary systems

Figure 1. 1 Application of ionic liquids in chemistry and industry

The first reported ionic liquid was synthesized in 1914 by Paul Walden, who neutralized ethylamine with concentrated nitric acid to produce a low melting point salt, ethylammonium nitrate ($[EtNH_3][NO_3]$), with a melting point of 12°C.[6] However, ionic liquids did not receive much attention in the first few decades after they were discovered. During the 1970s and 1980s, imidazolium and pyridinium cation based ionic liquids were initially developed and used as electrolytes for battery applications.[7, 8] In the mid-1980s, Fry et al.[9] and Boon et al.[10] utilized low melting point salts as solvents for organic reaction media. Since then, studies on ILs became widespread and the term "ionic liquids" was officially assigned to the low melting salts which have melting points at or below 100 °C.

Compared to conventional high-melting inorganic salts, ILs almost always have a bulky organic ion as either the cation or anion, which serves as a asymmetry-breaking moiety to lower the melting point of the resulting salt.[5] Typical cations, which are used to construct ILs, include alkyl-substituted imidazolium, pyridinium, ammonium, or phosphonium groups. While the anions are mostly inorganic, such as tetrafluoroborate ($BF_4$), and hexafluorophosphate ($PF_6$), organic anions are also common, like bis[(trisfluoromethyl)sulfonyl]amide ($NTf_2$) and trifluoromethane sulfonate (OTf). Because of the numerous combinations of cations and anions available, ILs has been regarded as "designer" compounds. Cations and anions that are commonly used in ILs are listed in Figures 1.2 and 1.3.[11]
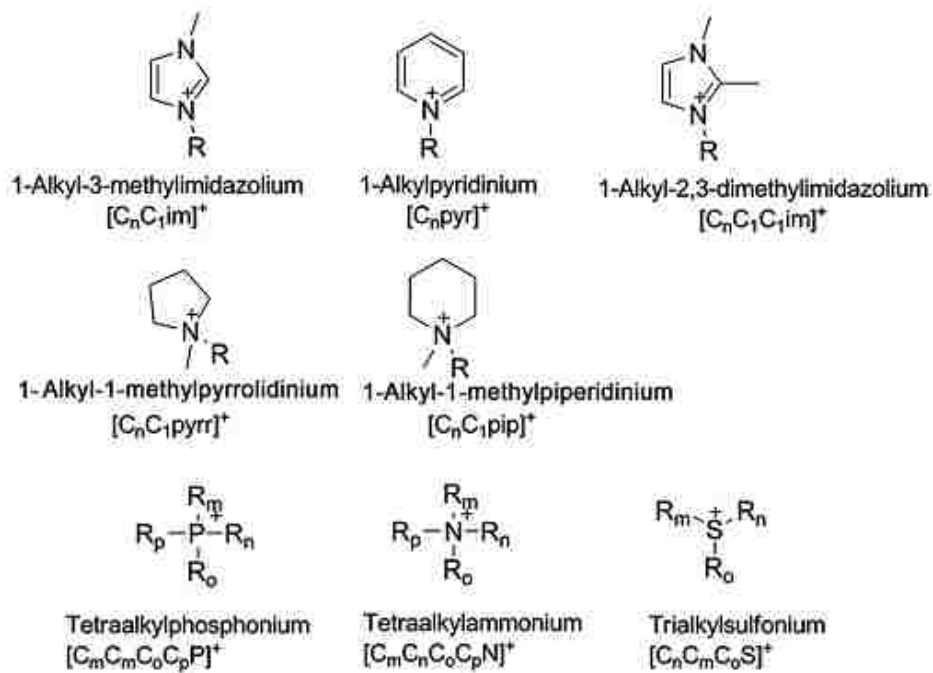
Figure1. 2 Structures and abbreviations of some common cations in ionic liquids
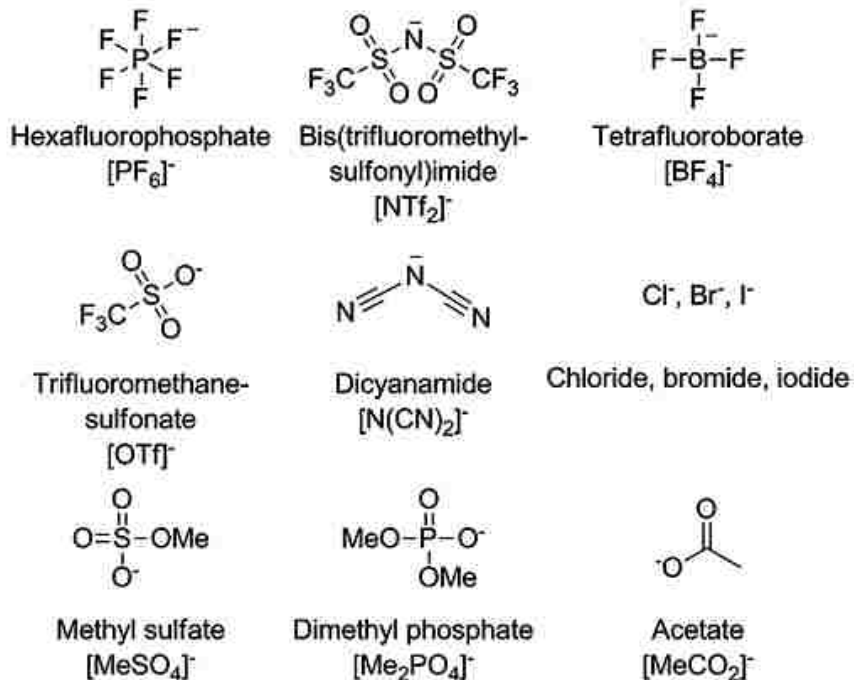


Figure1. 3 Structures and abbreviations of some common anions in ionic liquids

3

## 1.2 A Group of Uniform Materials Based on Organic Salts (GUMBOS)

The conventional definition of ILs sets an upper boundary for the melting point, which has limited the studies of organic salts containing melting points higher than 100 ℃. These solid organic salts also have many attractive properties similar to those of ILs and are tuned to exhibit multifunctional properties based on the selected cation and anion. Furthermore, solid organic salts have some advantages as compared to conventional ILs in developing nano-scale materials. The Warner research group has recently developed a class of materials referred to as a **g**roup of **u**niform **m**aterials **b**ased on **o**rganic **s**alts (GUMBOS), which includes the organic salts having melting points between 25-250 ℃ (Figure 1.4). This definition partially includes ILs (25 -100 ℃) and solid organic salts with melting points ranging from 100 to 250 ℃. The first reported GUMBOS and nanoGUMBOS (nanoparticles synthesized from GUMBOS) were developed by Tesfai et al.[12] They synthesized GUMBOS and nanoGUMBOS that were composed of 1-butyl-2,3-dimethylimidazolium [$Bm_2Im$]  as a cation and $BF_4$ and tetrachloroferrate [$FeCl_4$] as anions. Their study demonstrated the tunability of GUMBOS through careful selection of anions, in which magnetic GUMBOS were developed using $FeCl_4^-$ as an anion. Thus, varying ion pairs provides GUMBOS with unique properties and offers them as potential candidates for biomedical imaging,[13, 14] antibacterial agents,[15] drug delivery vehicles,[16] tumor therapy,[17, 18] optoelectronic,[19, 20] and light harvesting[21, 22, 23] applications.
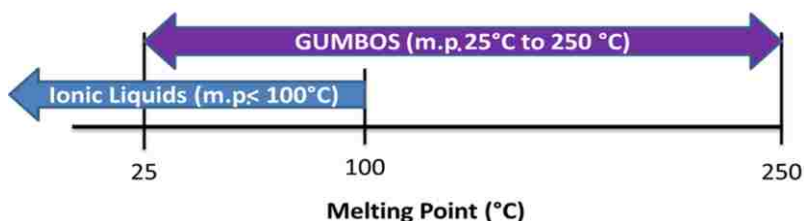


Figure1. 4 Temperature difference between ionic liquids and GUMBOS

**1.3 Fluorescent GUMBOS**

As mentioned previously, GUMBOS are tunable and hence can be designed to exhibit desirable properties based on selected ion pairs. Therefore, GUMBOS can also be developed to have fluorescence properties by employing either fluorescent cations or anions. In section 1.3 and 1.4, a discussion of background information on fluorescence spectroscopy and fluorescent GUMBOS based on cyanine dyes, lanthanide ions, and carbazole is presented.

**1.3.1 Fluorescence Spectroscopy**

Fluorescence is a phenomenon in which absorption of light by molecules results in emission of light from the excited state. The fluorescence process includes two steps. In the first step, light (photons) absorption promotes molecules from the ground state, $S_0$, to the excited singlet states $S_n$ ($n \geqslant 1$). In the second step, excited molecules return to the ground state through the emission of photons. In addition to fluorescence, excited molecules may undergo a non-radiative process called intersystem crossing (ISC) and transit to the excited triplet states. The triplet states then slowly decay back to the ground states with emission of photons, which is known as phosphorescence. It must be pointed out that emission is not the only process for excited molecules to dissipate their energy; there are other competitive processes, including release of heat, reaction, and transfer of energy to other molecules, for the molecules to return from the excited state to the ground state (Figure 1.5).

Upon excitation, molecules can reach any vibrational sub-levels associated with a given electronic state, which results in distinct absorption bands. After reaching one of the higher vibrational levels of an excited state, the molecules will rapidly lose vibrational energy and fall to the lowest vibrational level of the excited state. The excited molecules can lose energy again via internal conversion and fall to the lowest vibrational level of the first excited state ($S_1$).

Fluorescence occurs when molecules in the lowest vibrational level of the first excited state return to a vibrational level of the ground state by emitting light. Thus, the energy absorbed by a fluorophore is larger than the emission energy. This energy difference results in the Stokes shift, in which the emission maximum occurs at longer wavelength than the absorption maximum (Figure 1.6). Quantum yield describes the probability of an excited molecule to fluorescence or phosphorescence by calculating the ratio of the number of photons emitted relative to the number of photons absorbed.
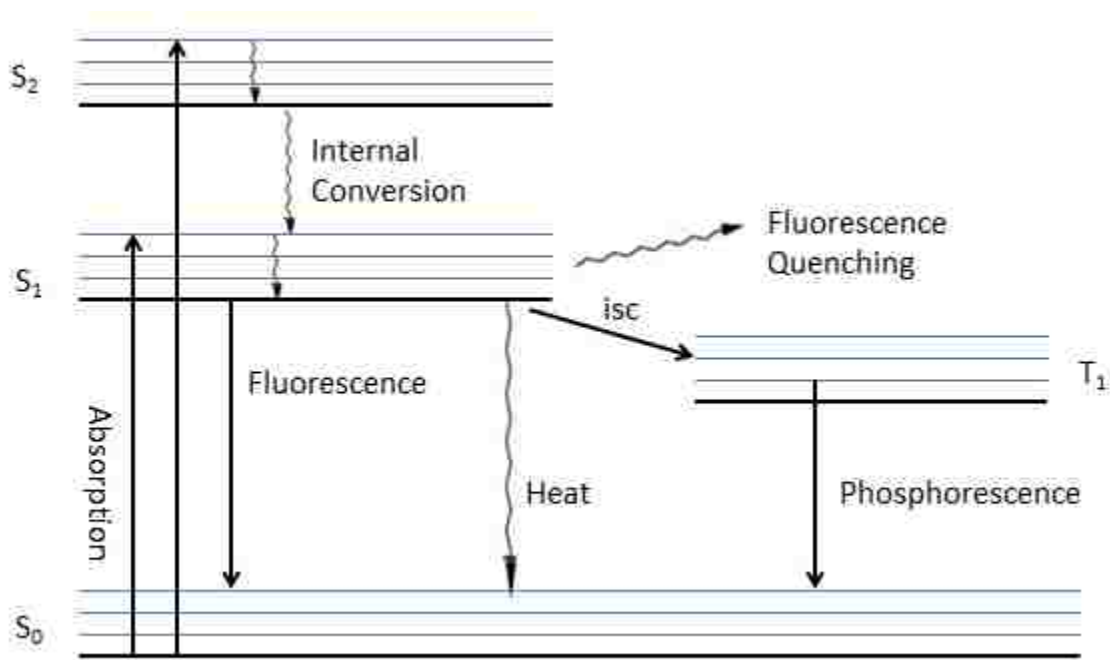


Figure1. 5  Jablonski diagram
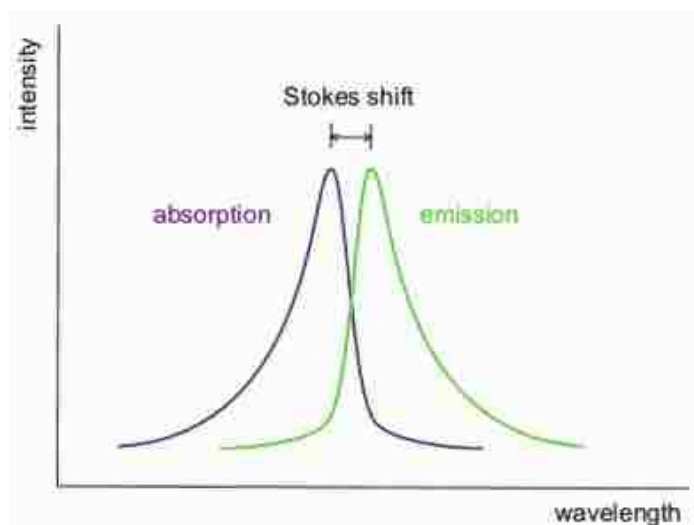
Figure1. 6    Stokes shift

Fluorescence spectroscopy has been widely employed as a detection technique in analytical chemistry for over 50 years and it is continuously expanding. Compared to other techniques, fluorescence spectroscopy can achieve low detection limits due to its high signal-to-noise ratio. For intensely fluorescent molecules, limits of detection of $10^{-10}$ M or lower are possible; in favorable cases under strictly controlled conditions, the ultimate limit of detection (a single molecule) may be reached.

### 1.3.2 Cyanine Dye Based Fluorescent GUMBOS

The emission of organic fluorophores often has a range from the ultraviolet visible to the near-infared (NIR) region. Among these regions, near-infared fluorescence has attracted intense attention recently for biomedical studies, such as photodynamic therapy [24, 25, 26] and biomedical imaging,[27, 28, 29, 30, 31, 32, 33] due to the low absorption coefficient and autofluorescence of the human skin tissue in the NIR region (700 – 900 nm) (Figure 1.7).  This distinct feature of NIR fluorescence greatly minimizes scattering and background interference, and allows a deeper

penetration of NIR emission for visualization of inner structure of biomatrices.[34] The NIR region

is often referred to as "NIR diagnostic window."
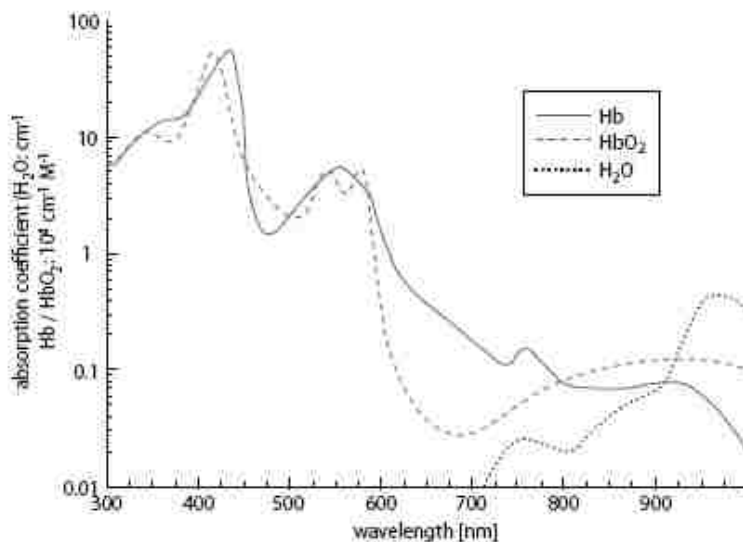


Figure1. 7 Absorption coefficient of oxyhaemoglobin, deoxyhaemoglobin and water as a function of wavelength[35]

Many fluorophores which emit NIR light have been developed for biomedical applications.

These NIR fluorophores include fluorescent NIR organic dyes, quantum dots, rare earth metals

nanoparticles, single-walled carbon nanotubes, [36] and fluorescent proteins.[37, 38] Among the five

categories of NIR fluorophores, organic dyes are the most frequently used NIR fluorescent

materials. The cyanine family of dyes makes the majority of commonly used organic dyes due to

their biocompatibility and desired photophysical properties.[34] In addition, cyanine dyes are often

ionic compounds suitable for conversion to GUMBOS in order to obtain desired properties when

coupled with selected counter ions.

**1.3.2.1 Introduction and Structure of Cyanine Dyes**

Cyanine dyes are a large family of synthetic pigments. The first cyanine dye was discovered

in 1856 by William, who noted that quinolinium salts emitted colors when heated with silver

oxide. Cyanine dyes absorb a wide range of wavelengths from the ultraviolet to the NIRregion compared to other dyes. Cyanine dyes have been widely used in silver halide photography,[39] laser technology,[40] and solar cells[23, 41] due to their high molar extinction coefficient. In addition to traditional uses, cyanine dyes, especially NIR cyanine dyes, have received extensive attention in biomedical applications as contrast agents for disease imaging and tissue characterization,[42, 43, 44] as well as photodynamic therapy agents. For example, indocyanine green (ICG), a NIR dye, is the only approved dye for clinical use as an imaging agent in ophthalmology, surgery, and inflammation imaging.[42, 43, 44, 45]

Cyanine dyes consist of two nitrogen centers, one of which is positively charged and the other neutral, linked by a conjugated polymethine chain. Based on the structure of the moieties containing nitrogen, cyanine dyes are classified into three types: streptocyanines (open chain cyanines, Figure 1.8I), hemicyanines (Figure 1.8II), and closed-chain cyanines (Figure 1.8III). For closed-chain cyanines, the nitrogen atoms are part of heteroaromatic rings, such as pyrrole, imidazole, pyridine, quinolone, thiazole, benzothiazole etc. Generally, cyanine dyes have all-trans geometries in their most stable form.
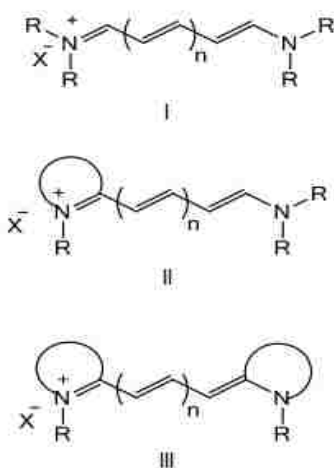


Figure1. 8 Chemical structures of cyanine dyes

**1.3.2.2 Spectroscopic and Photophysical Properties of Cyanine Dyes**

The spectroscopic and photophysical properties of cyanine dyes are a function of the structure of these molecules.

*Effect of the terminal groups*. Generally, asymmetric cyanine dyes, contain two different heterocyclic end groups, or one heterocyclic and one noncyclic terminal group. These later structures tend to absorb at shorter wavelengths than those of the corresponding symmetric cyanine dyes.[46] In addition, annelation at the heterocyclic terminal group causes cyanine dyes to absorb at longer wavelengths. [46]

*Effect of the length of the polymethine chain.* Research has demonstrated that introduction of additional vinylene leads to red shifting of the absorption maximum of the cyanine dyes by 100 nm. [46] Few monomethine (n=0) cyanine dyes show absorption peaks above 700 nm. Cyanine dyes which absorb and emit in the NIR regions are mainly trimethine (n=1), pentamethine (n=2) dyes or heptamethine (n=3) dyes. The streptopolymethines need longer polymethine chains than closed-chain cyanines to absorb in the NIR region. For example, the streptopolymethines parent chromophore (where R= -CH$_3$) absorbs at more than 700 nm with n=5. [46] The fluorescence quantum yields of cyanine dyes reach a maximum value and then decrease upon going from short to long chain lengths.[46]

*Effect of substitutions.* Substitution and other modifications can occur on the polymethine chain or on the aromatic ring. For substitutions on the polymethine chain, there are two possible ways to affect the spectroscopic properties of cyanines. The first causes an absorption shift depending on the inductive effect and position of the substituents, and the second changes the photophysical properties of dyes by steric effects. Electron-withdrawing groups at electron rich positions (such as 1, 3, 5 positions of polymethine chain) lead to blue-shifts of the absorption

maxima, while electron-donating groups result in red-shifts.[47, 48] At electron deficient positions (positions 2, 4 etc), the opposite trends are obtained in the presence of electron-withdrawing or electron-donating substituents. Steric effects occur when rigid substituents such as the six-membered carbocyclic rings in the polymethine chain. The rigid rings in polymethine chains greatly increase the photostability and quantum yield.[49, 50] For substitutions at heteroaromatic rings, the absorption maxima usually shift to longer wavelength.[51] However, the quantum yield is not monotone increasing but depends on the electronic effect of substituents. Strong electron-withdrawing groups (such as $-NO_2$, $-CF_3SO_2$) significantly improve the quantum yield, while electron-donating groups decrease the quantum yield.[52, 53]

*Effect of binding to biomolecules.* Binding of cyanine dyes to biomolecules can be covalent or non-covalent. Covalent attachment of dyes to biomolecules is typically achieved by the reaction of a sulfhydryl group or a primary amine with the dye maleimide or N-hydroxysuccinimide ester (NHS-ester), respectively. The attachment of biomolecules can potentially affect the photophysical properties of the dye considerably due to significant effects in the dynamics of cis-trans isomerization. Generally, covalent binding to biomolecules produces dramatic increases in the fluorescence quantum yield and lifetime with a red-shift in absorption wavelength.[54] Non-covalent labeling of biomolecules can involve ionic, hydrophobic, electrostatics, and hydrogen bonding interactions (Figure 1.9). This kind of non-specific binding to biomolecules results in formation of a stable complex (less stable than covalent linkages) and occurs at a faster rate (faster than covalent binding).[55] Compared to free dyes, complexes usually show increased fluorescence quantum yield and red-shifted absorption peaks.[56]
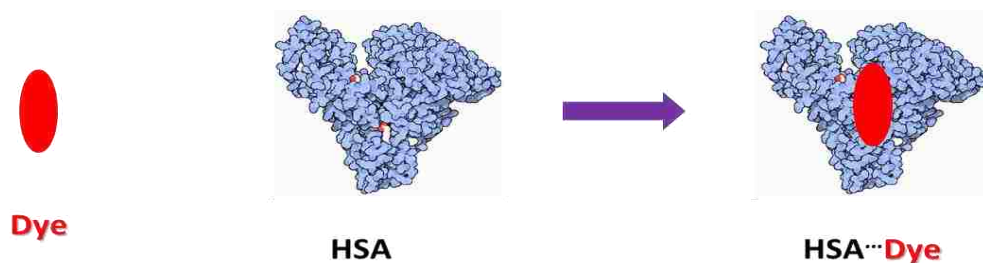
Figure1. 9  Illustration of non-covalent binding of dye to HSA.

### 1.3.2.3 Aggregation of Cyanine Dyes

Self-association of cyanine dyes in aqueous solution is frequently observed as a result of the strong Van der Waals-like intermolecular attractive forces between molecules.[57] Research has demonstrated that the aggregation of dyes displays different optical properties from that of the corresponding monomeric species.  Absorption bands may shift to longer wavelengths or shorter wavelengths and two types of proposed aggregate patterns have been developed to explain the spectral shifts. Aggregates leading to red shifts are referred to as J type aggregates,[58, 59] and blue shifted aggregates are termed H type aggregates.[60, 61, 62] J aggregates are composed of head to tail configurations, and H aggregates stack in a plane to plane (parallel) way to produce a sandwich formation (Figure 1.10). Factors which influence the extent of aggregation include the structure of the dye, temperature, medium composition, etc.[63] The self-association of cyanine dyes has been described by the exciton coupling theory, in which the molecule is regarded as a point dipole and the excitonic state of the dye aggregate splits into two levels through the interaction of transition dipoles. In the case of parallel aggregates, only transition to an upper state is allowed. Then a blue shift in  the absorption maxima is observed as a consequence, while for J aggregates, transition to a lower state results in a red shift.[64] H aggregates typically possess lower molar extinction coefficient and quantum yields than that of corresponding monomers. Due to their

12

significantly increased quantum yields, J aggregates have found applications in light harvesting, optical recording, and laser technology.
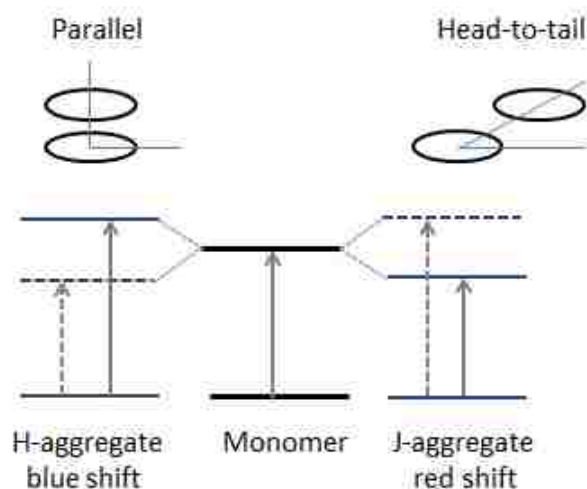


Figure1.10 Schematic of the excitonic energy state splitting, into two Levels: H-aggregate and J-aggregate. [65]

### 1.3.3 Lanthanide Ions Based Luminescent GUMBOS

Lanthanide metals are elements of atomic number 57 (lanthanum) through 71 (lutetium). Trivalent lanthanide ions ($Ln^{III}$) have been extensively studied due to their luminescence and magnetic properties. Their unique properties are readily explained by the electronic configurations of $Ln^{III}$ ([Xe]$4f^n$, n= 0-14).

### 1.3.3.1 Spectroscopic Properties of Lanthanide Ions

The electrons in 4f orbitals of $Ln^{III}$ are well shielded from the environment by the filled $5p^6 5S^2$ sub-shells and do not contribute to chemical bonding. Because of the shielding, the ligand-field effects in $Ln^{III}$ complexes (~500 cm$^{-1}$) are much smaller than that in d-transition metal complexes, which commonly extend from 15,000 to 25,000 cm$^{-1}$. [66] Therefore, the non-radiative deactivation processes are relatively rare and emissions from these $Ln^{III}$ complexes are common.

13

The partial energy levels of some of the trivalent lanthanide ions are shown in Figure 1.11. Due to the parity selection rules, 4f -4f transitions are parity-forbidden. However, absorptions with low molar absorption coefficients of $Ln^{III}$ are still present by "stealing" intensity from the allowed transition (such as 4f – 5d transition). As a result of the forbidden f-f transition, the lifetimes of the excited states are usually long-lived, up to milliseconds, and the emission is characteristic with narrow-line mostly in visible and NIR ranges.[67] A way to increase the absorption coefficients is to use an antenna, which absorbs light and then transfers energy to the lanthanide ion.
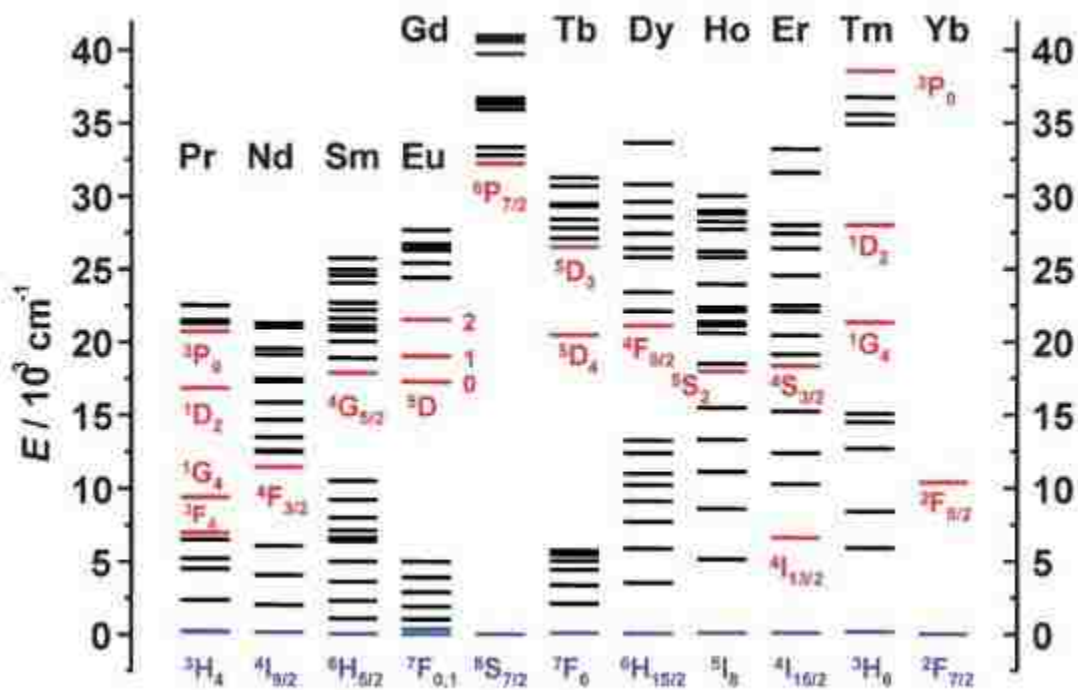


Figure1. 11 Partial energy diagrams for the lanthanide ions. The main luminescent levels are drawn in red, while the fundamental level is indicated in blue. [67]

### 1.3.3.2 Magnetic Properties of Lanthanide Ions

Valence electrons in $4f^n$ orbitals also provide $Ln^{III}$ magnetic properties due to the strong unquenched angular moment and spin-orbit coupling.[68] The energy level structure of 4f states is determined by the following interactions: the electron-electron interaction ($H_{ee}$), the spin-orbit coupling ($H_{so}$) and crystal field ($H_{cf}$), where $H_{ee} > H_{so} > H_{cf}$. The crystal field is much lower than interelectronic interaction and spin-orbit coupling, which is because the 4f electrons are located in the inner core and shielded by $5p^6 5S^2$ sub-shells. Then the electronic level structure can be described by Russell-Saunder coupling scheme, where an energy level of $^{2S+1}L_J$ multiplet is observed.[69]

Among the multiplets, the ground state multiplet has the lowest energy and dominates at room or lower temperature, and therefore it is the only one that contributes to the magnetic properties. Typically, $S$, $L$, and $J$ correspond to the total spin angular momentum, the total orbital angular momentum and the total angular momentum, respectively, of the ground state multiplet. This ground state multiplet fulfills three conditions called Hund's rules: (i) It has the maximum allowed spin value ($S$); (ii) For a given spin multiplicity, it has the maximum allowed angular momentum ($L$); and (iii) The value of the total momentum, $J$, is equal to $J = |L - S|$ when the 4f subshell is less than half filled, while $J = L + S$ when the 4f subshell is more than half filled.

Neglecting crystal field, Hund's formula applies:

$$\mu \approx g_J \sqrt{J(J + 1)} \ \mu_B \text{ (except } 4f^4 \ 4f^5 \ 4f^6 \text{ systems)}$$

Where $\mu$ is permanent magnetic moment, $\mu_B$ is Bohr magneton, $g_J$ is given by

$$g_J = \frac{3}{2} + \frac{S(S+1) - L(L+1)}{2J(J+1)}$$

In the isolated ions, the crystal field effects split the $J$ multiplet, resulting in a large deviation from the Curie law at low temperature. Unlike the transition metal ions, the magnetic moment of $Ln^{III}$ is temperature dependent.

### 1.3.3.3 Ionic Liquid Crystals

Liquid crystals flow like liquid; but maintain orientational order and show anisotropic properties. Molecules which can form liquid crystals usually have either rod-like or disc-like shape. Driving forces for formation of liquid-crystalline phase (mesophase) include dipole-dipole interaction, Van der Waals interactions, $\pi$-$\pi$ stacking, etc.

Ionic liquid crystals (ILCs) are a class of liquid-crystalline compounds that are composed of cations and anions. As a special type of liquid crystals, ILCs combine the properties of both liquid crystals and ionic liquids. At a molecular level, ILCs can be viewed as ionic liquids (above the clear point they are definitely ionic liquids) since the local structure of the mesophase is dominated by short-range interactions. At the macroscopic level, ILCs are in all respects liquid crystals, since the behavior depends on the structure of the phase. Consequently, ILCs are anisotropic at a macroscopic level, but at molecular level, ILCs have the properties of ionic liquids, which are different from that of organic liquid crystals. A typical property of ILCs is ion conductivity. [70]

ILCs may display a variety of mesophases, including nematic (N), smectic (Sm), columnar (Col) and cubic (Cub).[71] Rodlike (calamitic) molecules usually form nematic and smectic mesophases. The nematic phase is the least ordered mesophase, in which the rod-like molecules are arranged in random positions with their long molecular axis, on average, parallel to a preferential direction (so-called "director", denoted by $\tilde{n}$. Figure 1.12 A). Smectic A (Sm A, Figure 1.12 C) is the least ordered smectic mesophase, and the molecules are arranged in layers

16

with their long molecular axis on average perpendicular to the layer plane. Smectic C (SmC, Figure 1.12 D) mesophase is very similar to SmA mesophase, but the long molecular axis is tilted to the layer plane instead of perpendicular. In ordered smectic B (SmB, Figure 1.12 E) mesophase, there is a 6-fold bond orientation order, and, therefore, the translational order is lost within few intermolecular distances. The cations of the ILCs often consist of a positively charged head with a long hydrophobic alkyl chain. Thus, the driving forces for formation of ionic mesophases are more complicated than that of organic liquid crystals. In ILCs, the cation-cation repulsive interaction, hydrophobic interaction between long alkyl chain, hydrogen bonding and electrostatic attractive interaction between cations and anions work together to form and stabilize ionic mesophases.[72] Due to the combination of these forces, unique smectic mesophases are found in ILCs.  A smectic T (SmT, Figure 1.12 F) phase observed in ammonium mesogens (compounds that display liquid crystalline behavior) exhibits tetragonal layers, separated by long alkyl chains. In a $SmA_2$ (Figure 1.12 G) phase, cations and anions are assembled in bilayers, separated by double layer of long alkyl chain.[70, 71]

Disc-like molecules usually form columnar phases, in which the discs are stacked one top of another to form columns. In the hexagonal columnar ($Col_h$, Figure 1.12 H) and rectangular columnar ($Col_r$, Figure 1,12 I) phases, the columns are arranged into a hexagonal lattice or rectangular lattice. The disc-like molecules can also form a nematic phase: a discotic nematic phase ($N_D$), in which the discs are arranged in a nematic order; while in a columnar nematic phase ($N_{col}$), the columns are arranged in a nematic order.[70, 71]

= calamitic molecule ( = cationic "head";  = counteranion;  = long alkyl "tail")

A, nematic (N) phase

B, chiral nematic (N*) phase

C, smectic A (SmA) phase

D, smectic C (SmC) phase

E, smectic B (SmB) phase

F, smectic T (SmT) phase

= discotic molecule

H, hexagonal columnar (Col$_h$) phase

I, rectangular columnar (Col$_r$) phase

G, smectic A$_2$ (SmA$_2$) phase
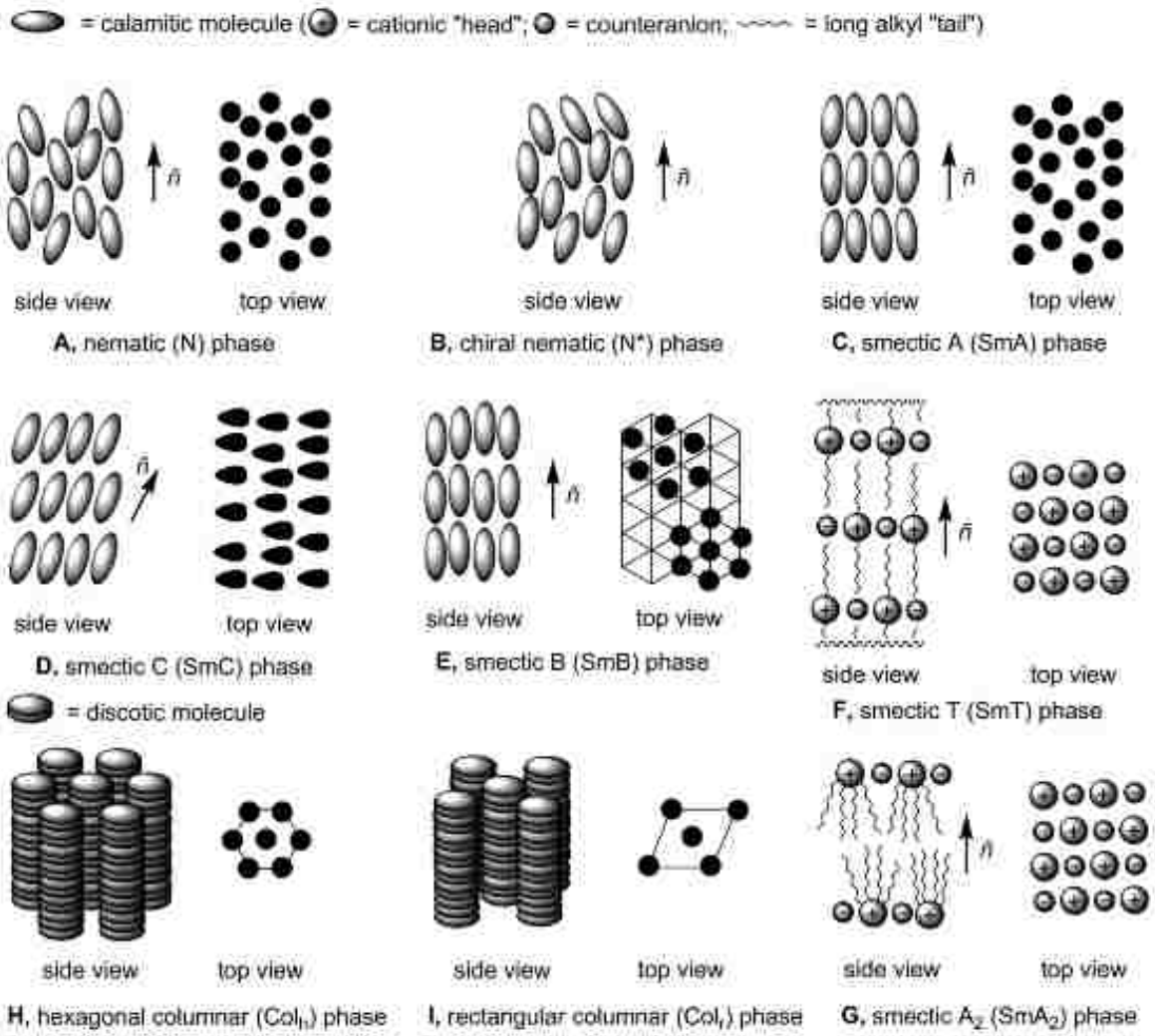
Figure1. 12 Schematic representation of mesophases [71]

The formation and orientation of mesophases of ILCs depend on the properties and structures of cations and anions, as well as the surrounding environments, such as solvents and temperature. A thermotropic mesophase is formed by heating a solid or cooling an isotropic liquid, while a lyotropic mesophase is prepared by dissolving an amphiphilic mesogen in a suitable solvent with appropriate concentration and temperature. Among these factors, the structural properties of cations and anions that constitute the ILCs are the primary elements that

18

determine the structures of mesophases. Thus, the extensive amount cations and anions available make the properties of ILCs widely tunable.

**1.3.3.4 Trivalent Lanthanide Ion based GUMBOS and Ionic Liquid Crystal**

$Ln^{III}$-based GUMBOS (especially ionic liquids) have recently attracted considerable attention since these GUMBOS may be designed for specific applications by incorporation of various functionalities in ion pairs via the selection of specific cation-anion combinations.[73, 74] In the $Ln^{III}$-based GUMBOS, the $Ln^{III}$-ligand complexes serve as anions with paramagnetic and luminescence properties, while the counter ions provide the GUMBOS with other functionalities, such as ability for formation of liquid crystals,[75, 76, 77, 78] targeting to cancer cells,[18] etc.

Ionic liquids containing lanthanide ions are attractive materials, that combine the properties of the ionic liquids with the magnetic and optical properties of incorporated lanthanides. Usually, the lanthanides containing ILs are multicomponent ILs synthesized by dissolving the lanthanide complexes into the ionic liquids. These lanthanide ILs solutions are potential soft materials for applications in organic light-emitting diodes (OLEDs),[79] metal separation,[80] and electrodeposition.[81] However, poor solubility of lanthanide complexes in ILs limits the use of lanthanide containing ionic liquids. Peter Nockemann[82] and co-workers have developed the first lanthanide based ionic liquids which consist of 1-butyl-3-methylimidazolium [BMIM] and lanthanide thiocyanate anions $[Ln(NCS)_x(H2O)_y]^{3-x}$ (x = 6-8; y = 0-2). However, these ILs contain water, which quenches the luminescence of $Ln^{III}$ due to the absorption of energy of excited states through the excitation of O-H vibration, and, therefore, limits the optical applications. Anja-Verena Mudring[73] and co-workers developed the first "true" lanthanide based ILs without use of neutral coligands. Lanthanide based ionic liquid crystals have also been

19

reported by Anja-Verena Mudring group.[75] The authors developed a new material [C$_{12}$mim]$_3$[DyBr$_6$] with luminescent as well as mesomorphic and magnetic properties.

**1.4 Computational Modeling of Carbazole Based Fluorescent GUMBOS**

**1.4.1 Computational Modeling of GUMBOS**

Computational chemistry is a branch of chemistry which uses principles of computer science to assist in solving chemical problems. Because of the difficulties of dealing with materials in nano- and molecular levels, computational modeling has become important for interpretation and prediction of experimental results.

Many efforts have been undertaken to simulate inorganic salts and their liquid state structures through computational calculations in the 1970's through the use of inter-ionic potentials.[83] However, except for the early theoretical calculations on organic salts, little work has been done until relatively recently.[84, 85, 86, 87] To theoretically study organic salts, many approaches have been developed to meet the different simulation purposes. Using quantum mechanical calculations, which is based on solving Schrödinger's equation, one can obtain ion pair stability, intramolecular geometry, orientation of ions in the pairs, hydrogen bonding, degree of charge transfer between ions, and vibrational frequency of small and medium systems. For a better molecular understanding of the dynamical process while describing the essential overall behavior of GUMBOS, classical molecular dynamic (MD) modeling has been developed based on Newtonian mechanics. This method is good for simulation of systems containing ~1000 molecules. Statistical, (thermodynamical) mechanical simulation, which employs statistical physical and thermodynamics, enables one to study large length- and time-scale phenomena, and, thus, the intrinsic morphologies of GUMBOS.

**1.4.1.1 Quantum Mechanics Simulation**

*Methods*: Quantum mechanical calculations are aimed at finding the solution to the Schrödinger's equation, however; we can only solve the equation using a one-electron atom (hydrogen atom). Fortunately, approximation (Born-Oppenheimer approximation) has been developed to help solve the equation for multi-electron atoms. This approximation assumes nuclei are stationary because nuclei are much more massive than electrons. Based on this approximation, Hartree-Fock (HF) methods and post-HF methods have been carried out. Density functional theory (DFT) is alternative to wavefunction based electron structure. DFT assumes that there exists a function that will calculate the molecular energy from electron density, and accounts for electron correlation by estimating the interaction of an electron with total electron density.

*Basis sets:* In the last paragraph, two quantum mechanical methods were introduced. To calculate the electronic structure, we still need basis functions (basis set) to describe the orbitals of atoms in a molecule. Linear combinations of basis functions approximate the total electronic wavefunction, while basis functions themselves are linear combinations of Gaussian type orbitals (GTO). Slater type orbitals (STO) were firstly used in atomic calculation due to its accuracy, but were abandoned soon after the initial success due to the complexity in the evaluation of multicenter integrals required in the molecular calculations. Using a linear combination of primitive GTO, which is so-called contracted GTO (CGTO), to mimic STO is an alternative way to overcome the problem of evaluation of integrals (Figure 1.13). GTO started to become the most popular basis set for the calculation of molecular electronic structure. Two conflicting goals for basis sets, efficiency and accuracy, have led to the generation of many different basis sets. The minimal basis is STO-3G. Since the valence electrons are responsible for bonding, more

than one basis functions are usually used to calculate the valence orbitals. If two basis functions were used, it is double-zeta; if three, it is triple-zeta. This approximation is called split-valence basis sets. Pople's split-valence basis set like 6-31G means that the inner shell is a CGTO made of 6 Gaussians, and the valence is described by two basis functions — one CGTO made of 3 Gaussians, and one single Gaussian. Adding more basis functions per atom allows orbitals to change size, and adding polarization functions to atoms allows orbitals to change shape. For example, 6-31G (d, p) means that adding d functions for heavy atoms and p functions to H atoms. When calculating lone pairs, anions, excited states etc., diffuse functions are needed. For instance, 6-31++G means adding diffuse functions to both heavy atoms and H atoms. Dunning correlation-consistent basis sets are optimized using correlated wavefunctions. An example of Dunning basis set is aug-cc-pVDZ, where aug means one diffuse function is added for every angular momentum present in the basis, cc means Dunning correlation-consistent, p means polarized valence, D means double-zeta basis.
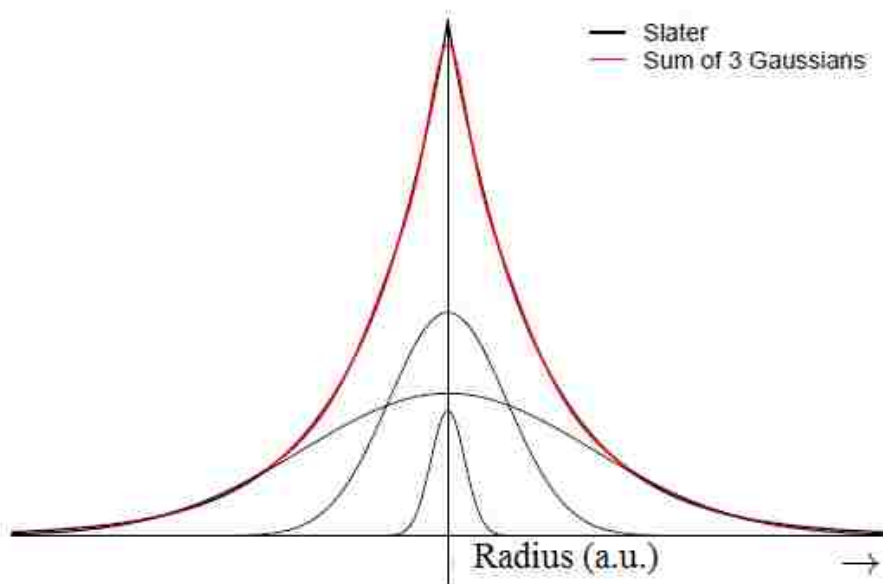


Figure1. 13 Linear combination of primitive Gaussians form contracted Gaussians

Quantum mechanical calculation, which employs *ab initio* (from the first principles) molecular dynamic method or density functional theory (DFT), is the most accurate method for simulation of molecules. From this calculation, detailed and important information on individual ions and ion pairs were obtained. Renqing Lue [88] and co-workers employed the density function method and DNP basis set to study 1-pair, 2-pair, and 3-pair cation–anion interactions of 1-propyl-4, 5-dibromo-3-methylimidazolium bromides. Chu Guo[89] and co-workers optimized the structure of pseudoisocyanine (PIC) and calculated the Raman vibrational frequencies of these compounds based on DFT at the B3LYP level and using the 6-31G (d, p) basis set. Tingting Gao[90] and co-workers performed computational calculations to investigate the interactions of ILs with different classes of volatile organic compounds (VOCs), including alcohols, aldehydes, ketones, alkanes, alkenes, alkynes, and aromatic compounds. Madhulata Shukla [91] and co-workers have investigated the spectral features of 1-butyl-3-methylimidazolium iodide (bmimI) by use of Time Dependent-DFT (TD-DFT) calculations at B3LYP level using the DGDZVP basis set.

**1.4.1.2 Classic Dynamic Simulation**

Although ab initio molecular dynamic method is highly accurate to calculate intermolecular and intramolecular interactions at atomic level, their application in large length and time scale systems is limited due to the need for expensive computational resources. In order to simulate large systems, which contain hundreds of atoms and long-time processes, classic molecular dynamics (MD) simulations were developed using Newtonian mechanics instead of quantum mechanics. Since this method is less accurate, we still use the numbers derived from quantum mechanics as constants in our MD simulation for the purpose of alleviating this problem. MD does not consider electrons and only takes into account the nuclei since nuclei are much larger

than electrons, thus, nuclear motion, vibration, and rotation can be studied separately from electrons. For MD simulation, the following information is required from each atom in a molecule: position, momentum (mass and velocity), charge, and bonding information.

A single atom will be affected by the potential energy functions of every atom in the system, and these interactions in turn affect the motion of the atom. The potential energy is described in the form:

$$E(R) = \sum_{1,2\ pairs} \frac{1}{2} K_b (b - b_0)^2 + \sum_{angles} \frac{1}{2} K_\theta (\theta - \theta_0)^2 \ + \ \sum_{dihedrals} K_\Phi (1 + \cos(n\Phi - \delta)) + \sum_{i,j} \{ 4\ \varepsilon_{ij} \left[ \left( \frac{\sigma_{ij}}{r_{ij}} \right)^{12} - \left( \frac{\sigma_{ij}}{r_{ij}} \right)^{6} \right] + \frac{q_i q_j}{\varepsilon D r_{ij}} \}$$

This is called the force field which contains bonded terms including stretching, bending, and torsions along with non-bonded interactions that consist of van der Waals and electrostatic potentials.

ILs have been widely studied using classical molecular dynamics with refined force field. Ramesh Singh[84] and co-workers used MD simulation to investigate the dynamics of the ionic liquid [BMIM$^+$][PF$_6^-$] when confined inside an uncharged slit-like graphitic pore of width H= 5.4 nm, in the temperature range 300-400 K. They also performed molecular dynamics to study the structural and dynamical properties of [BMIM$^+$][PF$_6^-$] confined inside multiwalled carbon nanotubes (MWCNTs).[92] Trinidad Mendez-Morales[93] and co-workers investigated the dynamic properties of alcohol and IL mixtures.

### 1.4.1.3 Coarse Grain Molecular Dynamics (CGMD)

Previous approaches have been limited to simulation times and system sizes less than 100 ns and 10 nm, however, sometimes GUMBOS can exhibit structural order beyond these molecular distances. Such orders are typically denoted as nano-sized structures. To simulate these systems, coarse grain molecular dynamics (CGMD) were developed with a reduced number of degrees of freedom and eliminated fine interaction details. CGMD assumes all atoms present within a given length scale are one united-atom or bead, and beads are connected to one another by "bonds." Figure 1.14 depicts the representation of an imidazolium cation in ab initio, atomistic and coarse grain MD simulations.
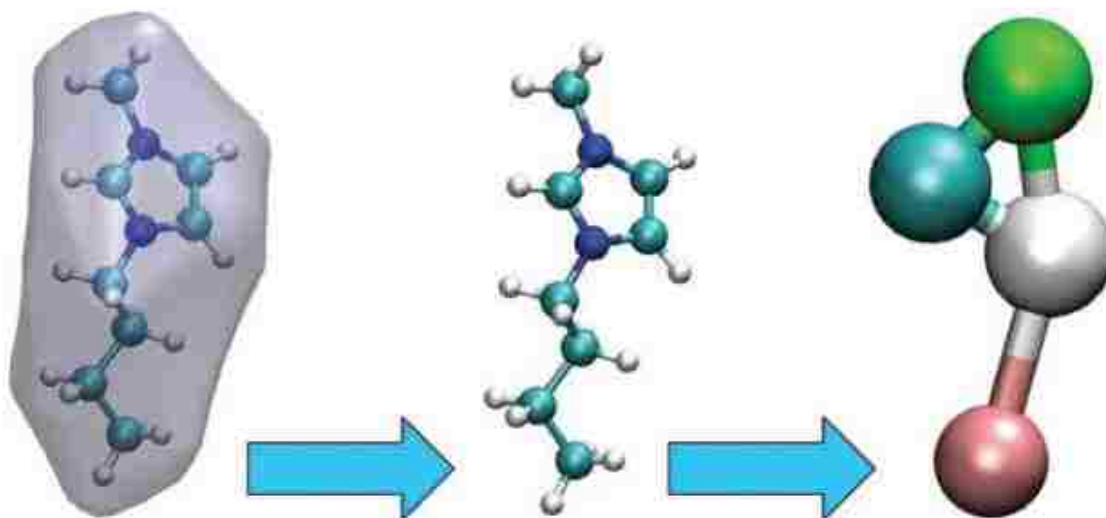


Figure1. 14 Imidazolium cation in ab initio, atomistic and coarse grain MD simulations (from left to right)[83]

### 1.4.2 Current Theoretical Studies of Carbazole Derivatives

Carbazole is an important aromatic heterocyclic compound. It has a nitrogen atom as an electron donor (Figure 1.15), which makes its ring easily functionalized and covalently linked to

other molecules. Carbazole derivatives, with appropriate chemical modification, have been synthesized and investigated as organic electronic devices because of carbazole's high thermal stability and excellent photophysical properties.[94] Carbazole derivatives can be used as materials for hole-transporting layers of both small molecule and polymer organic light emitting diodes (OLEDs) due to their high charge mobility.[95, 96, 97, 98, 99] Many carbazole based compounds have also been used as white, red, green, and in some cases even blue triplet emitters due to the large bang gap of the biphenyl unit.[100, 101] In addition, the optical and electronic properties of carbazole are tunable by substitution on 2-, 3-, 6-, 7-, and 9-H positions. Carbazole based GUMBOS can be developed by covalently linking a cation to the carbazole ring.
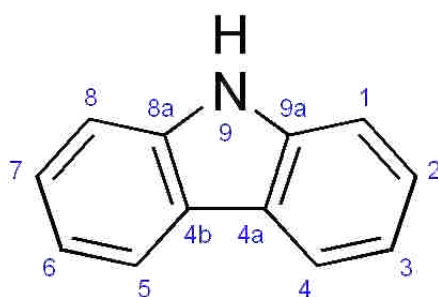


Figure1. 15 Chemical structure of carbazole

Current theoretical (computational) studies of carbazole derivatives are focused on the effects of substitutions on HOMO levels. Predictions of the spectral and electronic properties employ DFT, Time Dependent-DFT (TDDFT) and HF methods. Theoretical calculations for N-methylcarbazole and 3, 6-diphenyl-N-methyl carbazole were carried out by Neeraj Agarwal [102]and co-workers using B3LYP/6-31G(d). Calculated results indicate that 3- and 6-positions of carbazole have largest contribution to HOMO levels and hence the effect of electron donating/withdrawing groups (EDG/EWG) in these positions would result in maximal changes in the HOMO level. Similarly, the density distribution in the model compound 3, 6-diphenyl-N-

methylcarbazole shows that ortho and para positions of the phenyl group have the largest contribution to the HOMO level (Figure 1.16 b). Hence, substitution at ortho and para positions of the phenyl group with EDG/EWG should tune the HOMO energy levels. Michel Belletete[103] and co-workers used RHF/6-31G* and RCIS/6-31G* to calculate the ground state and excited states of covalently linked carbazole-based dimers: N,N-diethyl-2,2-bicarbazole (CC), 2-(N-ethylcarbazol-2-yl)thiophene (CT), and 2-(N-ethylcarbazol-2-yl)furan (CF). The calculation results indicate that the absorption is due to the $S_0$-$S_2$ transition and fluorescence is a result of $S_1$-$S_0$ transition.
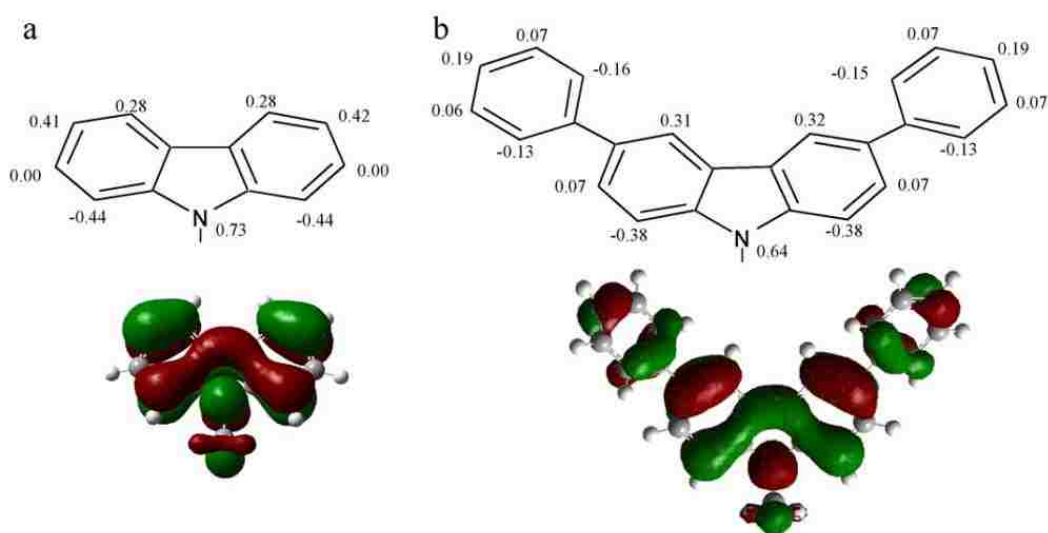


Figure1. 16 Representation of the pz contribution of the atomic orbitals for HOMO (above) and molecular orbital plots (below) [102]

## 1. 5 Analytical Techniques, Methods and Software Used

### 1.5.1 UV-Vis Spectroscopy

Many molecules absorb ultraviolet or visible light and induce promotion of one electron from the ground state to the excited states. As a result, the intensity of light decreases at a wavelength where absorbance occurring. UV-Vis spectroscopy is the measurement of the

wavelength and intensity of absorbance of ultraviolet and visible light by a sample. Absorbance (A) is directly proportional to the path length, b (cm), and the concentration, c (M), of the absorbing species at low concentration ranges. Beer's Law states that $A = \varepsilon bc$, where $\varepsilon$ is molar absorbtivity with units of $M^{-1}$ $cm^{-1}$. The spectrum is recorded by plotting absorbance as a function of wavelength. A typical UV-Vis spectrophotometer consists of light source, monochromator, sample, and detector as shown in Figure 1.17.
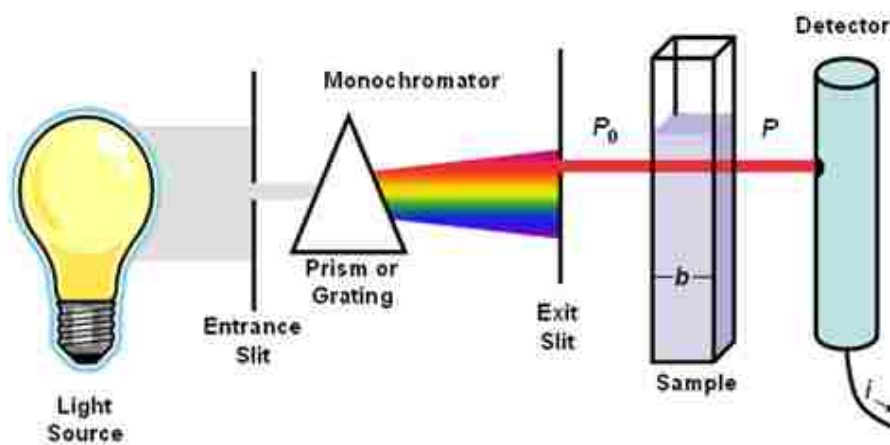


Figure1. 17 Schematic of a UV-Vis spectrophotometer

## 1.5.2 Fluorescence Spectroscopy

Fluorescence principles have been discussed in section 1.3.1. A fluorometer is used to record the fluorescence spectra and other information of molecules. A fluorometer consists of a light source, an excitation monochromator, an emission monochromator, a sample cell, and a detector (Figure 1.18). Since a sample emits equally, in all directions, the emission monochromator is positioned orthogonally from the excitation light to minimize light scattering by the solution and cell.
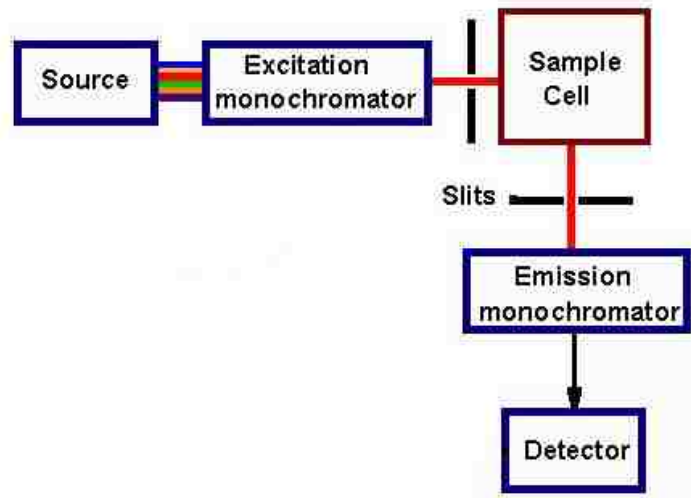
Figure1. 18 Schematic of a fluorometer

## 1.5.3 Superconducting Quantum Interference Device (SQUID) Magnetometer

A Superconducting Quantum Interference Device (SQUID) uses the properties of electron-pair wave coherence and Josephson Junctions to detect very small magnetic fields. A SQUID consists of a loop of superconductor with one or more Josephson junctions, called weak links. Figure 1.19 shows an example of SQUID with weak links at X and W, where critical current ( $i$ ) is much less than the critical current ( I ) of the main ring. The magnetic field through the loop causes a phase difference between electrons, affecting current through the loop. If a magnetic field is applied perpendicular to the plane of the ring, a phase difference is produced in the electron-pair wave along the path XYW and WZX and will be measured.

29
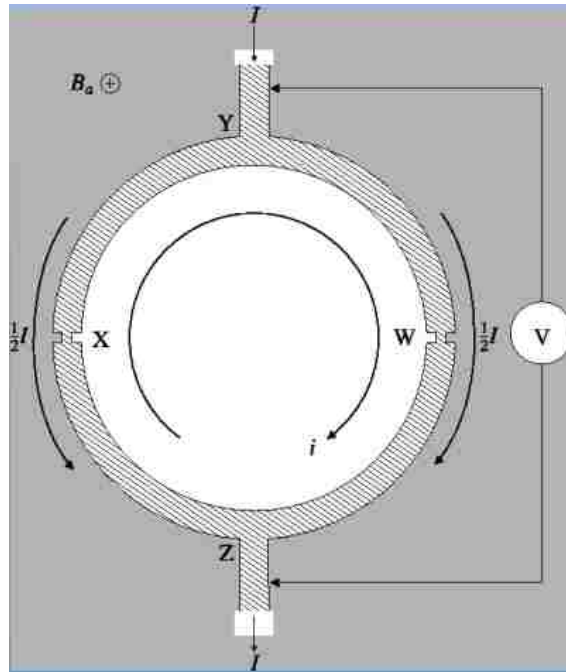
Figure1. 19 Superconducting quantum interference device (SQUID) as a simple magnetometer.

### 1.5.4 Transmission Electronic Microscopy

Transmission electron microscopy (TEM) is a microscopy technique that has been widely used to visualize nano-scale materials due to its high resolution and magnification. TEM (Figure 1.20) uses an accelerated beam of electrons to transmit through an ultra-thin specimen, and produces many interactions with the specimen as it passes through. An image is formed from the interaction of the electrons penetrated through the specimen. The image is magnified by electromagnetic lenses and projected onto an imaging device, such as a fluorescent screen, on a layer of photographic film, or to be detected by a CCD camera.
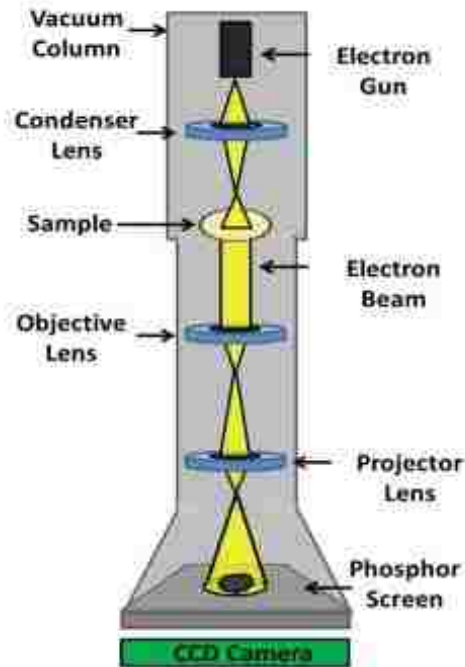
Figure1. 20 Schematic of a TEM

## 1.5.5 Polarized Optical Microscopy

Polarized optical microscopy (POM) uses plane-polarized light to analyze birefringent structures, such as crystals and liquid crystals. As shown in Figure 1.21, a polarized light microscope consists of (from bottom to top) a light source, polarizer, specimen, analyzer (another polarizer), and camera. In a polarized light microscope, light from the source transmits through a polarizer and produces a plane-polarized light vibrating in only one direction ($0^0$). A birefringent specimen, whose refractive index depends on direction, produces two individual wave components that are each polarized in mutually perpendicular planes, after interaction with plane-polarized light. Then one of the components will pass through the analyzer ($90^0$). Therefore a birefringent specimen will be seen as a bright image. In contrast, polarized light will pass through an isotropic sample that has a refractive index that is equal in all directions and remain unaltered, resulting in a dark image.

31
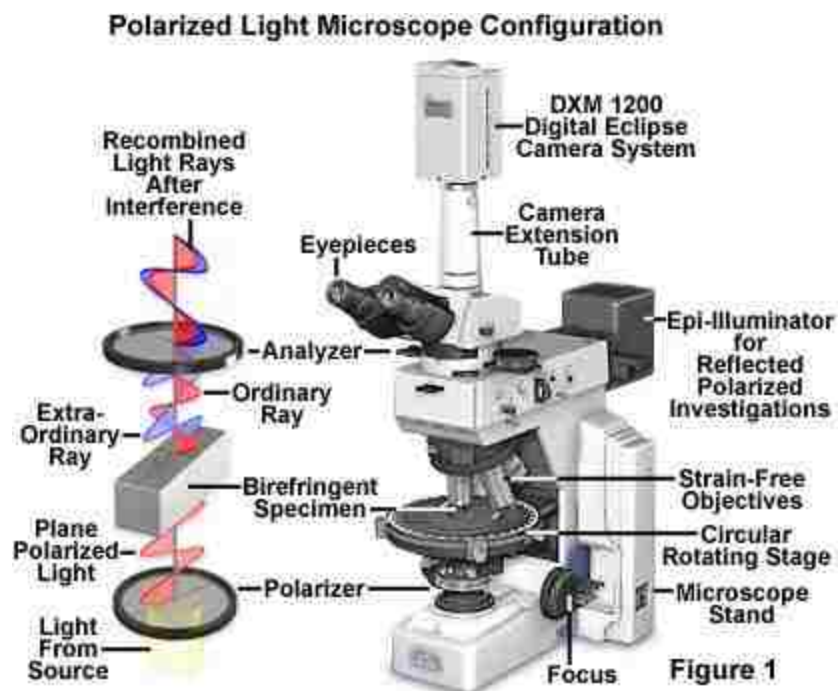
Figure1. 21 Polarized Optical Microscope Configuration

## 1.5.6 Circular Dichroism Spectroscopy

Circular dichroism is the difference in absorption of left-handed circularly polarized light (L-CPL) and right-handed circularly polarized light (R-CPL) and occurs when a molecule contains one or more chiral chromophores. Circular dichroism (CD) spectroscopy is a spectroscopic technique where the CD of molecules is measured over a range of wavelengths. CD spectroscopy is used extensively to study chiral molecules of all types and sizes. Measurements carried out in the visible and ultraviolet region of the electro-magnetic spectrum monitor electronic transitions, and, if the molecule under study contains chiral chromophores then one CPL state will be absorbed to a greater extent than the other and the CD signal over the corresponding wavelengths will be non-zero. A CD signal can be positive or negative, depending on whether L-CPL is absorbed to a greater extent than R-CPL (CD signal positive) or to a lesser extent (CD signal negative)

### 1.5.7 Gaussian 09

Gaussian 09 is the latest in the Gaussian series of programs. It provides state-of-the-art capabilities for electronic structure modeling. Starting from the fundamental laws of quantum mechanics, Gaussian 09 predicts the energies, molecular structures, vibrational frequencies and molecular properties of molecules and reactions in a wide variety of chemical environments. Gaussian 09's models can be applied to both stable species and compounds which are difficult or impossible to observe experimentally (e.g., short-lived intermediates and transition structures). Gaussian 09 provides the most advanced modeling capabilities available today, and it includes many new features and enhancements which significantly expand the range of problems and systems which can be studied. With Gaussian 09, you can model larger systems and more complex problems than ever before, even on modest computer hardware.

– Gaussian 09 official website.

### 1.6 References

1.      Buszewski, B.; Studzinska, S. A review of ionic liquids in chromatographic and electromigration techniques. *Chromatographia* **2008,** *68* (1-2), 1-10.

2.      Hallett, J. P.; Welton, T. Room-Temperature Ionic Liquids: Solvents for Synthesis and Catalysis. 2. *Chemical Reviews* **2011,** *111* (5), 3508-3576.

3.      Pandey, S. Analytical applications of room-temperature ionic liquids: A review of recent efforts. *Analytica Chimica Acta* **2006,** *556* (1), 38-45.

4.      Welton, T. Room-temperature ionic liquids. Solvents for synthesis and catalysis. *Chemical Reviews* **1999,** *99* (8), 2071-2083.

5.      Plechkova, N. V.; Seddon, K. R. Applications of ionic liquids in the chemical industry. *Chemical Society Reviews* **2008,** *37* (1), 123-150.

6.      Walden, P. Molecular weights and electrical conductivity of several fused salts. *Bull. Acad. Imper. Sci.* **1914**.

7.      Chum, H. L.; Koch, V. R.; Miller, L. L.; Osteryoung, R. A. ELECTROCHEMICAL SCRUTINY OF ORGANOMETALLIC IRON COMPLEXES AND HEXAMETHYLBENZENE IN A ROOM-TEMPERATURE MOLTEN-SALT. *Journal of the American Chemical Society* **1975,** *97* (11), 3264-3265.

8. Wilkes, J. S.; Levisky, J. A.; Wilson, R. A.; Hussey, C. L. DIALKYLIMIDAZOLIUM CHLOROALUMINATE MELTS - A NEW CLASS OF ROOM-TEMPERATURE IONIC LIQUIDS FOR ELECTROCHEMISTRY, SPECTROSCOPY, AND SYNTHESIS. *Inorganic Chemistry* **1982,** *21* (3), 1263-1264.

9. Fry, S. E.; Pienta, N. J. EFFECTS OF MOLTEN-SALTS ON REACTIONS - NUCLEOPHILIC AROMATIC-SUBSTITUTION BY HALIDE-IONS IN MOLTEN DODECYLTRIBUTYLPHOSPHONIUM SALTS. *Journal of the American Chemical Society* **1985,** *107* (22), 6399-6400.

10. Boon, J. A.; Levisky, J. A.; Pflug, J. L.; Wilkes, J. S. FRIEDEL CRAFTS REACTIONS IN AMBIENT-TEMPERATURE MOLTEN-SALTS. *Journal of Organic Chemistry* **1986,** *51* (4), 480-483.

11. Niedermeyer, H.; Hallett, J. P.; Villar-Garcia, I. J.; Hunt, P. A.; Welton, T. Mixtures of ionic liquids. *Chemical Society Reviews* **2012,** *41* (23), 7780-7802.

12. Tesfai, A.; El-Zahab, B.; Kelley, A. T.; Li, M.; Garno, J. C.; Baker, G. A.; Warner, I. M. Magnetic and Nonmagnetic Nanoparticles from a Group of Uniform Materials Based on Organic Salts. *Acs Nano* **2009,** *3* (10), 3244-3250.

13. Bwambok, D. K.; El-Zahab, B.; Challa, S. K.; Li, M.; Chandler, L.; Baker, G. A.; Warner, I. M. Near-Infrared Fluorescent NanoGUMBOS for Biomedical Imaging. *Acs Nano* **2009,** *3* (12), 3854-3860.

14. Lu, C.; Das, S.; Magut, P. K. S.; Li, M.; El-Zahab, B.; Warner, I. M. Irradiation Induced Fluorescence Enhancement in PEGylated Cyanine-Based NIR Nano- and Mesoscale GUMBOS. *Langmuir* **2012,** *28* (40), 14415-14423.

15. Cole, M. R.; Li, M.; El-Zahab, B.; Janes, M. E.; Hayes, D.; Warner, I. M. Design, Synthesis, and Biological Evaluation of beta-Lactam Antibiotic-Based Imidazolium- and Pyridinium-Type Ionic Liquids. *Chemical Biology & Drug Design* **2011,** *78* (1), 33-41.

16. Das, S.; de Rooy, S. L.; Jordan, A. N.; Chandler, L.; Negulescu, I. I.; El-Zahab, B.; Warner, I. M. Tunable Size and Spectral Properties of Fluorescent NanoGUMBOS in Modified Sodium Deoxycholate Hydrogels. *Langmuir* **2012,** *28* (1), 757-765.

17.     Magut, P. K. S.; Das, S.; Fernand, V. E.; Losso, J.; McDonough, K.; Naylor, B. M.; Aggarwal, S.; Warner, I. M. Tunable Cytotoxicity of Rhodamine 6G via Anion Variations. *Journal of the American Chemical Society* **2013,** *135* (42), 15873-15879.

18.     Li, M.; Ganea, G. M.; Lu, C.; De Rooy, S. L.; El-Zahab, B.; Fernand, V. E.; Jin, R.; Aggarwal, S.; Warner, I. M. Lipophilic phosphonium-lanthanide compounds with magnetic, luminescent, and tumor targeting properties. *Journal of Inorganic Biochemistry* **2012,** *107* (1), 40-46.

19.     Dumke, J. C.; El-Zahab, B.; Challa, S.; Das, S.; Chandler, L.; Tolocka, M.; Hayes, D. J.; Warner, I. M. Lanthanide-Based Luminescent NanoGUMBOS. *Langmuir* **2010,** *26* (19), 15599-15603.

20.     de Rooy, S. L.; El-Zahab, B.; Li, M.; Das, S.; Broering, E.; Chandler, L.; Warner, I. M. Fluorescent one-dimensional nanostructures from a group of uniform materials based on organic salts. *Chemical Communications* **2011,** *47* (31), 8916-8918.

21.     Das, S.; Bwambok, D.; El-Zahab, B.; Monk, J.; de Rooy, S. L.; Challa, S.; Li, M.; Hung, F. R.; Baker, G. A.; Warner, I. M. Nontemplated Approach to Tuning the Spectral Properties of Cyanine-Based Fluorescent NanoGUMBOS. *Langmuir* **2010,** *26* (15), 12867-12876.

22.     de Rooy, S. L.; Das, S.; Li, M.; El-Zahab, B.; Jordan, A.; Lodes, R.; Weber, A.; Chandler, L.; Baker, G. A.; Warner, I. M. Ionically Self-Assembled, Multi-Luminophore One-Dimensional Micro- and Nanoscale Aggregates of Thiacarbocyanine GUMBOS. *Journal of Physical Chemistry C* **2012,** *116* (14), 8251-8260.

23.     Jordan, A. N.; Das, S.; Siraj, N.; de Rooy, S. L.; Li, M.; El-Zahab, B.; Chandler, L.; Baker, G. A.; Warner, I. M. Anion-controlled morphologies and spectral features of cyanine-based nanoGUMBOS - an improved photosensitizer. *Nanoscale* **2012,** *4* (16), 5031-5038.

24.     Zhang, P.; Steelant, W.; Kumar, M.; Scholfield, M. Versatile photosensitizers for photodynamic therapy at infrared excitation. *Journal of the American Chemical Society* **2007,** *129* (15), 4526-+.

25.     Chu, M.; Shao, Y.; Peng, J.; Dai, X.; Li, H.; Wu, Q.; Shi, D. Near-infrared laser light mediated cancer therapy by photothermal effect of Fe3O4 magnetic nanoparticles. *Biomaterials* **2013,** *34* (16), 4078-4088.

26.     Tang, S.; Huang, X.; Zheng, N. Silica coating improves the efficacy of Pd nanosheets for photothermal therapy of cancer cells using near infrared laser. *Chemical Communications* **2011,** *47* (13), 3948-3950.


27.     Cai, W. B.; Shin, D. W.; Chen, K.; Gheysens, O.; Cao, Q. Z.; Wang, S. X.; Gambhir, S. S.; Chen, X. Y. Peptide-labeled near-infrared quantum dots for imaging tumor vasculature in living subjects. *Nano Letters* **2006,** *6* (4), 669-676.


28.     Frangioni, J. V. In vivo near-infrared fluorescence imaging. *Current Opinion in Chemical Biology* **2003,** *7* (5), 626-634.


29.     Giavalisco, M.; Ferguson, H. C.; Koekemoer, A. M.; Dickinson, M.; Alexander, D. M.; Bauer, F. E.; Bergeron, J.; Biagetti, C.; Brandt, W. N.; Casertano, S.; Cesarsky, C.; Chatzichristou, E.; Conselice, C.; Cristiani, S.; Da Costa, L.; Dahlen, T.; de Mello, D.; Eisenhardt, P.; Erben, T.; Fall, S. M.; Fassnacht, C.; Fosbury, R.; Fruchter, A.; Gardner, J. P.; Grogin, N.; Hook, R. N.; Hornschemeier, A. E.; Idzi, R.; Jogee, S.; Kretchmer, C.; Laidler, V.; Lee, K. S.; Livio, M.; Lucas, R.; Madau, P.; Mobasher, B.; Moustakas, L. A.; Nonino, M.; Padovani, P.; Papovich, C.; Park, Y.; Ravindranath, S.; Renzini, A.; Richardson, M.; Riess, A.; Rosati, P.; Schirmer, M.; Schreier, E.; Somerville, R. S.; Spinrad, H.; Stern, D.; Stiavelli, M.; Strolger, L.; Urry, C. M.; Vandame, B.; Williams, R.; Wolf, C. The Great Observatories Origins Deep Survey: Initial results from optical and near-infrared imaging. *Astrophysical Journal* **2004,** *600* (2), L93-L98.


30.     Gobin, A. M.; Lee, M. H.; Halas, N. J.; James, W. D.; Drezek, R. A.; West, J. L. Near-infrared resonant nanoshells for combined optical imaging and photothermal cancer therapy. *Nano Letters* **2007,** *7* (7), 1929-1934.


31.     Huang, X. H.; El-Sayed, I. H.; Qian, W.; El-Sayed, M. A. Cancer cell imaging and photothermal therapy in the near-infrared region by using gold nanorods. *Journal of the American Chemical Society* **2006,** *128* (6), 2115-2120.


32.     Ntziachristos, V.; Bremer, C.; Weissleder, R. Fluorescence imaging with near-infrared light: new technological advances that enable in vivo molecular imaging. *European Radiology* **2003,** *13* (1), 195-208.


33.     Weissleder, R.; Tung, C. H.; Mahmood, U.; Bogdanov, A. In vivo imaging of tumors with protease-activated near-infrared fluorescent probes. *Nature Biotechnology* **1999,** *17* (4), 375-378.

34. Bashkatov, A. N.; Genina, E. A.; Kochubey, V. I.; Tuchin, V. V. Optical properties of human skin, subcutaneous and mucous tissues in the wavelength range from 400 to 2000 nm. *Journal of Physics D-Applied Physics* **2005,** *38* (15), 2543-2555.

35. Klohs, J.; Wunder, A.; Licha, K. Near-infrared fluorescent probes for imaging vascular pathophysiology. *Basic Research in Cardiology* **2008,** *103* (2), 144-151.

36. Amiot, C. L.; Xu, S.; Liang, S.; Pan, L.; Zhao, J. X. Near-infrared fluorescent materials for sensing of biological targets. *Sensors* **2008,** *8* (5), 3082-3105.

37. Filonov, G. S.; Piatkevich, K. D.; Ting, L.-M.; Zhang, J.; Kim, K.; Verkhusha, V. V. Bright and stable near-infrared fluorescent protein for in vivo imaging. *Nature Biotechnology* **2011,** *29* (8), 757-U133.

38. Shcherbo, D.; Shemiakina, I. I.; Ryabova, A. V.; Luker, K. E.; Schmidt, B. T.; Souslova, E. A.; Gorodnicheva, T. V.; Strukova, L.; Shidlovskiy, K. M.; Britanova, O. V.; Zaraisky, A. G.; Lukyanov, K. A.; Loschenov, V. B.; Luker, G. D.; Chudakov, D. M. Near-infrared fluorescent proteins. *Nature Methods* **2010,** *7* (10), 827-U1520.

39. Sahyun, M. R. V.; Sharma, D. K.; Serpone, N. MECHANISMS OF SPECTRAL SENSITIZATION OF SILVER-HALIDES - ROLE OF SENSITIZING DYE COMPLEXATION. *Journal of Imaging Science and Technology* **1995,** *39* (5), 377-385.

40. Ishchenko, A. A. LASER MEDIA BASED ON POLYMETHINE DYES. *Kvantovaya Elektronika* **1994,** *21* (6), 513-534.

41. Ehret, A.; Stuhl, L.; Spitler, M. T. Spectral sensitization of TiO2 nanocrystalline electrodes with aggregated cyanine dyes. *Journal of Physical Chemistry B* **2001,** *105* (41), 9960-9965.

42. Fischer, T.; Ebert, B.; Voigt, J.; Macdonald, R.; Schneider, U.; Thomas, A.; Hamm, B.; Hermann, K.-G. A. Detection of Rheumatoid Arthritis Using Non-Specific Contrast Enhanced Fluorescence Imaging. *Academic Radiology* **2010,** *17* (3), 375-381.

43. Hagen, A.; Grosenick, D.; Macdonald, R.; Rinneberg, H.; Burock, S.; Warnick, P.; Poellinger, A.; Schlag, P. M. Late-fluorescence mammography assesses tumor capillary permeability and differentiates malignant from benign lesions. *Optics Express* **2009,** *17* (19), 17016-17033.

44.     Ntziachristos, V.; Yoo, J. S.; van Dam, G. M. Current concepts and future perspectives on surgical optical imaging in cancer. *Journal of Biomedical Optics* **2010,** *15* (6).

45.     Reynolds, J. S.; Troy, T. L.; Mayer, R. H.; Thompson, A. B.; Waters, D. J.; Cornell, K. K.; Snyder, P. W.; Sevick-Muraca, E. M. Imaging of spontaneous canine mammary tumors using fluorescent contrast agents. *Photochemistry and Photobiology* **1999,** *70* (1), 87-94.

46.     Fabian, J.; Nakazumi, H.; Matsuoka, M. NEAR-INFRARED ABSORBING DYES. *Chemical Reviews* **1992,** *92* (6), 1197-1226.

47.     Chibisov, A. K.; Zakharova, G. V.; Gorner, H. Effects of substituents in the polymethine chain on the photoprocesses in indodicarbocyanine dyes. *Journal of the Chemical Society-Faraday Transactions* **1996,** *92* (24), 4917-4925.

48.     Khimenko, V.; Chibisov, A. K.; Gorner, H. Effects of alkyl substituents in the polymethine chain on the photoprocesses in thiacarbocyanine dyes. *Journal of Physical Chemistry A* **1997,** *101* (39), 7304-7310.

49.     Strekowski, L.; Lipowska, M.; Patonay, G. SUBSTITUTION-REACTIONS OF A NUCLEOFUGAL GROUP IN HEPTAMETHINE CYANINE DYES - SYNTHESIS OF AN ISOTHIOCYANATO DERIVATIVE FOR LABELING OF PROTEINS WITH A NEAR-INFRARED CHROMOPHORE. *Journal of Organic Chemistry* **1992,** *57* (17), 4578-4580.

50.     Zhang, Z. R.; Achilefu, S. Synthesis and evaluation of polyhydroxylated near-infrared carbocyanine molecular probes. *Organic Letters* **2004,** *6* (12), 2067-2070.

51.     Fernando, N. T. Novel Near-Infrared Cyanine Dyes for Fluorescence Imaging in Biological Systems. Ph.D, Georgia State University2011.

52.     Mader, O.; Reiner, K.; Egelhaaf, H. J.; Fischer, R.; Brock, R. Structure property analysis of pentamethine indocyanine dyes: Identification of a new dye for life science applications. *Bioconjugate Chemistry* **2004,** *15* (1), 70-78.

53.     Murphy, S.; Sauerwein, B.; Drickamer, H. G.; Schuster, G. B. SPECTROSCOPY OF CYANINE DYES IN FLUID SOLUTION AT ATMOSPHERIC AND HIGH-PRESSURE - THE EFFECT OF VISCOSITY ON NONRADIATIVE PROCESSES. *Journal of Physical Chemistry* **1994,** *98* (51), 13476-13480.

54. Levitus, M.; Ranjit, S. Cyanine dyes in biophysical research: the photophysics of polymethine fluorescent dyes in biomolecular environments. *Quarterly Reviews of Biophysics* **2011,** *44* (1), 123-151.

55. Patonay, G.; Salon, J.; Sowell, J.; Strekowski, L. Noncovalent labeling of biomolecules with red and near-infrared dyes. *Molecules* **2004,** *9* (3), 40-49.

56. Volkova, K. D.; Kovalska, V. B.; Balanda, A. O.; Vermeij, R. J.; Subramaniam, V.; Slominskii, Y. L.; Yarmoluk, S. M. Cyanine dye-protein interactions: Looking for fluorescent probes for amyloid structures. *Journal of Biochemical and Biophysical Methods* **2007,** *70* (5), 727-733.

57. Eisfeld, A.; Briggs, J. S. The J- and H-bands of organic dye aggregates. *Chemical Physics* **2006,** *324* (2-3), 376-384.

58. Jelley, E. E. Spectral absorption and fluorescence of dyes in the molecular state. *Nature* **1936,** *138*, 1009-1010.

59. Scheibe, G. Über die Veränderlichkeit der Absorptionsspektren in Lösungen und die Nebenvalenzen als ihre Ursache. *Angewandte Chemie* **1937,** *50* (11), 212-219.

60. Knapp, E. W.; Scherer, P. O. J.; Fischer, S. F. ON THE LINESHAPES OF VIBRONICALLY RESOLVED MOLECULAR AGGREGATE SPECTRA - APPLICATION TO PSEUDOISOCYANIN (PIC). *Chemical Physics Letters* **1984,** *111* (4-5), 481-486.

61. Scherer, P. O. J.; Fischer, S. F. ON THE THEORY OF VIBRONIC STRUCTURE OF LINEAR AGGREGATES - APPLICATION TO PSEUDOISOCYANIN (PIC). *Chemical Physics* **1984,** *86* (3), 269-283.

62. Spano, F. C.; Siddiqui, S. Exciton-vibrational coupling in pinwheel aggregates of pi-conjugated molecules. *Chemical Physics Letters* **1999,** *314* (5-6), 481-487.

63. Gadde, S.; Batchelor, E. K.; Kaifer, A. E. Controlling the Formation of Cyanine Dye H- and J-Aggregates with Cucurbituril Hosts in the Presence of Anionic Polyelectrolytes. *Chemistry-a European Journal* **2009,** *15* (24), 6025-6031.

64. Behera, G.; Behera, P.; Mishra, B. K. Cyanine Dyes: Self Aggregation and Behaviour in Surfactants A Review. *Journal of Surface Science and Technology* **2007,** *23* (1/2), 1.

65.     Kim, S.-o.; An, T. K.; Chen, J.; Kang, I.; Kang, S. H.; Chung, D. S.; Park, C. E.; Kim, Y.-H.; Kwon, S.-K. H-Aggregation Strategy in the Design of Molecular Semiconductors for Highly Reliable Organic Thin Film Transistors. *Advanced Functional Materials* **2011,** *21* (9), 1616-1623.


66.     Bunzli, J. C. G.; Andre, N.; Elhabiri, M.; Muller, G.; Piguet, C. Trivalent lanthanide ions: versatile coordination centers with unique spectroscopic and magnetic properties. *Journal of Alloys and Compounds* **2000,** *303*, 66-74.


67.     Bunzli, J. C. G.; Piguet, C. Taking advantage of luminescent lanthanide ions. *Chemical Society Reviews* **2005,** *34* (12), 1048-1077.


68.     Benelli, C.; Gatteschi, D. Magnetism of lanthanides in molecular materials with transition-metal ions and organic radicals. *Chemical Reviews* **2002,** *102* (6), 2369-2387.


69.     Luzon, J.; Sessoli, R. Lanthanides in molecular magnetism: so fascinating, so challenging. *Dalton Transactions* **2012,** *41* (44), 13556-13567.


70.     Binnemans, K. Ionic liquid crystals. *Chemical Reviews* **2005,** *105* (11), 4148-4204.


71.     Axenov, K. V.; Laschat, S. Thermotropic Ionic Liquid Crystals. *Materials* **2011,** *4* (1), 206-259.


72.     Yu, W.; Peng, H.; Zhang, H.; Zhou, X. Synthesis and Mesophase Behaviour of Morpholinium Ionic Liquid Crystals. *Chinese Journal of Chemistry* **2009,** *27* (8), 1471-1475.


73.     Tang, S.; Babai, A.; Mudring, A.-V. Europium-based ionic liquids as luminescent soft materials. *Angewandte Chemie-International Edition* **2008,** *47* (40), 7631-7634.


74.     Mallick, B.; Balke, B.; Felser, C.; Mudring, A.-V. Dysprosium room-temperature ionic liquids with strong luminescence and response to magnetic fields. *Angewandte Chemie-International Edition* **2008,** *47* (40), 7635-7638.


75.     Getsis, A.; Balke, B.; Felser, C.; Mudring, A.-V. Dysprosium-Based Ionic Liquid Crystals: Thermal, Structural, Photo- and Magnetophysical Properties. *Crystal Growth & Design* **2009,** *9* (10), 4429-4437.

76.     Getsis, A.; Mudring, A.-V. Switchable Green and White Luminescence in Terbium-Based Ionic Liquid Crystals. *European Journal of Inorganic Chemistry* **2011,** (21), 3207-3213.


77.     Getsis, A.; Tang, S.; Mudring, A.-V. A Luminescent Ionic Liquid Crystal: C(12)mim (4) EuBr6 Br. *European Journal of Inorganic Chemistry* **2010,** (14), 2172-2177.


78.     Ji, S.-P.; Tang, M.; He, L.; Tao, G.-H. Water-Free Rare-Earth-Metal Ionic Liquids/Ionic Liquid Crystals Based on Hexanitratolanthanate(III) Anion. *Chemistry-a European Journal* **2013,** *19* (14), 4452-4461.


79.     Kido, J.; Okamoto, Y. Organo lanthanide metal complexes for electroluminescent materials. *Chemical Reviews* **2002,** *102* (6), 2357-2368.


80.     Gutowski, K. E.; Bridges, N. J.; Cocalia, V. A.; Spear, S. K.; Visser, A. E.; Holbrey, J. D.; Davis, J. H.; Rogers, R. D. Ionic Liquid technologies for utilization in nuclear-based separations. In *Ionic Liquids Iiib: Fundamentals, Progress, Challenges and Opportunities: Transformations and Processes*, Rogers, R. D.; Seddon, K. R., Eds., 2005; Vol. 902, pp 33-48.


81.     Bhatt, A. I.; May, I.; Volkovich, V. A.; Collison, D.; Helliwell, M.; Polovov, I. B.; Lewin, R. G. Structural characterization of a lanthanum bistriflimide complex, La(N(SO2CF3)(2))(3)(H2O)(3), and an investigation of La, Sm, and Eu electrochemistry in a room-temperature ionic liquid, (Me3NBu)-Bu-n N(SO2CF3)(2). *Inorganic Chemistry* **2005,** *44* (14), 4934-4940.


82.     Nockemann, P.; Thijs, B.; Postelmans, N.; Van Hecke, K.; Van Meervelt, L.; Binnemans, K. Anionic rare-earth thiocyanate complexes as building blocks for low-melting metal-containing ionic liquids. *Journal of the American Chemical Society* **2006,** *128* (42), 13658-13659.


83.     Bhargava, B. L.; Balasubramanian, S.; Klein, M. L. Modelling room temperature ionic liquids. *Chemical Communications* **2008,** (29), 3339-3351.


84.     Singh, R.; Monk, J.; Hung, F. R. Heterogeneity in the Dynamics of the Ionic Liquid BMIM+ PF6- Confined in a Slit Nanopore. *Journal of Physical Chemistry C* **2011,** *115* (33), 16544-16554.


85.     Wendler, K.; Dommert, F.; Zhao, Y. Y.; Berger, R.; Holm, C.; Delle Site, L. Ionic liquids studied across different scales: A computational perspective. *Faraday Discussions* **2012,** *154*, 111-132.

86.     Roy, D.; Maroncelli, M. An Improved Four-Site Ionic Liquid Model. *Journal of Physical Chemistry B* **2010,** *114* (39), 12629-12631.


87.     Koeddermann, T.; Paschek, D.; Ludwig, R. Molecular dynamic simulations of ionic liquids: A reliable description of structure, thermodynamics and dynamics. *Chemphyschem* **2007,** *8* (17), 2464-2470.


88.     Lue, R.; Wang, S.; Lu, Y. Density functional study on ionic liquid of 1-propyl-4,5-dibromo-3-methylimidazolium bromide. *Chemical Physics Letters* **2011,** *505* (4-6), 87-91.


89.     Guo, C.; Aydin, M.; Zhu, H. R.; Akins, D. L. Density functional theory used in structure determinations and Raman band assignments for pseudoisocyanine and its aggregate. *Journal of Physical Chemistry B* **2002,** *106* (21), 5447-5454.


90.     Gao, T.; Andino, J. M.; Raul Alvarez-Idaboy, J. Computational and experimental study of the interactions between ionic liquids and volatile organic compounds. *Physical Chemistry Chemical Physics* **2010,** *12* (33), 9830-9838.


91.     Shukla, M.; Srivastava, N.; Saha, S. Theoretical and spectroscopic studies of 1-butyl-3-methylimidazolium iodide room temperature ionic liquid: Its differences with chloride and bromide derivatives. *Journal of Molecular Structure* **2010,** *975* (1-3), 349-356.


92.     Singh, R.; Monk, J.; Hung, F. R. A Computational Study of the Behavior of the Ionic Liquid BMIM+ PF6- Confined Inside Multiwalled Carbon Nanotubes. *Journal of Physical Chemistry C* **2010,** *114* (36), 15478-15485.


93.     Mendez-Morales, T.; Carrete, J.; Garcia, M.; Cabeza, O.; Gallego, L. J.; Varela, L. M. Dynamical Properties of Alcohol+1-Hexyl-3-methylimidazolium Ionic Liquid Mixtures: A Computer Simulation Study. *Journal of Physical Chemistry B* **2011,** *115* (51), 15313-15322.


94.     Shi, H.-p.; Xu, L.; Cheng, Y.; He, J.-y.; Dai, J.-x.; Xing, L.-w.; Chen, B.-q.; Fang, L. Experimental and theoretical study of three new benzothiazole-fused carbazole derivatives. *Spectrochimica Acta Part a-Molecular and Biomolecular Spectroscopy* **2011,** *81* (1), 730-738.


95.     Hu, N. X.; Xie, S.; Popovic, Z.; Ong, B.; Hor, A. M.; Wang, S. N. 5,11-Dihydro-5,11-di-1-naphthylindolo 3,2-b carbazole: Atropisomerism in a novel hole-transport molecule for organic light-emitting diodes. *Journal of the American Chemical Society* **1999,** *121* (21), 5097-5098.

96.     Hwang, S. W.; Chen, Y. Photoluminescent and electrochemical properties of novel poly(aryl ether)s with isolated hole-transporting carbazole and electron-transporting 1,3,4-oxadiazole fluorophores. *Macromolecules* **2002,** *35* (14), 5438-5443.

97.     Kundu, P.; Thomas, K. R. J.; Lin, J. T.; Tao, Y. T.; Chien, C. H. High-Tg carbazole derivatives as blue-emitting hole-transporting materials for electroluminescent devices. *Advanced Functional Materials* **2003,** *13* (6), 445-452.

98.     Li, J. Y.; Liu, D.; Li, Y. Q.; Lee, C. S.; Kwong, H. L.; Lee, S. T. A high Tg carbazole-based hole-transporting material for organic light-emitting devices. *Chemistry of Materials* **2005,** *17* (5), 1208-1212.

99.     Paik, K. L.; Baek, N. S.; Kim, H. K.; Lee, J. H.; Lee, Y. White light-emitting diodes from novel silicon-based copolymers containing both electron-transport oxadiazole and hole-transport carbazole moieties in the main chain. *Macromolecules* **2002,** *35* (18), 6782-6791.

100.    Brunner, K.; van Dijken, A.; Borner, H.; Bastiaansen, J.; Kiggen, N. M. M.; Langeveld, B. M. W. Carbazole compounds as host materials for triplet emitters in organic light-emitting diodes: Tuning the HOMO level without influencing the triplet energy in small molecules. *Journal of the American Chemical Society* **2004,** *126* (19), 6035-6042.

101.    van Dijken, A.; Bastiaansen, J.; Kiggen, N. M. M.; Langeveld, B. M. W.; Rothe, C.; Monkman, A.; Bach, I.; Stossel, P.; Brunner, K. Carbazole compounds as host materials for triplet emitters in organic light-emitting diodes: Polymer hosts for high-efficiency light-emitting diodes. *Journal of the American Chemical Society* **2004,** *126* (24), 7718-7727.

102.    Agarwal, N.; Nayak, P. K.; Ali, F.; Patankar, M. P.; Narasimhan, K. L.; Periasamy, N. Tuning of HOMO levels of carbazole derivatives: New molecules for blue OLED. *Synthetic Metals* **2011,** *161* (5-6), 466-473.

103.    Belletete, M.; Bedard, M.; Leclerc, M.; Durocher, G. Ground and excited state properties of carbazole-based dyads: correlation with their respective absorption and fluorescence spectra. *Journal of Molecular Structure-Theochem* **2004,** *679* (1-2), 9-15.

**CHAPTER 2 IRRADIATION INDUCED FLUORESCENCE ENHANCEMENT IN PEGYLATED CYANINE-BASED NIR NANO-AND MESO-SCALE GUMBOS**

## 2.1 Introduction

Fluorescent nanoparticles have been widely studied as diagnostic and thermal therapeutic agents with applications to tumor imaging and targeted cancer drug delivery. [1, 2, 3, 4, 5, 6, 7] Nanoparticles that can absorb and emit light in the near-infrared (NIR) region are of great interest in biomedical applications since the skin has minimum absorption coefficient and maximum penetration depth for electromagnetic radiation in the NIR region.[8, 9] There are numerous fluorescent NIR materials or molecules available which can be employed to provide fluorescence property in nanoparticles. These include quantum dots,[10, 11] fluorescent protein,[12, 13] gold/silver nanoparticles[14], and fluorescent NIR organic molecules.[8, 15, 16, 17] Among these, NIR organic dyes are the most frequently used fluorophores in fluorescent probes for imaging vascular pathophysiology and other disorders.[9, 18] Two methods have been developed to prepare fluorescent NIR organic nanoparticles. One involves encapsulation of organic molecules in nanocomposite particles;[9] the other uses a reprecipitation method to prepare nanoparticles employing water-insoluble dyes.[19, 20]

Among various organic fluorescent NIR dyes, heptamethine cyanine dyes are promising candidates due to their high molar extinction coefficients and broad wavelength tunability.[21, 22] However, when used as optical contrast agents, the heptamethine cyanine dyes suffer from several disadvantages. These major disadvantages which limit the application of cyanine dyes for biomedical applications include low quantum yields, self-assembly to form non-

_____

fluorescent aggregates, short fluorescence lifetime, poor photostability, cytotoxicity, non-specific binding to proteins and other cell components[23], and small Stokes shifts.[24] To improve the properties of heptamethine cyanine dyes, much effort has been directed toward modification of the molecular structures of these dyes. For example, studies have demonstrated that cyanine dyes which incorporate a rigid cyclohexenyl ring in the heptamethine chain have increased photostability and enhanced quantum yield as compared to cyanine dyes with an open polymethine chain.[25] In addition, cyanine dyes with two sulfonic groups or carboxyl groups have improved photostability, increased water solubility, as well as greater biocompatibility. For example, indocyanine green (ICG), a cyanine dye with two sulfonic groups, has been approved by the U.S Food and Drug Administration (FDA) for human use due to its low toxicity ($LD_{50}$ of 50-80 mg/kg for animal subjects).[9]

For most heptamethine cyanine dyes, Stokes shifts are often less than 25 nm, which can result in self-quenching and measurement errors from excitation and scattered light.[24] Peng, et al. have reported new cyanine dyes which have large Stokes shifts (>140 nm)[26]. These new dyes are derived from cyanine dyes containing a central cyclohexenyl ring in the heptamethine chain. A robust C-N bond substitution at the C-Cl bond on the rigid ring leads to a large Stoke shift due to excited-state intramolecular charge transfer (ICT) between a donor and acceptor in the dyes. However, most of these modifications were employed using cyanine dyes which are water soluble. Water soluble dyes cannot self-assemble to produce nanoparticles in aqueous solution using a reprecipitation method. In contrast, the research reported in this manuscript focuses on modification of water insoluble heptamethine cyanine dyes to produce stable self-assemblies in aqueous solution by use of reprecipitation.

PEG is a water soluble and biocompatible polymer that has been widely used to modify the surface properties of various nanoparticles.[27, 28, 29, 30] The surface properties of nanoparticles, e.g. hydrophobicity, play an important role in stabilizing such nanoparticles,

which in turn determines the *in vivo* fate of these nanoparticles. It is well established that nanoparticles with hydrophobic surfaces are rapidly captured and massively cleared by the mononuclear phagocyte system (MPS). Upon PEGylation, the hydrophilicity of the PEG chain will typically prevent such nanoparticles from being recognized by MPS.[31] Moreover, PEG chains extend into the aqueous pool and provide a sphere of solvation in water , thus preventing such dyes from aggregating.[32] In addition, a PEG shell has the potential of reducing non-specific binding to proteins[33] , as well as reducing cytotoxicity. [34]

Our group has recently reported a series of organic salts which are similar to ionic liquids, but do not fit the accepted definition of ionic liquids since they often have melting points greater than 100 $^{\circ}$C.[19, 20] We have defined these materials as a **g**roup of **u**niform **m**aterials **b**ased on **o**rganic **s**alts and use the acronym, GUMBOS, to describe these materials with melting points between 25 ℃ and 250 ℃.  As used here, GUMBOS can be singular and plural.

Cyanine dyes are typically either cationic or anionic organic salts. Dyes with two sulfonic groups or carboxyl groups are anionic salts with typically small counter cations, such as sodium.  Dyes without negatively charged groups are cationic salts with counter anions, such as iodide ion. Since various anions are available for conversion to GUMBOS, cationic cyanine dye based GUMBOS can be obtained by use of anion-exchange. It has been demonstrated that cationic cyanine dyes coupled with various anions display tunable spectral properties in aqueous solutions.[20] Therefore, in this article, selection of a water insoluble cyanine dye (cationic) for modification is based on considerations of exploiting these anion-controlled spectral properties.

In this study, in order to achieve large stokes shift, lower non-specific binding to proteins, and to reduce cytotoxicity, 6-aminohexanoic acid linked with PEG was used to modify IR786, which is normally a water insoluble cationic NIR dye with a rigid

cyclohexenyl ring in the heptamethine chain. The modified dye based GUMBOS were obtained by use of anion exchange with sulfosuccinate (AOT) sodium salt and lithium bis(trifluoromethane) sulfonamide (NTf$_2$), respectively. In this manuscript, we demonstrate that PEGylated dye-based GUMBOS show increased Stokes shifts and can form nano- and meso-sized self-assemblies in aqueous solution. The nano- and meso-scale GUMBOS also displayed anion and concentration dependent photostability as a result of irradiation. The PEG chains provide a protective outer layer for improving steric stabilization and reducing non-specific binding to protein and cytotoxicity.

## 2.2 Experimental Methods

### 2.2.1 Materials

IR786 iodide, 6-aminohexanoic acid, DMF, polyethylene glycol monomethyl ether (MeOPEG, Mn=550), 1, 3-dicyclohexylcarbodiimide (DCC), bis(2-ethylhexyl) sulfosuccinate (AOT) sodium salt (≥99%), and lithium bis(trifluoromethane) sulfonamide (NTf$_2$) were all purchased from Sigma-Aldrich and used as received. Four (4)-(Dimethylamino)pyridine (DMAP) and triethylamine were obtained from Fluka and Fisher Scientific respectively. Triply deionized water (18.2MΩ cm), obtained from an Elga model PURELAB ultra water-filtration system, was used for the preparation of all PEGylated NIR dye samples.

### 2.2.2 Synthesis of PEG786 GUMBOS

The PEGylated NIR GUMBOS were synthesized by use of a two-step procedure followed by an anion exchange reaction. In the two-step reaction, 6-aminohexanoic acid was first attached to IR786 iodide ([IR786][I]) using a method described in the literature[22]. In this procedure, triethylamine (198 μL, 1.42 mmol) and 6-aminohexanoic acid (126 mg, 1.42 mmol) were added to a solution of IR786 iodide (0.283 mmol) in anhydrous DMF (10 mL) under nitrogen atmosphere. After stirring for 3 h at 85 ℃, the green solution changed to a blue

solution. Flash chromatography (AcOEt/MeOH 70/30 to 0/100) was used to obtain a pure blue product (yield 85%). Subsequently, 0.03 g of MeOPEG (0.06 mmol) and 0.02g of N, N-dimethylaminopyridine (DMAP) were dissolved in 10 mL of anhydrous DMSO. In a separate vessel, 0.0466 g of the blue compound (0.06 mmol) was dissolved into 10 mL of anhydrous DMSO together with 0.0124 g N, N -dicyclo-hexylcarbodiimide (DCC, 0.06 mmol). The mixture was stirred for 30 min at room temperature and then added to the above MeOPEG solution. This reaction mixture was then agitated for 2 days at room temperature (yield 75%).

An anion exchange method similar to those reported in the literature was employed to prepare PEG786 GUMBOS.[20] Equimolar amounts of PEG786 iodide([PEG786][I]) and sodium bis(2-ethylhexyl) sulfosuccinate (AOT) salt were dissolved in a mixture of methylene chloride and water (2:1 v/v) and stirred for 12 h at room temperature. The methylene chloride bottom layer was washed several times with fresh water to remove the byproduct, NaI. The product ([PEG786][AOT], yield 80%) was obtained from the lower organic layer and dried after solvent removal under vacuum. A similar anion-exchange procedure was employed for preparation of [PEG786][NTf$_2$].

### 2.2.3 Preparation and Characterization of PEG786 nano- and meso-scale GUMBOS

The PEG786 nano- and meso-scale GUMBOS were prepared from PEG786 GUMBOS by use of a reprecipitation method which has been previously described in the literature. [19, 20] A given amount (1-70μL) of a 1 mM GUMBOS ethanolic solution of the GUMBOS was rapidly injected into 1 mL of triply deionized water in an ultrasonic bath, followed by additional sonication for 5 min.

The average particle sizes and morphologies of the prepared PEG786 nano- and meso-scale GUMBOS were obtained using transmission electron microscopy (TEM). These TEM micrographs were recorded by use of an LVEM5 transmission electron microscope (DelongAmerica, Montreal, Canada). A small amount of PEG786 nano- andmeso-scale

48

GUMBOS in aqueous solution was drop cast onto a carbon-coated copper grid and allowed to dry in air at room temperature before TEM imaging. Electron diffraction measurements of the dried nano- and meso-scale GUMBOS were obtained on a Nonius Kappa CCD diffractometer through long exposure to Mo KR radiation and rotation of samples about the vertical axis.

### 2.2.4 Absorption and Fluorescence Studies of PEG786 nano- and meso-scale GUMBOS

For all spectroscopic measurements, samples were placed in a low-volume fluorescence cuvet and held in place by use of a modified cuvet holder. UV-Vis-NIR absorption spectra were recorded using a UV-3101PC UV-Vis-NIR scanning spectrophotometer (Shimadzu). UV-Vis-NIR absorbance was performed and monitored in the wavelength range from 200 nm to 900 nm. Fluorescence spectra were recorded at room temperature by use of a Spex Fluorolog-3 spectrofluorimeter (model FL3-22TAU3; Jobin Yvon, Edison, NJ, USA) equipped with a 450-W xenon lamp and R928P photomultiplier tube (PMT) emission detector. The photostabilities of these PEG-modified dyes were evaluated in aqueous solution by excitation at 630 nm for 3000 seconds with 14nm slit width.

Fluorescence lifetime measurements were performed on a Spex Fluorolog-3 spectrofluorimeter (model FL3-22TAU3, Jobin Yvon, Edison, NJ) using time domain mode. A picosecond pulsed excitation source of 735 nm was used and emission collected at 760 nm with a TBX detector. The time correlated single photon counting (TSCPC) mode was used for data acquisition with a resolution of 7 ps/channel.

### 2.2.5 Study of Resistance to Non-specific Protein Adsorption

Absorption difference spectroscopy was used to study the resistance of PEG786 nano- and meso-scale GUMBOS to protein adsorption. Differential spectral titrations were performed at room temperature. [35] The concentration of the dye in the reference cuvet and the dye in the dye/BSA mixture were identical. The conditions employed were as follows:

1. At a constant dye concentration of 20 μM in PBS solutions (pH = 7.4), the BSA concentration was varied as follows: 0.1mg/mL, 0.2 mg/mL, 0.3 mg/mL, 0.4 mg/mL, 0.5 mg/mL, and 0.6 mg/mL;

2. At a constant concentration of 0.5 mg/mL BSA in PBS solutions (pH=7.4), the dye concentration was increased from 5 μM to 20 μM;

3. The dye and BSA mixtures were then incubated for 1 hour before UV-vis-NIR absorption measurements.

## 2.2.6 In vitro Cytotoxicity Assay

Cytotoxicities of IR786 and PEG786 GUMBOS against HeLa cancer cell line was determined by use of MTT Assay kit (Promega Corporation, Madison, WI, USA) according to the manufacturer's instructions. Briefly, in a 96-well plate, 5000 cells in 0.1 mL culture medium were seeded to each well. After 24 h, the old culture medium was removed and discarded and 0.1 mL of new culture medium containing 0-40 μM [IR786][I] or PEG786 GUMBOS dissolved in 1% DMSO was introduced to the cells. The cells were then incubated for 48 h at 37 ℃, in 5% $CO_2$ atmosphere. At the end of the incubation period, the cells were treated with 15 μL 3-(4, 5-Dimethylthiazol-2-yl)-2, 5-diphenyltetrazolium bromide (MTT) and incubated for 4 h. After four hours 100 μL of the stock solution was added per well and incubated overnight. The plate was shaken for 20 seconds and absorbance was then read at 570 nm with a reference wavelength of 650 nm using a micro plate spectrophotometer (Benchmark Plus, Bio-Rad Laboratories, Hercules, CA, USA). Cell viability as a percentage was determined by taking the ratio between absorbance of the treated cells and the absorbance of untreated (control) cells taken as 100%.

## 2.3 Results and Discussion

The position of the chloride on the central cyclohexenyl ring of [IR786][I] is considered to be a useful reaction site for further structural modification. Six(6)-aminohexanoic acid, which has two functional groups, was linked to IR786 by use of an $S_{NR}1$ reaction (Scheme 2.1, first reaction) to obtain a blue product [IR786AA][I]. Afterwards, polyethylene glycol monomethyl ether (MeoPEG) was attached to 6-aminohexanoic acid by use of an esterification reaction between the carboxyl and hydroxyl groups (Scheme 2.1, second reaction). Finally, the PEG786 GUMBOS were synthesized employing an anion exchange between [PEG786][I] and bis(2-ethylhexyl) sulfosuccinate (AOT) sodium salt (≥99%), lithium bis(trifluoromethane) sulfonamide ($NTf_2$) (Scheme 2.1, third reaction).

[IR786AA][I] characterization: ^{1}HNMR ($CDCl_3$): δ (ppm) 10.0 (1H), 8.02 (s, 2H), 7.37 (s, 2H), 7.05 (t, 2H), 6.87 (d, 4H), 5.60 (m, 2H), 3.84 (t, 3H), 3.28 (s, 3H), 2.96 (s, 4H), 2.49 (t, 2H), 1.99 (t, 1H), 1.69 (m, 8H), 1.44 (m, 4H), 1.38 (s, 6H), 1.26 (m, 2H); ESI-MS: Calculated $m/z$ =578.80 , Found $m/z$ =578.38

[PEG786][I] characterization: ^{1}HNMR ($CDCl_3$): δ (ppm) 8.12 (d, 1H), 7.65 (d, 1H), 7.22 (m, 2H), 7.16(m, 1H), 6.98 (d, 2H), 6.88 (t, 1H), 6.79 (d, 1H), 6.67(d, 1H), 5.37(t, 2H), 3.78 (m, 2H), 3.68 (m, 2H), 3.68 (s, 3H), 3.62 (m, 44H), 3.52 (s, 3H), 3.35 (s, 3H), 3.26 (m, 3H), 2.47(t, 4H), 2.35 (t, 2H), 2.14 (s, 1H), 1.67 (m, 10H), 1.27 (m, 10H). ^{13}CNMR ($CDCl_3$): δ (ppm) 171.56 (3C), 144.62 (2C), 139.61 (1C), 136.40 (2C), 132.69 (2C), 127.92 (2C), 127.61 (1C), 126.88 (1C), 122.09, 121.96, 121.69, 120.46 (4C), 106.39, 107.45 (3C), 72.60,71.93, 70.56, 70.29 (24C), 61.66, 58.98 (2C), 50.98, 49.95, 49.71 (1C), 46.41 (1C), 35.86, 34.33 (2C), 32.44 (1C), 29.76, 29.25 (2C), 28.77 (1C), 26.25, 26.15 (3C), 25.86, 25.41, 25.02, 24.62, 24.32 (4C). ); ESI-MS: Found $m/z$ =784.56
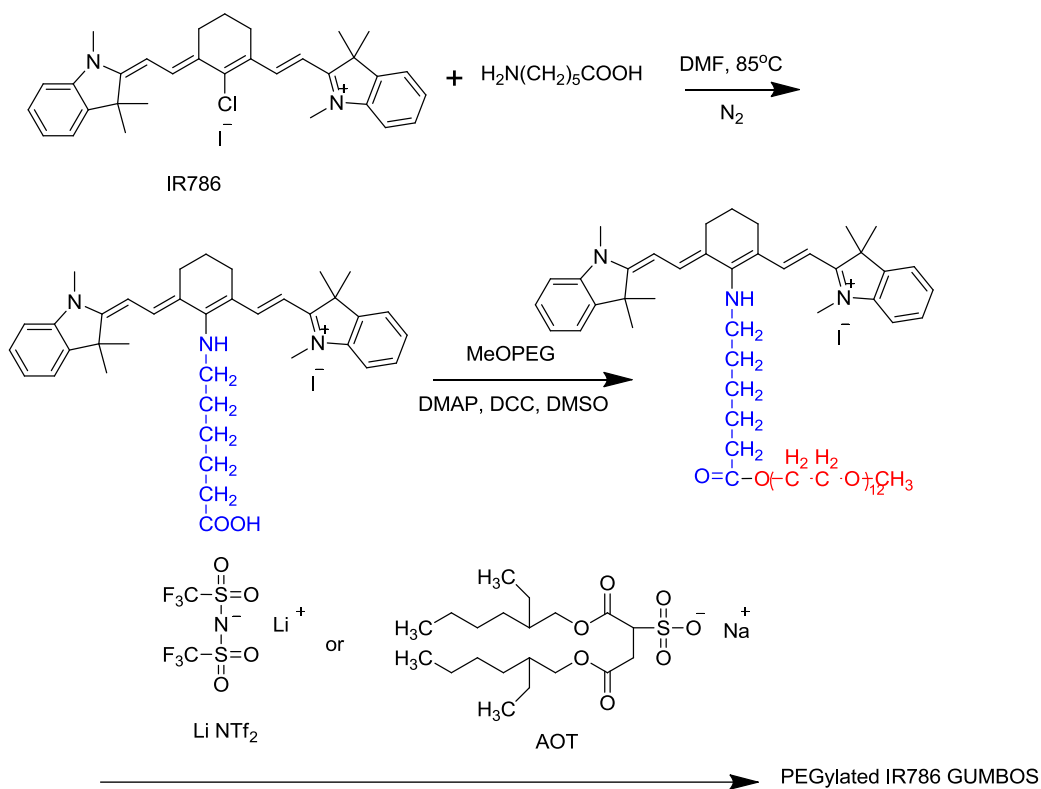
Scheme2. 1 Synthesis of PEG786 based GUMBOS

PEG786 GUMBOS formed nano-sized self-assemblies in aqueous solution when a reprecipitation method was employed.[19,20] These nano- and meso-scale GUMBOS were characterized using transmission electron microscopy (TEM) (Figure 2.1). The TEM images of [PEG786][NTf$_2$] show that these nano- and meso-scale GUMBOS were primarily spherical with average diameters in the range of 100 to 220 nm; while [PEG786][I] nano- and meso-scale GUMBOS displayed both spherical and quasi-spherical particles with average size ranging from 100 to 150 nm.
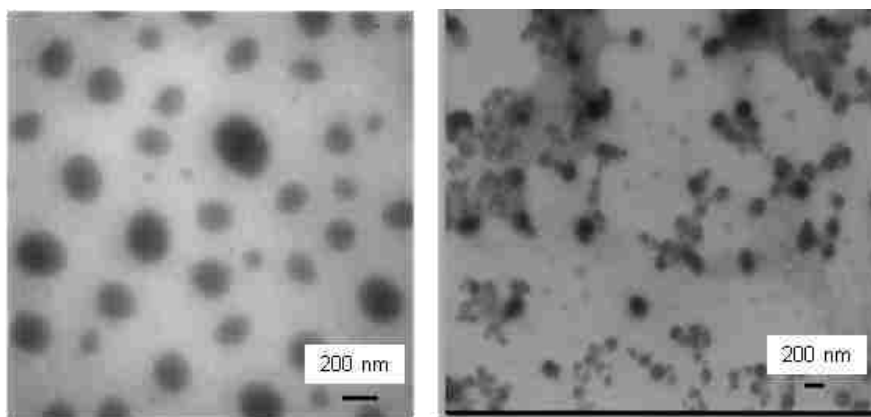
Figure2. 1 Transmission electron micrograms of [PEG786][NTf2] (left) and [PEG786][I] (right) nano- and meso-scale GUMBOS

## 2.3.1 Spectroscopic Analysis of PEG786 GUMBOS

The PEG786 GUMBOS exhibited broader spectra as compared to the original unmodified IR786 (Figure 2.2). The absorption maxima of [PEG786][I] was observed at 620 nm which was 150 nm blue shifted as compared to its non-PEGylated counterpart. A large Stokes shift of 122 nm was also observed as compared to IR786 with a Stokes shift of 25 nm. The significant increase in Stokes shift after substitution of C-Cl bond with a C-N bond on the central ring is attributed to intramolecular charge transfer (ICT).[26] After structural modification, the nitrogen binding to the cyclohexenyl ring results in a bridgehead amine, which leads to intramolecular charge transfer (ICT). Accompanying ICT, a locally excited (LE) state (pyramidal geometry) is formed after excitation, and then transformed into an ICT state (planar configuration).[26] This process is illustrated in Figure 2.3.
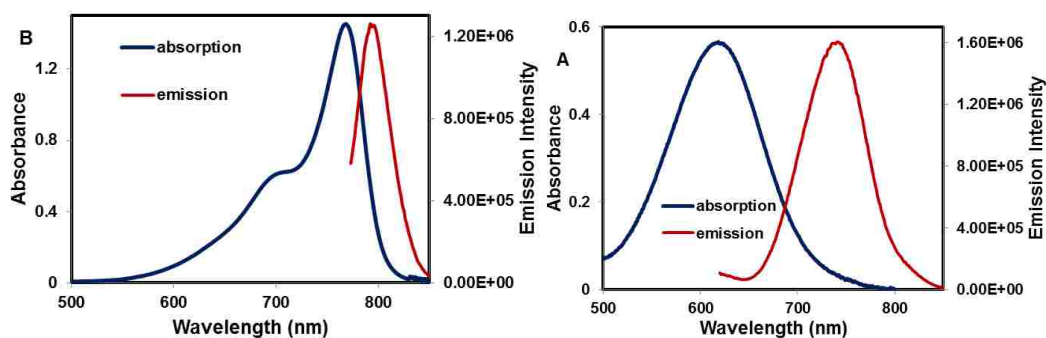


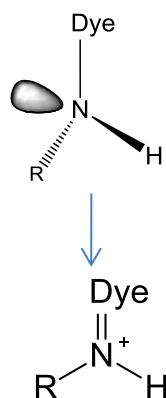Figure2. 2 Absorption (blue) and emission (red) spectra of [PEG786][I] (A) and IR786 (B) in EthanlEwater

53

Figure2. 3 Transformation of pyramidal geometry to planar configuration

## 2.3.2. Photostability of PEG786 Nano- and meso-scale GUMBOS

The stability of dyes, including the ability to resist degradation from light, heat, oxygen, and ozone, is important for spectroscopic applications.[36] For example, as optical contrast agents, cyanine dyes should have high photostability in order to improve their lifetimes for laser operation. In order to track the photobleaching of PEG786 GUMBOS, aqueous solutions of this compound were irradiated by use of a xenon lamp (630nm, slits 14/14) over a period of 50 min to examine irradiation photostability. A decrease in the emission maxima over time was recorded and is illustrated in Figures 2.4. As seen in Figure 2.4 A, at a concentration of 20 μM, the photostability of [PEG786][AOT] was much higher than that of [PEG786][NTf$_2$] and [PEG786][I]. [PEG786][I] has the lowest photostability with a residual emission intensity of 15%. The residual emission intensity for [PEG786][AOT] and [PEG786][NTf$_2$] are 57% and 35%, respectively.
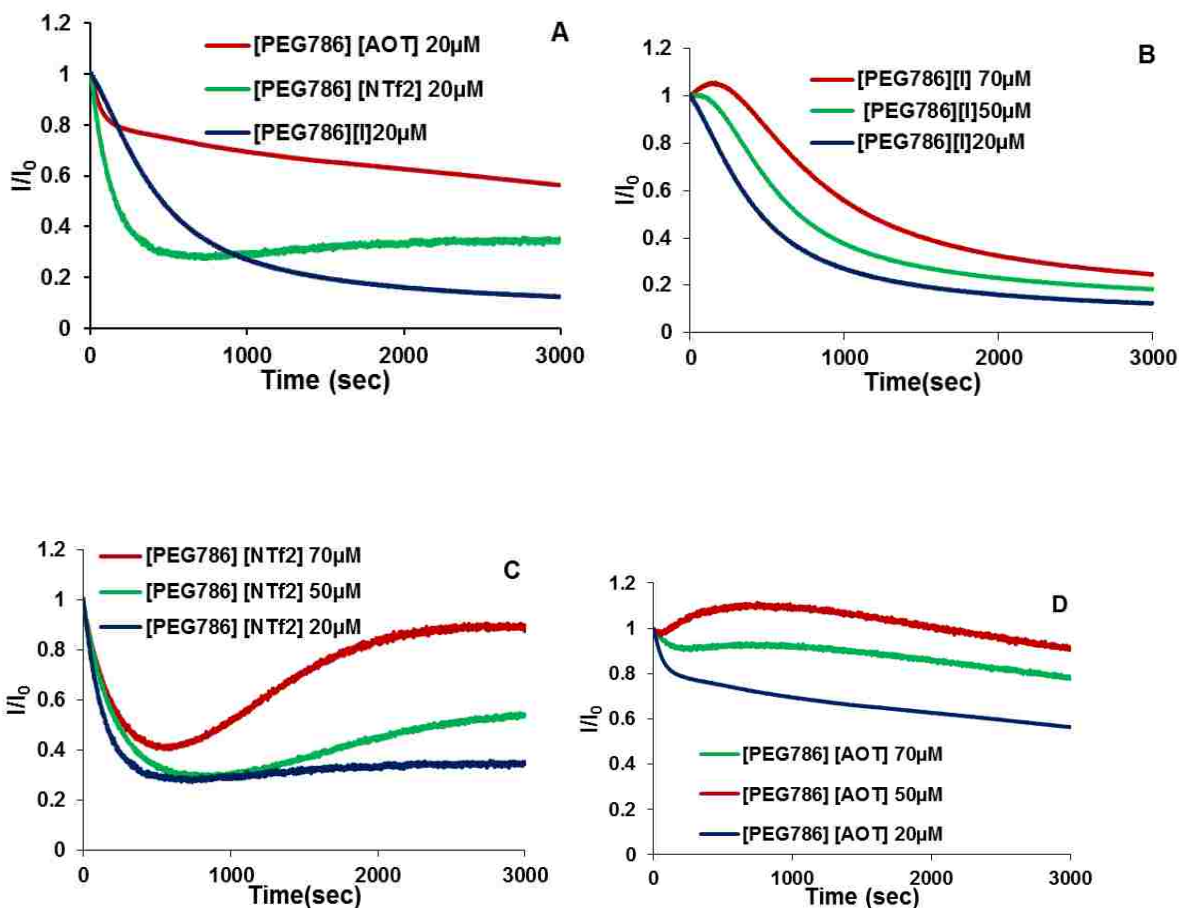
Figure2. 4 Effects of anions (A) and concentration (B, C, D) on photostability of PEG786 nano- and meso-scale GUMBOS

The effect of concentration on photostability of PEG786 GUMBOS in aqueous solution was also investigated. The results shown in Figure 2.4 B, C and D indicate that photostability of three PEG786 nano- and meso-scale GUMBOS from 20 μM to 70 μM in water. It was observed that for [PEG786][I] the photostability dropped at all concentrations over a period of 50 min. However, for [PEG786][NTF$_2$] nano- and meso-scale GUMBOS, the higher concentrations exhibited an increase in fluorescence intensity after irradiating for more than 500 sec. Similar behavior was observed for [PEG786][AOT] at higher concentrations.

The emission spectrum of [PEG786][NTf$_2$] has a maximum at 742 nm and a shoulder at 798 nm (Figure 2.5 A). Interestingly, it was observed that the photostability of [PEG786][NTF$_2$] increased upon short irradiation at all concentrations when the emission

was collected at the shoulder (798 nm). Data from Figure 2.5 B demonstrates that the ratio of residual emission intensity to emission intensity before irradiation at 798 nm was much higher than that at 742 nm: ratios of 65%, 160% and 160% at 798 nm were obtained as compared to 35%, 53% and 90% at 742nm with respective concentrations of 20 μM, 50 μM and 70 μM. The sharp increase in emission intensity at 798 nm after irradiation as compared to that before irradiation suggests that a new emitting species is formed due to irradiation which emits near 798 nm and has a higher quantum yield as compared to the initial emitting species.
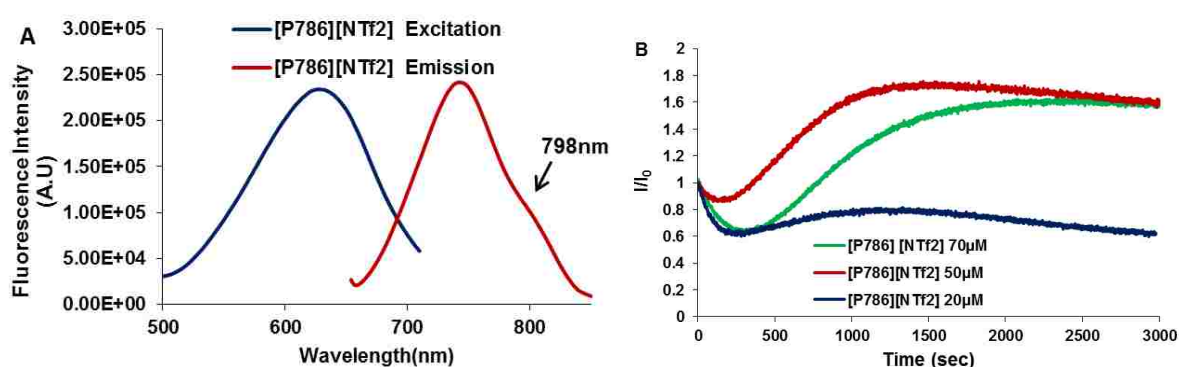


Figure2. 5 Photostability study of [PEG786][NTf2] with emission wavelength at 798nm

Emission and excitation spectra of PEG786 nano- and meso-scale GUMBOS were obtained before and after irradiation. As a comparison, emission and excitation spectra without irradiation were also investigated to identify the new emitting species and understand the mechanism of formation. Figure 2.6 A shows the excitation and emission spectra of [PEG786][NTf$_2$] (50 μM) before and after irradiation. Both the excitation and emission maxima exhibited a red shift after 50 min of irradiation. The excitation maximum shifted from 625 nm to 640 nm and the emission maximum shifted from 640 nm to 773 nm. These new maxima were ascribed to the new emitting species, which needs identification. Time studies of [PEG786][NTf$_2$] aqueous solution without irradiation were performed by recording the excitation and emission spectra at 15 -min interval. The final spectrum was recorded at 50

minutes. The results are shown in Figure 2.6 B and C. No peak shift was observed during time studies, which indicates that formation of the new emitting species is induced by irradiation rather than time. Moreover, such a phenomenon was not observed at 1 μM which is an extremely low concentration for induction of dye aggregation. This observation further suggests that the new emitting species is a molecular aggregate formed as a result of higher concentration and irradiation. Irradiation-induced J-aggregation has been reported for other cyanine dyes with different templates.[37] J aggregates are usually characterized by red-shifted absorption and intense fluorescence as compared to the corresponding monomeric species.[36]

In order to further verify irradiation induced J-aggregation formation, fluorescence lifetime measurements were performed. These measurements for [PEG786][NTf$_2$] nano- and meso-scale GUMBOS in water revealed an extremely short component of 69 ps after irradiation. This was the only emitting species as compared to before irradiation which was composed of a longer component of 349 ps. However, as noted, at the lower non-aggregation concentration of 1 μM, the appearance of a shorter component was not observed in the fluorescence lifetime measurements after irradiation. Similar results were obtained for [PEG786][AOT] nano- and meso-scale GUMBOS at higher concentrations. These results are summarized in Table 2.1. J-aggregation is often characterized by short lifetimes and enhanced fluorescence. Thus, the combination of steady state fluorescence, kinetic studies, and fluorescence lifetime confirms irradiation induced J-aggregation and enhanced fluorescence of the PEGylated nano- and meso-scale GUMBOS.
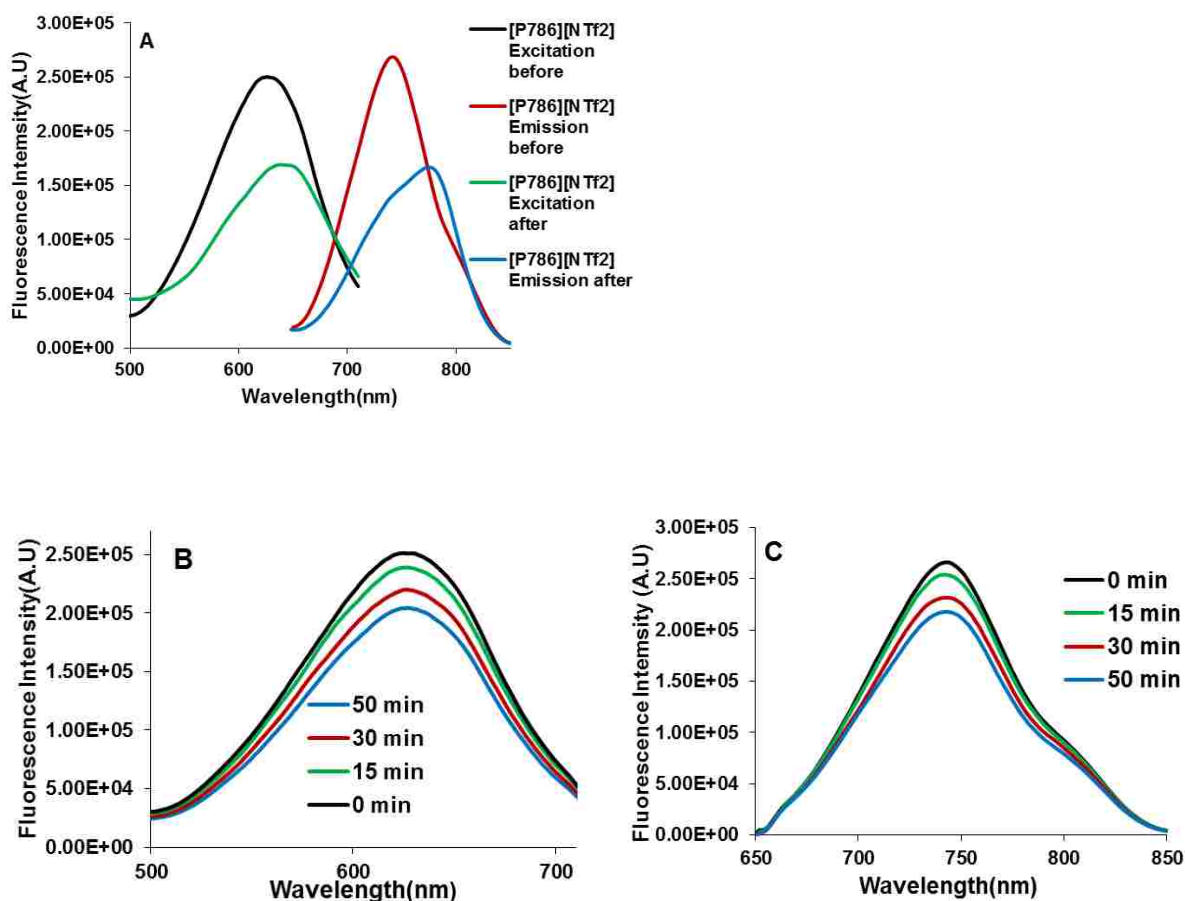
Figure2. 6 Excitation (left) and emission (right) (A) spectra of [PEG786][NTf2] (50uM) before and after irradiation. Excitation (B) and emission (C) spectra of [PEG786][NTf2] (50uM) without irradiation

Table2. 1 Lifetime of [PEG786][AOT] and [PEG786][NTf2] before and after irradiation

| System | $\tau1$ | a1 | $\tau2$ | a2 | $\chi$ |
|---|---|---|---|---|---|
| **1$\mu$M [PEG786][AOT] before irradiation** | 243 ps | 1 | | | 1.4 |
| **1$\mu$M [PEG786][AOT] after irradiation** | 172 ps | 1 | | | 1.3 |
| **50$\mu$M [PEG786][AOT] before irradiation** | 23.5 ps | 0.7 | 325 ps | 0.3 | 1.5 |
| **50$\mu$M [PEG786][AOT] after irradiation** | 32.3 ps | 0.9 | 190 ps | 0.1 | 1.5 |
| **1$\mu$M [PEG786][NTf$_2$] before irradiation** | 146 ps | 1 | | | 1.4 |
| **1$\mu$M [PEG786][NTf$_2$] after irradiation** | 272 ps | 1 | | | 1.2 |
| **50$\mu$M [PEG786][NTf$_2$] before irradiation** | 349 ps | 1 | | | 1.2 |
| **50$\mu$M [PEG786][NTf$_2$] after irradiation** | 69 ps | 0.99 | 395 ps | 0.01 | 1.8 |

### 2.3.3 Studies of Resistance to Nonspecific Protein Adsorption

Absorption difference spectroscopy is often used to study the interaction between dyes and proteins.[35] The absorption spectrum of the unmodified dye [IR786][I] in water has a broad maximum at 764 nm (Figure 2.7). In contrast, the spectrum of [IR786][I] in the presence of BSA is characterized by a maximum at 785 nm with a narrow peak. Thus, a considerable difference in absorbance was observed due to formation of an IR786-BSA complex. For determination of the dye-BSA binding process, 20 μM of unmodified [IR786][I] was titrated with increasing amounts of BSA, and 0.5 mg/mL of BSA was titrated with increasing amounts of [IR786][I]. The intensity of the 785 nm peak in each spectrum was plotted against the BSA concentration (Figure 2.8 A), or dye concentration (Figure 2.8 B). In both studies, the plots appeared to be linear. These results suggest that the [IR786][I] has a strong interaction with BSA, and the dye-BSA complex concentration is directly proportional to both the dye and BSA concentration.
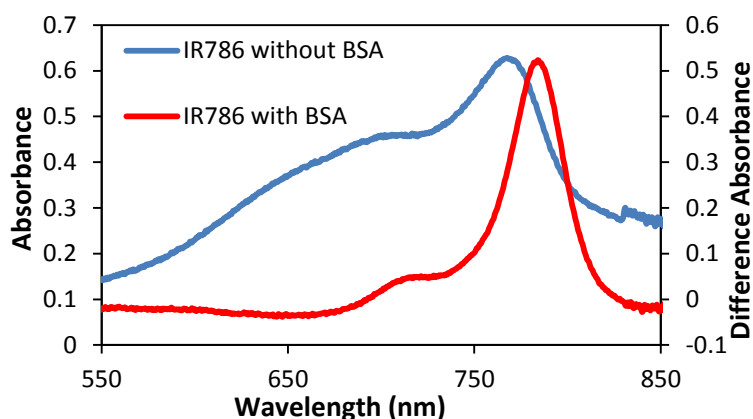


Figure2. 7 Spectrum of 20 μM of [IR786][I] in 0.1 M PBS pH 7.0 (blue) and different spectrum for IR786 binding to BSA in the same buffer (red). The BSA concentration in the sample cuvette was 0.5 mg/mL and the dye concentration in both the sample and reference cuvettes was 20 μM
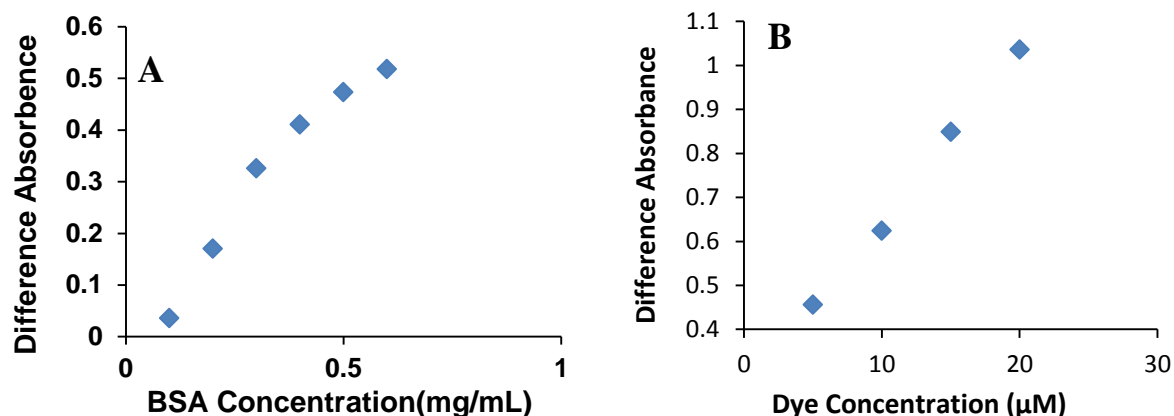
Figure2. 8 Titration at λ=785 nm of BSA with IR786 in PBS, pH=7.0. The dye concentration in the sample cuvettes was 20 μM (A); the BSA dye concentration in the sample cuvettes was 0.5 mg/mL(B).

Similar studies to those described in the previous paragraph were conducted between PEGylated dye, [PEG786][I], and BSA. A difference in absorbance was observed in [PEG786][I] and BSA mixture compared to [PEG786][I] in PBS solution ( Figure 2.9). A peak shift from 625 nm to 645 was ascribed to the presence of PEG786 – BSA complex. Evaluation of the titration studies showed that the titration curve was saturated at a concentration of 0.3 mg/mL BSA with a constant dye concentration (Figure 2.10 C). When the BSA concentration was held constant at 0.5 mg/mL, increasing the dye concentrations showed negligible effect on the intensity of the 645 nm peak for difference spectra (Figure 2.10 D). Therefore, [PEG786][I]   interacts very weakly with BSA and  binding to BSA follows a saturation curve.
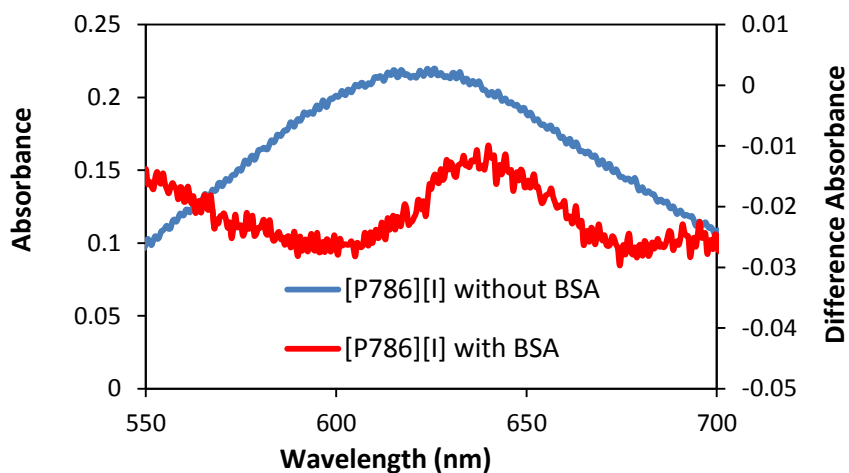
Figure2. 9 Spectrum of 20 μM of [PEG786][I] in 0.1 M PBS pH 7.0 (blue) and difference spectrum for [PEG786][I] binding to BSA in the same buffer (red). The BSA concentration in the sample cuvettes was 0.5 mg/mL and the dye concentration in both the sample and reference cuvettes was 20 μM
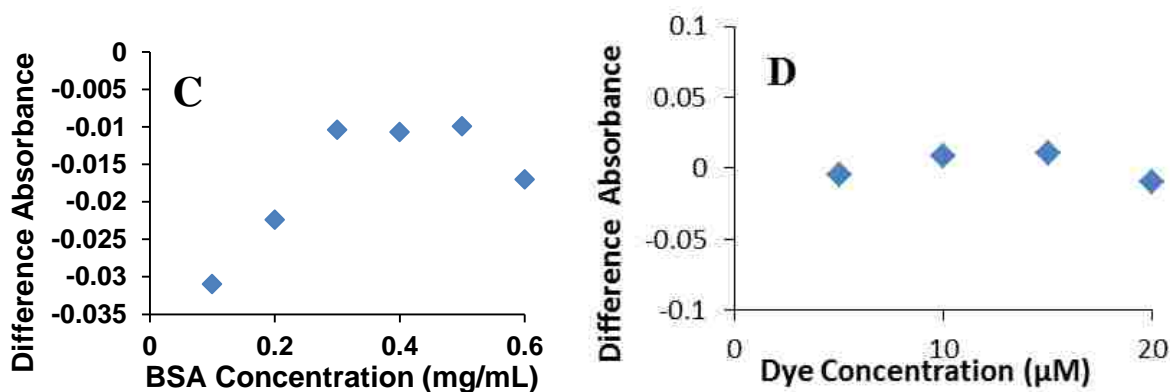


Figure2. 10Titration at λ=645nm of BSA with [PEG786][I] in PBS, pH=7.0. The dye concentration in the sample cuvettes was 20 μM (C); the BSA dye concentration in the sample cuvettes was 0.5 mg/mL (D)

## 2.3.4 In vitro Cytotoxicity Assay of PEG786 GUMBOS

Cellular toxicity of fluorescent NIR nanoparticles is a prime limitation which restricts application to living cell imaging.[38] Quantum dots are photostable fluorescent NIR nanoparticles with high luminescent efficiency; however, these nanoparticles are not always suitable for application in humans due to cytotoxic effects.[39, 40, 41] Indocyanine green (ICG),

in contrast, has been approved by the FDA for human use because of its low toxicity regardless of its poor photostablity and low quantum yield in aqueous media. However, research has demonstrated increased toxicity with an increase in ICG concentration, which limits the application of ICG at higher concentrations.[42]

In vitro cytotoxicity tests using our data suggest that the cytotoxicity of PEG786 GUMBOS is similar to [IR786][I] at low concentration but significantly different from [IR786][I] at high concentration (Figure 2.11). When the concentration is smaller than 15 μM, both PEGylated and un-PEGylated dye show low toxicity to cells, and there is no significant difference between [IR786][I] and PEG786 GUMBOS. Further examination of the results of the modified and unmodified dyes suggests that PEGylation significantly reduces the cytotoxicity of [IR786][I] at high concentrations. For example, the average cell viabilities in wells containing [PEG786][I], [PEG786][NTf2] and [PEG786][AOT] are 40.7%, 51.3% and 55.7% at concentration of 30 μM, while the average cell viability in wells containing [IR786][I] is 8.4% at the same concentration. This phenomenon can be ascribed to the formation of PEG786 nano- and meso-scale GUMBOS comprised of molecular self-assemblies with the hydrophobic dye skeleton facing the core of the assembly and the hydrophilic PEG chain facing the surface at high concentrations. Thus, PEG chains appear to protect the dye from direct contact with the cells, thereby decreasing its toxicity. This result suggests that PEG786 GUMBOS are suitable to be employed for cellular imaging at high concentrations.
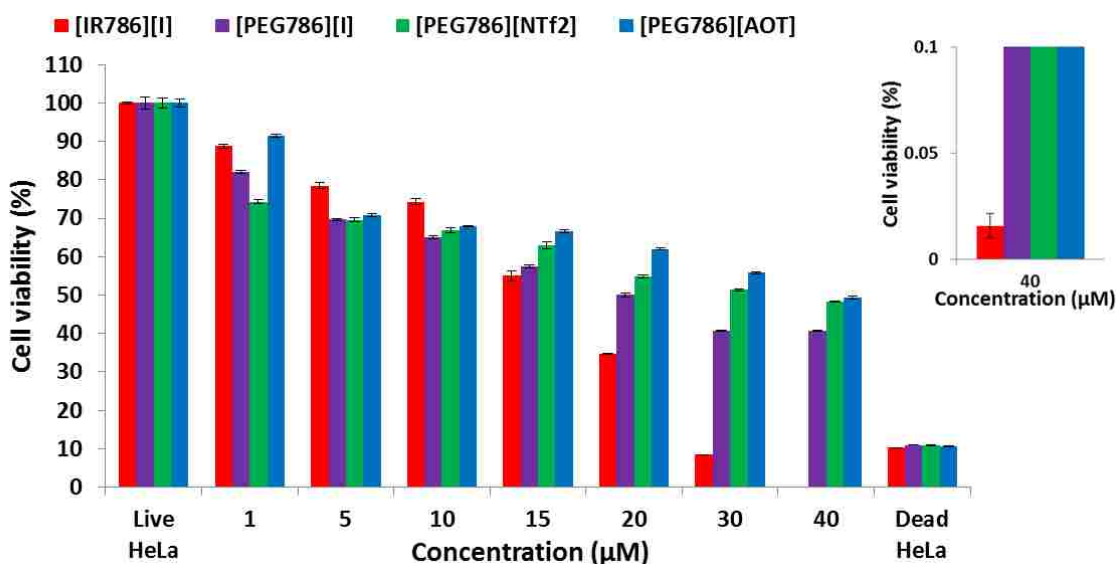
Figure2. 11 *In vitro* cytotoxicity of PEG786 GUMBOS and IR786 on Hela cells as measured by the MTT assay. Cell viability is expressed as mean $\pm$ S.D. (n = 3).

## 2.4 Conclusions

We have successfully synthesized PEG modified IR786 GUMBOS by simple variations of the associated counter anions. After modification, the new dyes showed very different properties as compared to the unmodified dye, which appear to be a result of formation of self-assemblies in water. A large Stokes shift of the PEG786 GUMBOS is attributed to intramolecular charge transfer (ICT) between the pyramidal and planar conformations in the excited states. PEG786 nano- and meso-scale GUMBOS also exhibit a reduced binding constant with BSA and reduced cytotoxicity at higher concentration. This is likely due to protection from PEG chains located on the surface of the nano- and meso-scale GUMBOS.

In addition to the above properties, photostability of PEG786 nano- and meso-scale GUMBOS varies with changes in anion. AOT and NTf$_2$ are shown to improve the photostablity of PEG786 nano- and meso-scale GUMBOS. We have also demonstrated that improved photostablity of [PEG786][NTf$_2$] nano- and mesoscale GUMBOS is a result of irradiation induced changes in dye molecule stacking, which lead to J-aggregation. Most importantly, the observation that PEGylation of IR786 followed by anion exchange with

suitable anions leads to enhanced fluorescence upon irradiation and reduced cytotoxicity at higher concentrations may provide many potential applications for biomedical imaging using NIR fluorescence.

## 2.5 References

1.      Erogbogbo, F.; Yong, K. T.; Roy, I.; Hu, R.; Law, W. C.; Zhao, W. W.; Ding, H.; Wu, F.; Kumar, R.; Swihart, M. T.; Prasad, P. N. In Vivo Targeted Cancer Imaging, Sentinel Lymph Node Mapping and Multi-Channel Imaging with Biocompatible Silicon Nanocrystals. *ACS Nano* **2010,** *5* (1), 413-423.

2.      Foy, S. P.; Manthe, R. L.; Foy, S. T.; Dimitrijevic, S.; Krishnamurthy, N.; Labhasetwar, V. Optical Imaging and Magnetic Field Targeting of Magnetic Nanoparticles in Tumors. *ACS Nano* **2010,** *4* (9), 5217-5224.

3.      Bringley, J. F.; Penner, T. L.; Wang, R. Z.; Harder, J. F.; Harrison, W. J.; Buonemani, L. Silica nanoparticles encapsulating near-infrared emissive cyanine dyes. *J. Colloid Interface Sci.* **2008,** *320* (1), 132-139.

4.      Morgan, T. T.; Muddana, H. S.; Altinoglu, E. I.; Rouse, S. M.; Tabakovic, A.; Tabouillot, T.; Russin, T. J.; Shanmugavelandy, S. S.; Butler, P. J.; Eklund, P. C.; Yun, J. K.; Kester, M.; Adair, J. H. Encapsulation of Organic Molecules in Calcium Phosphate Nanocomposite Particles for Intracellular Imaging and Drug Delivery. *Nano Lett.* **2008,** *8* (12), 4108-4115.

5.      Liong, M.; Lu, J.; Kovochich, M.; Xia, T.; Ruehm, S. G.; Nel, A. E.; Tamanoi, F.; Zink, J. I. Multifunctional inorganic nanoparticles for imaging, targeting, and drug delivery. *ACS Nano* **2008,** *2* (5), 889-896.

6.      Ow, H.; Larson, D. R.; Srivastava, M.; Baird, B. A.; Webb, W. W.; Wiesner, U. Bright and stable core-shell fluorescent silica nanoparticles. *Nano Lett.* **2005,** *5* (1), 113-117.

7.      Fuller, J. E.; Zugates, G. T.; Ferreira, L. S.; Ow, H. S.; Nguyen, N. N.; Wiesner, U. B.; Langer, R. S. Intracellular delivery of core-shell fluorescent silica nanoparticles. *Biomaterials* **2008,** *29* (10), 1526-1532.

8.      Weissleder, R. A clearer vision for in vivo imaging. *Nature Biotechnology* **2001,** *19* (4), 316-317.

9.      Altinoglu, E. I.; Russin, T. J.; Kaiser, J. M.; Barth, B. M.; Eklund, P. C.; Kester, M.; Adair, J. H. Near-Infrared Emitting Fluorophore-Doped Calcium Phosphate Nanoparticles for In Vivo Imaging of Human Breast Cancer. *ACS Nano* **2008,** *2* (10), 2075-2084.

10.     Michalet, X.; Pinaud, F. F.; Bentolila, L. A.; Tsay, J. M.; Doose, S.; Li, J. J.; Sundaresan, G.; Wu, A. M.; Gambhir, S. S.; Weiss, S. Quantum dots for live cells, in vivo imaging, and diagnostics. *Science* **2005,** *307* (5709), 538-544.

11.     Liu, W.; Howarth, M.; Greytak, A. B.; Zheng, Y.; Nocera, D. G.; Ting, A. Y.; Bawendi, M. G. Compact biocompatible quantum dots functionalized for cellular imaging. *Journal of the American Chemical Society* **2008,** *130* (4), 1274-1284.

12.     Venisnik, K. M.; Olafsen, T.; Loening, A. M.; Iyer, M.; Gambhir, S. S.; Wu, A. M. Bifunctional antibody-Renilla luciferase fusion protein for in vivo optical detection of tumors. *Protein Engineering Design & Selection* **2006,** *19* (10), 453-460.

13.     Maxwell, D.; Chang, Q.; Zhang, X.; Barnett, E. M.; Piwnica-Worms, D. An Improved Cell-Penetrating, Caspase-Activatable, Near-Infrared Fluorescent Peptide for Apoptosis Imaging. *Bioconjugate Chemistry* **2009,** *20* (4), 702-709.

14.     Murphy, C. J.; Gole, A. M.; Hunyadi, S. E.; Stone, J. W.; Sisco, P. N.; Alkilany, A.; Kinard, B. E.; Hankins, P. Chemical sensing and imaging with metallic nanorods. *Chem. Commun.* **2008,** (5), 544-557.

15.     Weissleder, R.; Tung, C. H.; Mahmood, U.; Bogdanov, A. In vivo imaging of tumors with protease-activated near-infrared fluorescent probes. *Nature Biotechnology* **1999,** *17* (4), 375-378.

16.     Cheng, Z.; Levi, J.; Xiong, Z. M.; Gheysens, O.; Keren, S.; Chen, X. Y.; Gambhir, S. S. Near-infrared fluorescent deoxyglucose analogue for tumor optical imaging in cell culture and living mice. *Bioconjugate Chemistry* **2006,** *17* (3), 662-669.

17.     Becker, A.; Hessenius, C.; Licha, K.; Ebert, B.; Sukowski, U.; Semmler, W.; Wiedenmann, B.; Grotzinger, C. Receptor-targeted optical imaging of tumors with near-infrared fluorescent ligands. *Nature Biotechnology* **2001,** *19* (4), 327-331.

18.     Klohs, J.; Wunder, A.; Licha, K. Near-infrared fluorescent probes for imaging vascular pathophysiology. *Basic Res. Cardiol.* **2008,** *103* (2), 144-151.

19.    Bwambok, D. K.; El-Zahab, B.; Challa, S. K.; Li, M.; Chandler, L.; Baker, G. A.; Warner, I. M. Near-Infrared Fluorescent NanoGUMBOS for Biomedical Imaging. *ACS Nano* **2009,** *3* (12), 3854-3860.


20.    Das, S.; Bwambok, D.; Ei-Zahab, B.; Monk, J.; de Rooy, S. L.; Challa, S.; Li, M.; Hung, F. R.; Baker, G. A.; Warner, I. M. Nontemplated Approach to Tuning the Spectral Properties of Cyanine-Based Fluorescent NanoGUMBOS. *Langmuir* **2010,** *26* (15), 12867-12876.


21.    Patonay, G.; Salon, J.; Sowell, J.; Strekowski, L. Noncovalent labeling of biomolecules with red and near-infrared dyes. *Molecules* **2004,** *9* (3), 40-49.


22.    Masotti, A.; Vicennati, P.; Boschi, F.; Calderan, L.; Sbarbati, A.; Ortaggi, G. A novel near-infrared indocyanine dye - Polyethylenimine conjugate allows DNA delivery imaging in vivo. *Bioconjugate Chemistry* **2008,** *19* (5), 983-987.


23.    Lee, Y. E. K.; Smith, R.; Kopelman, R. Nanoparticle PEBBLE Sensors in Live Cells and In Vivo. *Annual Review of Analytical Chemistry* **2009,** *2*, 57-76.


24.    Zhang, Z. R.; Achilefu, S. Synthesis and evaluation of polyhydroxylated near-infrared carbocyanine molecular probes. *Organic Letters* **2004,** *6* (12), 2067-2070.


25.    Lee, H.; Mason, J. C.; Achilefu, S. Heptamethine cyanine dyes with a robust C-C bond at the central position of the chromophore. *Journal of Organic Chemistry* **2006,** *71* (20), 7862-7865.


26.    Peng, X. J.; Song, F. L.; Lu, E.; Wang, Y. N.; Zhou, W.; Fan, J. L.; Gao, Y. L. Heptamethine cyanine dyes with a large stokes shift and strong fluorescence: A paradigm for excited-state intramolecular charge transfer. *Journal of the American Chemical Society* **2005,** *127* (12), 4170-4171.


27.    Lu, W.; Wan, J.; Zhang, Q.; She, Z. J.; Jiang, X. G. Aclarubicin-loaded cationic albumin-conjugated pegylated nanoparticle for glioma chemotherapy in rats. *International Journal of Cancer* **2007,** *120* (2), 420-431.


28.    Levy, D. E.; Ding, Z. L.; Hu, C. W.; Zalipsky, S. PEGylated iminodiacetic acid zinc complex stabilizes cationic RNA-bearing nanoparticles. *Bioorganic & Medicinal Chemistry Letters 20* (18), 5499-5501.


29.    Lipka, J.; Semmler-Behnke, M.; Sperling, R. A.; Wenk, A.; Takenaka, S.; Schleh, C.; Kissel, T.; Parak, W. J.; Kreyline, W. G. Biodistribution of PEG-modified gold nanoparticles

following intratracheal instillation and intravenous injection. *Biomaterials* *31* (25), 6574-6581.

30.    Liu, J. Q.; Setijadi, E.; Liu, Y. K.; Whittaker, M. R.; Boyer, C.; Davis, T. P. PEGylated Gold Nanoparticles Functionalized with beta-Cyclodextrin Inclusion Complexes: Towards Metal Nanoparticle-Polymer-Carbohydrate Cluster Biohybrid Materials. *Australian Journal of Chemistry* *63* (8), 1245-1250.

31.    Bazile, D.; Prud'homme, C.; Bassoullet, M. T.; Marlard, M.; Spenlehauer, G.; Veillard, M. Stealth Me.PEG-PLA nanoparticles avoid uptake by the mononuclear phagocytes system. *Journal of pharmaceutical sciences* **1995,** *84* (4), 493-8.

32.    Takahashi, T.; Yamada, Y.; Kataoka, K.; Nagasaki, Y. Preparation of a novel PEG-clay hybrid as a DDS material: Dispersion stability and sustained release profiles. *Journal of Controlled Release* **2005,** *107* (3), 408-416.

33.    Chen, H.; Hu, X. Y.; Zhang, Y. X.; Li, D.; Wu, Z. K.; Zhang, T. Effect of chain density and conformation on protein adsorption at PEG-grafted polyurethane surfaces. *Colloids and Surfaces B-Biointerfaces* **2008,** *61* (2), 237-243.

34.    Lu, W.; Tan, Y. Z.; Hu, K. L.; Jiang, X. G. Cationic albumin conjugated pegylated nanoparticle with its transcytosis ability and little toxicity against blood-brain barrier. *International Journal of Pharmaceutics* **2005,** *295* (1-2), 247-260.

35.    Sereikaite, J.; Bumeliene, Z.; Bumelis, V. A. Bovine serum albumin-dye binding. *Acta Chromatographica* **2005,** *15*, 298-307.

36.    Mishra, A.; Behera, R. K.; Behera, P. K.; Mishra, B. K.; Behera, G. B. Cyanines during the 1990s: A review. *Chemical Reviews* **2000,** *100* (6), 1973-2011.

37.    Tachibana, H.; Sato, F.; Terrettaz, S.; Azumi, R.; Nakamura, T.; Sakai, H.; Abe, M.; Matsumoto, M. Light-induced J-aggregation in mixed Langmuir-Blodgett films of selenium-containing cyanine and azobenzene. *Thin Solid Films* **1998,** *327*, 813-815.

38.    He, X. X.; Wang, K. M.; Cheng, Z. In vivo near-infrared fluorescence imaging of cancer with nanoparticle-based probes. *Wiley Interdisciplinary Reviews-Nanomedicine and Nanobiotechnology* **2010,** *2* (4), 349-366.

39.    Hardman, R. A toxicologic review of quantum dots: Toxicity depends on physicochemical and environmental factors. *Environmental Health Perspectives* **2006,** *114* (2), 165-172.

40.     Lin, P.; Chen, J. W.; Chang, L. W.; Wu, J. P.; Redding, L.; Chang, H.; Yeh, T. K.; Yang, C. S.; Tsai, M. H.; Wang, H. J.; Kuo, Y. C.; Yang, R. S. H. Computational and ultrastructural toxicology of a nanoparticle, Quantum Dot 705, in mice. *Environmental Science & Technology* **2008,** *42* (16), 6264-6270.


41.     Geys, J.; Nemmar, A.; Verbeken, E.; Smolders, E.; Ratoi, M.; Hoylaerts, M. F.; Nemery, B.; Hoet, P. H. M. Acute Toxicity and Prothrombotic Effects of Quantum Dots: Impact of Surface Charge. *Environmental Health Perspectives* **2008,** *116* (12), 1607-1613.


42.     Ho, J. D.; Tsai, R. J. F.; Chen, S. N.; Chen, H. C. Cytotoxicity of indocyanine green on retinal pigment epithelium - Implications for macular hole surgery. *Archives of Ophthalmology* **2003,** *121* (10), 1423-1429.

# CHAPTER 3 DYSPROSIUM BASED MULTIFUNCTIONAL IONIC LIQUID CRYSTALS WITH ENHANCED LUMINESCENCE INTENSITY

## 3.1 Introduction

Ionic liquid crystals (ILCs) are a class of liquid-crystalline compounds that contain anions and cations. ILCs are unique liquid crystals because they combine the properties of liquid crystals and ionic liquids in a single compound.[1] ILCs have the properties of ionic liquids, such as low volatility, non-flammability, high ionic conductivity, and large electrochemical windows, which are different from those of organic liquid crystals. ILCs also possess properties of liquid crystals, such as ordered molecular arrangement making ILCs highly structured solvents. Due to their unique properties, ILCs are often used as electrolytes for fuel cells [2, 3] and solar cells,[4] templating agents for synthesis of inorganic nanostructures,[5] and as organized reaction media.[1]

In the last few decades, ILCs that incorporate functional groups in either the anion or the cation have received intense attention.[6, 7, 8, 9, 10] Chirality is an important factor in functional ILC design. Much efforts have been concentrated on developing asymmetric synthesis and catalysis using chiral ionic liquids as solvent, and preliminary results have shown that chiral ionic liquids are promising reaction media for chiral discrimination. [11, 12, 13, 14, 15, 16, 17, 18] Furthermore, if chiral ionic liquids show thermotropic  mesophases, they have the potential to offer increased selectivity by ordering of reactants. In addition, highly structured mesophases could be used for synthesis of mesoporous materials and ordered thin films.[19]

Metal-containing ILCs have been widely explored as multifunctional materials due to the combination of the mesomorphic behavior and unique properties of metal ions such as redox-activity, magnetism, and luminescence.[6] The combination of luminescence of metal ions and anisotropy of ILCs can produce polarized light. By taking advantage of the high magnetic anisotropy of the lanthanide ions in ILCs, alignment of the mesophase in an external magnetic

69

field can be achieved. Such compounds have the potential for use in electric and magnetic switchable devices.[6]

To the best of our knowledge, multifunctional ILCs that possess chirality, luminescence, paramagnetism as well as mesophase have not yet been reported. (1R, 2S) (-)-Methylephedrine ((-)MeEph) is a natural chiral resource which is used as a starting material for synthesis of ILCs. In this study, (-)MeEph based multi-functional ionic liquid crystals (MFILCs) which consist of chiral cations and lanthanide metal-containing anions were synthesized and characterized. Their thermal and photophysical properties were also investigated in regards to their potential applications. The properties investigated in this study suggest possible usage of these materials as organized reaction media and temperature sensors.

### 3. 2 Experimental Methods

### 3.2.1 Materials

(1R, 2S) (-)-N-Methylephedrine, (1S, 2R) (+)-N-Methylephedrine, 1-bromotetradecane, 1-bromohexadecane, 1-bromooctadecane, potassium thiocyanate, dysprosium(III) oxide, and perchloric acid (70%) were obtained from Sigma-Aldrich (Milwaukee, Wisconsin, USA) and used without further purification. Ethanol, methanol, acetonitrile, chloroform, and carbon tetrachloride were of anhydrous grade (Sigma-Aldrich, Milwaukee, WI), and all other solvents such as acetone, hexane, and water were of HPLC grade (J. T. Baker, Phillipsburg, NJ).

### 3.2.2 Synthesis of Multifunctional Ionic Liquids

A facile three-step synthesis procedure was used to prepare the (-)-N-Methylephedrine-lanthanide based MFILCs. In the first step, (1R, 2S) (-)-N-Methylephedrine ((-)MeEph) (1500 mg, 8.37 mmol) was dissolved in dry ethanol. A 1.1 molar equivalent of 1-bromotetradecane or 1-bromohexadecane or 1-bromooctadecane was dissolved separately in dry ethanol. The two

solutions were mixed and the reaction mixture was refluxed for 2 days at 90 °C under argon atmosphere. After cooling to room temperature, most of the solvent was removed by use of a rotary evaporator. Upon addition of the concentrated ethanol solution to cold diethyl ether, the product $[(-)MeEphC_nH_{2n+}1][Br]$ (n=14, 16, 18) precipitated as a white powder. The product was filtered and washed two times using diethyl ether, and then dried under vacuum.

In the second step, three methylephedrin-dysprosium compounds were synthesized according to the procedure previously described.[20] $[(-)MeEphC_nH_{2n+1}][Br]$ (n=14, 16, 18) and 2 molar equivalents of potassium thiocyanate (KSCN) was dissolved in dry acetonitrile, separately. The two solutions were then mixed and the reaction mixture stirred for 2 days. KBr, the reaction by-product, formed as a white precipitate and was removed by filtration. Acetonitrile was removed by use of a rotary evaporator. To further purify the compounds produced, the resulting solid was re-dissolved in 30 mL of cold dichloromethane (DCM), and the solution was kept in a refrigerator for 24 hours in order to precipitate the excess KSCN. After filtration of the excess KSCN, the solvent was evaporated and the product, $[(-)MeEphC_nH_{2n+1}]$ [SCN] (n=14, 16, 18), was dried under vacuum for 48 hours.

In the third step, $Dy(ClO_4)_3 \bullet 6H_2O$ was prepared by dissolving $Dy_2O_3$ in a 70% $HClO_4$ aqueous solution, with subsequent removal of water by lyophilization. A mixture of $[(-)MeEphC_nH_{2n+1}]$ [SCN] (n=14, 16, 18) (5 equiv.), KSCN (3 equiv.), and $Dy(ClO_4)_3.6H_2O$ (1 equiv.) was stirred in anhydrous ethanol at room temperature for 24 hours. The by-product $(KClO_4)$ was removed by filtration and the final products, $[(-)MeEphC_nH_{2n+1}]_5[Dy(SCN)_8]$ (n=14, 16, 18), were purified and collected employing the method described above.

### 3.2.3 Instruments and Methods

$^1$H NMR (400 MHz) and $^{13}$C NMR (100 MHz) spectra were acquired by use of a Bruker Avance 400 NMR spectrometer. The $^1$H and $^{13}$C chemical shifts are given in parts per million ($\delta$) with TMS as an internal standard. Mass spectra were collected on Agilent 6210 Electrospray Time-of-flight Mass Spectrometer by use of both positive and negative ion mode.

Luminescence spectra were recorded at temperatures ranging from 25 - 100 ℃ using a Spex Fluorolog-3 spectrofluorometer (model FL3-22TAU3; Jobin Yvon, Edison, NJ, USA) equipped with a 450-W xenon lamp and R928P photomultiplier tube (PMT) emission detector. CD measurements were obtained by analyzing 1 mM methanolic solutions at room temperature in 4-mm quartz cuvettes on a Jasco-815 CD spectrometer.

Magnetic properties were measured using approximately 80 to100 mg of sample in a Quantum Design Superconducting Quantum Interference Device (SQUID) magnetometer (San Diego, CA, USA) at temperatures between 2 and 300 K and fields between −70 000 and 70 000 Oe.

Thermal properties of MFILCs were investigated with a DSC Q 100 differential calorimeter (TA Instruments, USA) by cooling 5–10 mg of MFILCs to -20 ℃ and subsequently heating it at a rate of 5℃ per min to 150℃. Polarized optical microscopy (POM) was performed using an Olympus BH polarizing optical microscope with a hot stage and MD 1900 camera. Samples for POM were prepared by re-dissolving the MFILCs in DCM and ethanol, and coating the solution on the surface of glass slides using spin coating. The images were taken at temperatures ranging from room temperature to 100℃. The samples were incubated for 30 minutes to allow the mesophase to equilibrate before taking images.

## 3.3 Results and Discussion

### 3. 3.1 Synthesis of Multi-functional Ionic Liquid Crystals

(1R, 2S) (-)-Methylephedrine ((-)MeEph) were alkylated with n-alkylbromides containing 14, 16, and 18 carbons to afford chiral cations. The multi-functional ionic liquid crystals (MFILCs) were obtained by two anion exchange reactions with the (-)MeEph based salts. In the first anion exchange, SCN⁻ was used to replace Br⁻. A second anion exchange resulted in a dysprosium-thiocyanate complex anion. The synthesis of the MFILCs is outlined in Scheme 3.1.
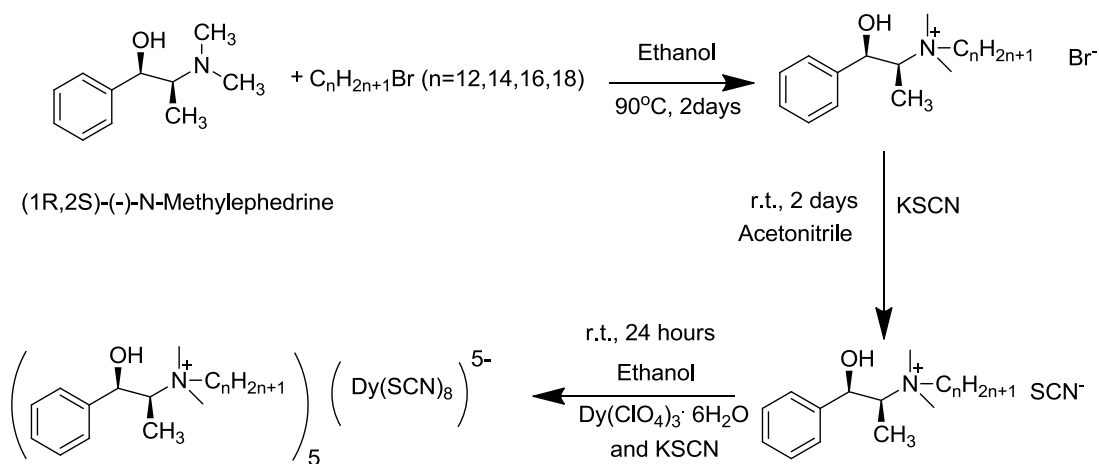


Scheme3. 1 Synthesis of multi-functional ionic liquid crystal

[(-)MeEph $C_{14}H_{29}$]$_5$ [Dy(SCN)$_8$]: pale brown viscous semi-solid. Yield, 79% (400 MHz, DMSO-d6), δ (ppm): 0.94(m, 6H), 1.36 (m, 24H), 2.17 (m, 6H), 2.98(m, 1H), 6.05(m, 1H), 7.28(t,5H), Calculated: $m/z = 376.64$, Found: $m/z = 376.36$

[(-)MeEph $C_{16}H_{33}$]$_5$ [Dy(SCN)$_8$]: pale brown solid . Yield, 77% (400 MHz, DMSO-d6), δ (ppm): 0.93(m, 6H), 1.34 (m, 28H), 2.16 (m, 6H), 2.97(m, 1H), 3.28(m,1H), 6.05(m, 1H), 7.28(t,5H), Calculated: $m/z = 404.69$, Found: $m/z = 404.39$

[(-)MeEph C$_{18}$H$_{37}$]$_5$[Dy(SCN)$_8$]: pale brown solid . Yield, 82% (400 MHz, DMSO-d6), δ (ppm): 0.85(t, 3H), 1.10(d, 3H) 1.22(m, 32H), 2.07 (m, 1H), 3.18(m, 6H), 3.30(t, 1H), 5.43(d, 1H), 6.00(d, 1H), 7.28(t, 5H) , Calculated: *m/z* = 432.74, Found: *m/z* = 432.42

### 3.3.2 Chiroptical Activity of Multi-functional Ionic Liquid Crystals

Ephedrine has two chiral centers which give rise to four stereoisomers. The enantiomers with opposite stereochemistry around the chiral centers (1R, 2S-(-) and 1S, 2R-(+)) are named ephedrine, while the enantiomers with the same stereochemistry around the chiral carbons (1R, 2R and 1S, 2S) are designated pseudoephedrine. In this study, only (1R, 2S) (-)-ephedrine was used for further structural modification to produce MILCs. To investigate the chiroptical activities of the MFILCs, circular dichroism (CD) studies were performed with [(-)MeEph C$_{16}$H$_{33}$]$_5$ [Dy(SCN)$_8$]  and [(+)MeEph C$_{16}$H$_{33}$]$_5$ [Dy(SCN)$_8$] in ethanol. [(+)MeEph C$_{16}$H$_{33}$]$_5$ [Dy(SCN)$_8$] was synthesized using the same procedure as the preparation of [(-)MeEph C$_{16}$H$_{33}$]$_5$ [Dy(SCN)$_8$] using (1S, 2R)-(+)Methylephedrine as a starting material. The comparison of CD spectra of [(-)MeEph C$_{16}$H$_{33}$]$_5$ [Dy(SCN)$_8$] and [(+)MeEph C$_{16}$H$_{33}$]$_5$ [Dy(SCN)$_8$] is shown in Figure 3.1. Three bands of at 255 nm, 261 nm and 267 nm were observed for both compounds, while [(-)MeEph C$_{16}$H$_{33}$]$_5$ [Dy(SCN)$_8$]  shows positive signal and [(+)MeEph C$_{16}$H$_{33}$]$_5$ [Dy(SCN)$_8$] shows negative signal. The two isomers exhibit a precise mirror image relationship. The results demonstrate that MFILCs retain chiroptical properties after structural modification.
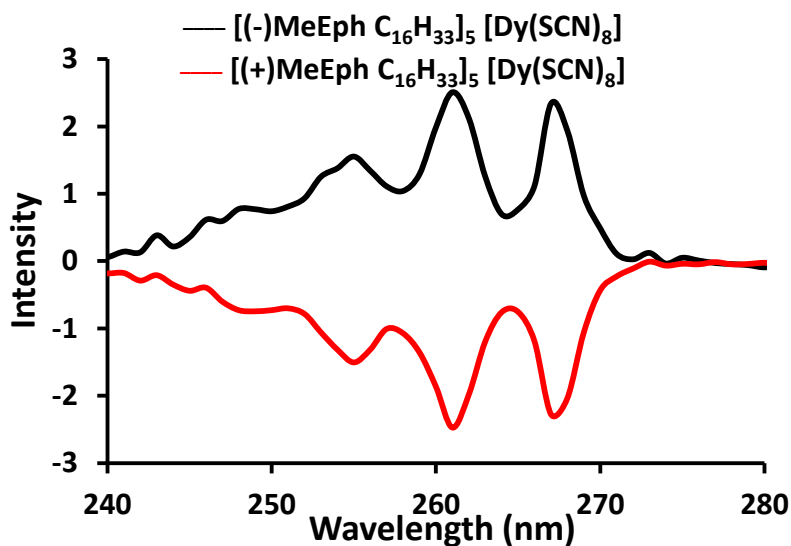
Figure3. 1 Circular dichroism spectra of [(-)MeEph $C_{16}H_{33}$]$_5$ [Dy(SCN)$_8$] (black) and [(+)MeEph $C_{16}H_{33}$]$_5$ [Dy(SCN)$_8$] (red) in ethanol at concentration of 1mM

### 3.3.3 Luminescence Spectroscopy of Multi-functional Ionic Liquid Crystals

The emission spectra of MFILCs were recorded at excitation wavelength of 366 nm in both solid state and in acetonitrile. The solid samples were prepared by spin coating of MFILCs in ethanol onto glass slides and then allowing them to dry under vacuum, overnight. Trivalent dysprosium, $Dy^{3+}$ with a $4f^9$ electron configuration, has been found to be luminescent due to the transitions from $^4F_{9/2}$ to $^6H_{15/2}$ in blue light and from $^4F_{9/2}$ to $^6H_{13/2}$ in the yellow-orange region.[21] As shown in Figure 3.2, the two characteristic emissions of the three compounds were observed both in solution and in solid state. The intensity and relative intensities of these two emission peaks, however, are quite different in solution and in solid state. This indicates that the transitions are hypersensitive to the environment. The emission intensity orders of MFILCs acetonitrile solutions were [(-)MeEph $C_{14}H_{29}$]$_5$ [Dy(SCN)$_8$] > [(-)MeEph $C_{16}H_{33}$]$_5$ [Dy(SCN)$_8$] > [(-)MeEph $C_{18}H_{37}$]$_5$ [Dy(SCN)$_8$], whereas the emission intensity of MFILCs films showed a

reverse order. The transition $^4F_{9/2}$ to $^6H_{13/2}$ at 573 nm is the most intense peak for all compounds in acetonitrile, agreeing with previous studies.[20] It is well known that the 4f-4f transitions are parity forbidden. The excitation of Dy (III) at 366 nm is due to the existence of (-)MeEph based cation which serves as an antenna to allow energy transfer to $Dy^{3+}$.[20] The forbidden 4f-4f transitions also result in long-lived excited states and subsequently reduce photobleaching.
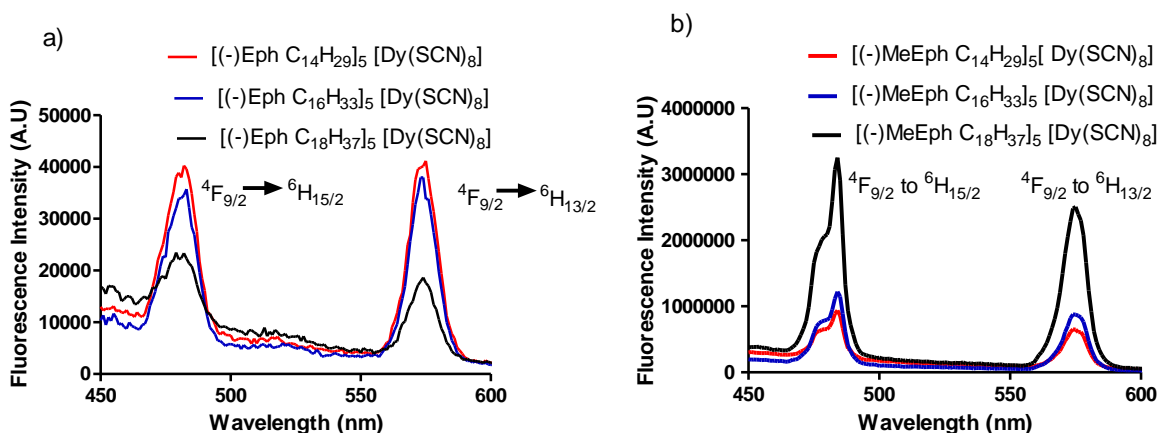


a)
— $[(-)Eph\ C_{14}H_{29}]_5\ [Dy(SCN)_8]$
— $[(-)Eph\ C_{16}H_{33}]_5\ [Dy(SCN)_8]$
— $[(-)Eph\ C_{18}H_{37}]_5\ [Dy(SCN)_8]$

b)
— $[(-)MeEph\ C_{14}H_{29}]_5[\ Dy(SCN)_8]$
— $[(-)MeEph\ C_{16}H_{33}]_5\ [Dy(SCN)_8]$
— $[(-)MeEph\ C_{18}H_{37}]_5\ [Dy(SCN)_8]$

Figure3. 2 Emission spectra with transition assignments of $[(-)MeEph\ C_{14}H_{29}]_5\ [Dy(SCN)_8]$ (red), $[(-)MeEph\ C_{16}H_{33}]_5\ [Dy(SCN)_8]$(blue) and $[(-)MeEph\ C_{18}H_{37}]_5\ [Dy(SCN)_8]$(black) at acetonitrile solution a) and at solid states b)under excitation at $\lambda ex=366$ nm

### 3.3.4 Paramagnetic Properties of Multi-functional Ionic Liquid Crystals

In addition to its luminescence arising from $4f^9$ electron configuration, the $Dy^{3+}$ ion is also magnetically active. As a result, the MFILCs exhibited paramagnetic behavior at room temperature. Their magnetic susceptibilities were measured by use of a superconducting quantum interference device (SQUID) magnetometer. The magnetic properties of $[(-)MeEph\ C_{16}H_{33}]_5\ [Dy(SCN)_8]$ is summarized in Figure 3.3. The decrease in static molar magnetic susceptibility with increasing temperature in the plot of $\chi_{mol}$ against temperature (K) indicates that $[(-)MeEph\ C_{16}H_{33}]_5\ [Dy(SCN)_8]$ is paramagnetic (Figure 3.3 a). The respective molar magnetic susceptibilities of $[(-)MeEph\ C_{16}H_{33}]_5\ [Dy(SCN)_8]$ and $[(-)MeEph\ C_{18}H_{37}]_5$

[Dy(SCN)$_8$] at 300 K were obtained as $\chi_{mol}$ = 0.046 and 0.044 emu mol$^{-1}$, which fit well with the

expected value for Dy$^{3+}$. The effective magnetic moment ($\mu_{eff}$) for Dy$^{3+}$ has been calculated as

10.48 $\mu$B. The measured respective $\mu_{eff}$ values of [(-)MeEph C$_{16}$H$_{33}$]$_5$ [Dy(SCN)$_8$]  and [(-

)MeEph C$_{18}$H$_{37}$]$_5$ [Dy(SCN)$_8$] were 10.5 and 10.3 $\mu$B, respectively, which are very close to the

calculated values. Due to the large anisotropic magnetic moment of Dy$^{3+}$in ionic liquid crystals,

the MFILCs can be manipulated in an external magnetic field. Therefore, the MFILCs are

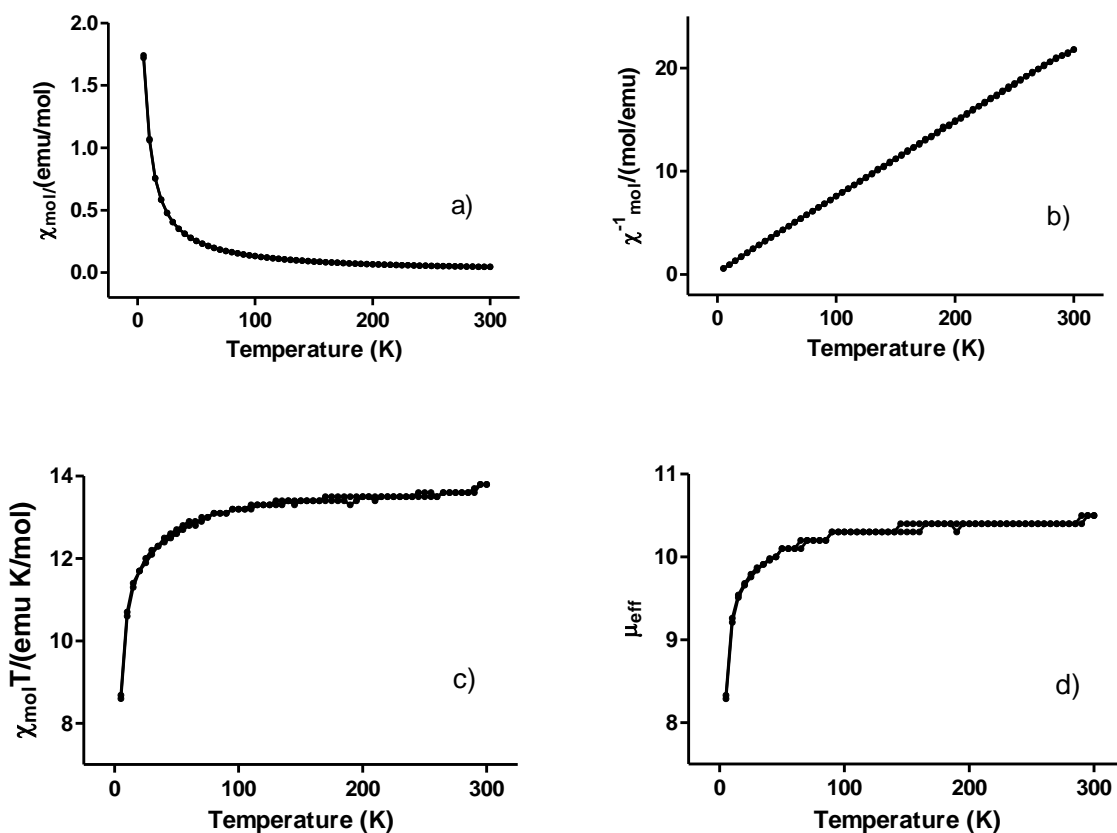expected to align in the direction of the applied external magnetic field.



Figure3. 3 Magnetic properties of [(-)MeEph C$_{16}$H$_{33}$]$_5$ [Dy(SCN)$_8$]. Temperature dependence of the static molar susceptibility (a) and reciprocal molar susceptibility (b) at a field of 10,000 Oe. Temperature dependence of the product of the temperature and the static molar susceptibility (c) and the effective magnetic moment (d) at a field of 10,000 Oe.

### 3.3.5 Thermal properties of Multi-functional Ionic Liquid Crystals

The thermal properties of all the compounds were examined using differential scanning calorimetry (DSC) and polarizing optical microscopy (POM). DCM and ethanol were independently used for re-dissolving MFILCs, and then the sample solutions were dried in a vacuum desiccator prior to analysis (for convenience, we called these samples DCM sample or ethanol sample). It was observed that the MFILCs show different thermal properties upon recrystallization from different solvents. The thermal properties of $[(-)MeEph\ C_{14}H_{29}]_5$ $[Dy(SCN)_8]$ will not be discussed since it did not exhibit a mesophase upon heating due to its short alkyl chain. DSC thermograms of $[(-)MeEph\ C_{18}H_{37}]_5$ $[Dy(SCN)_8]$ and $[(-)MeEph\ C_{16}H_{33}]_5$ $[Dy(SCN)_8]$ are shown in Figure 3.4 and Figure 3.5. Only the first heating traces are displayed since the phase transition could not be detected by DSC in the cooling trace and second scan. For the DCM samples of both $[(-)MeEph\ C_{18}H_{37}]_5$ $[Dy(SCN)_8]$ and $[(-)MeEph\ C_{16}H_{33}]_5$ $[Dy(SCN)_8]$, an additional peak was observed prior to the solid-to-mesophase transition peak. This additional peak may be due to the desolvation of trace DCM that remains in the compounds. The $[(-)MeEph\ C_{16}H_{33}]_5$ $[Dy(SCN)_8]$ DCM sample displayed a mesophase range from 41.9- 66.9 °C, while the ethanol sample displayed a mesophase range from 44.1- 74.9 °C. The $[(-)MeEph\ C_{18}H_{37}]_5$ $[Dy(SCN)_8]$ DCM sample showed a much lower crystalline solid to liquid crystalline transition temperature than that of ethanol sample. The liquid crystalline to isotropic liquid transition of DCM sample was observed at 85.6 °C, but the phase transition of the ethanol sample could not be detected by DSC.

POM investigation was carried out to examine the alteration of anisotropic behavior of the compounds upon heating of $[(-)MeEph\ C_{18}H_{37}]_5$ $[Dy(SCN)_8]$ and $[(-)MeEph\ C_{16}H_{33}]_5$ $[Dy(SCN)_8]$. The microscopy images of the textures are shown in figure 3.6. For both

compounds, the ethanol samples exhibited a nematic phase while DCM samples displayed a typical fan-shaped texture of SmA phase. The POM investigation of [(-)MeEph $C_{16}H_{33}$]$_5$ [Dy(SCN)$_8$] demonstrated that the optical data agree well with DSC data. In addition to confirming the DSC studies, POM examination also provided further information which could not be detected by DSC. The POM investigation of [(-)MeEph $C_{18}H_{37}$]$_5$ [Dy(SCN)$_8$] indicated that the liquid crystalline to isotropic liquid transition occurs at 98°C regardless of the treatment method. Furthermore, although no thermal events were observed during the cooling and second heating process by DSC, POM investigations observed mesophases during the second heating for MFILCs (Figure 3.6 c, f and g).
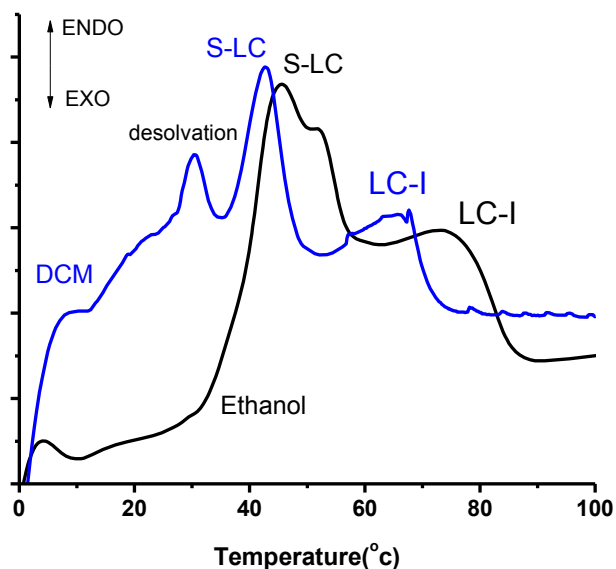


Figure 3.4 DSC traces observed on heating of [(-)Eph $C_{16}H_{33}$]$_5$ [Dy(SCN)$_8$] DCM sample (in blue) and ethanol sample (in black), (closed aluminum pan, heating rate 5 °C/min, *S-LC*: solid to liquid crystalline transition, *LC-I*: liquid crystalline to isotropic liquid transition)

Figure 3. 5 DSC traces observed on heating of [(-)Eph $C_{18}H_{37}$]$_5$ [Dy(SCN)$_8$]  DCM sample (in blue) and ethanol sample(in black), (closed aluminum pan, heating rate 5 ℃/min, *S-LC*: solid to liquid crystalline transition, *LC-I*: liquid crystalline to isotropic liquid transition)
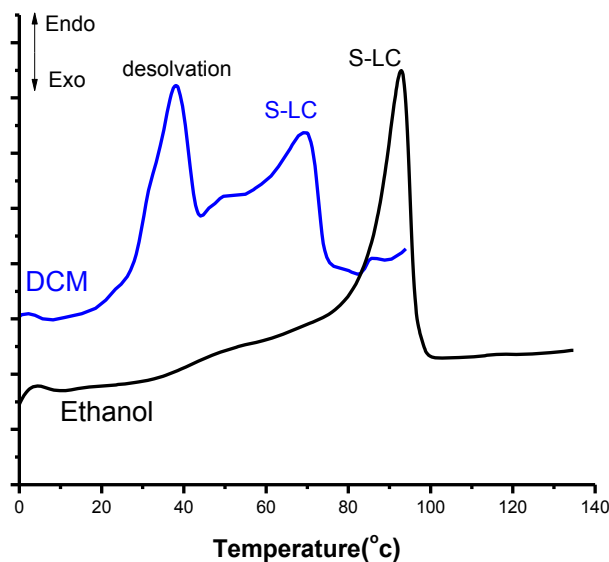
### 3.3.6 Phase Dependent Luminescence Intensity of Multi-functional Ionic Liquid Crystals

To investigate the influence of the phase transitions on luminescence, the emission spectra of transitions from $^4F_{9/2}$ to $^6H_{15/2}$ and from $^4F_{9/2}$ to $^6H_{13/2}$ were recorded over a temperature range from 20℃ to 100℃. Figure 3.7 shows the changes in $^4F_{9/2}$ to $^6H_{15/2}$ emission intensities of [(-)EphC$_{16}$H$_{33}$]$_5$ [Dy(SCN)$_8$] and [(-)EphC$_{18}$H$_{37}$]$_5$[Dy(SCN)$_8$] as a function of temperature.  Based on the DSC studies and optical data, the temperature-dependent luminescence intensity changes were divided into three regions: the solid crystalline state, the liquid crystalline state, and the isotropic liquid state. All samples exhibited enhanced luminescence intensity in liquid crystal state except for [(-)EphC$_{16}$H$_{33}$]$_5$ [Dy(SCN)$_8$] on second heating. It must be noted that [(-)EphC$_{16}$H$_{33}$]$_5$ [Dy(SCN)$_8$] and [(-)EphC$_{18}$H$_{37}$]$_5$[Dy(SCN)$_8$] DCM samples showed a sharp
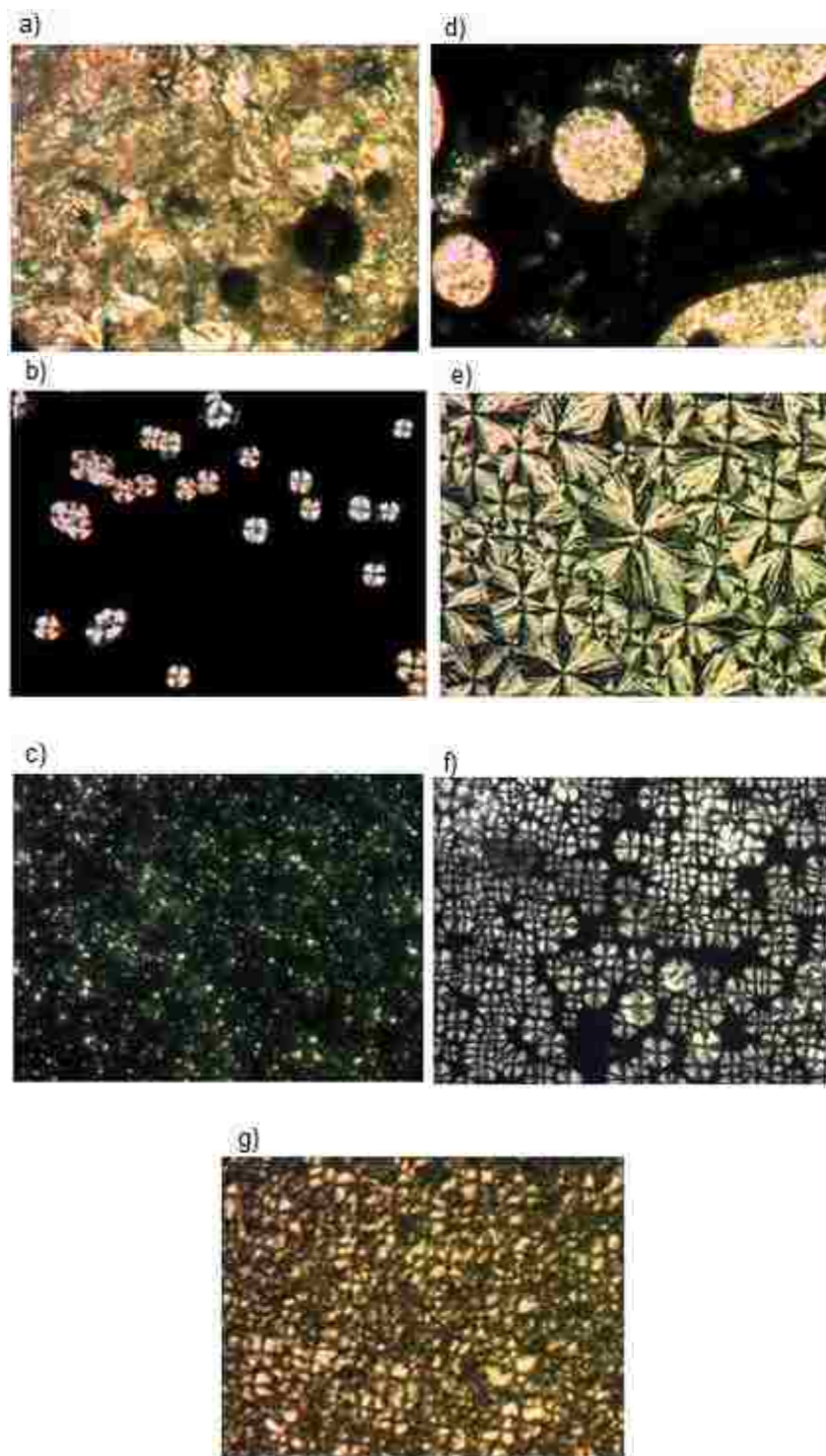
Figure3. 6 Micrographs of the textures observed by POM (200X magnification). Textures of [(-)EphC$_{16}$H$_{33}$]$_5$ [Dy(SCN)$_8$] ethanol sample at 70 ℃ (a) and DCM sample (right)at 60 ℃ (b), second heating at 75 ℃ (c);  [(-)EphC$_{18}$H$_{37}$]$_5$ [Dy(SCN)$_8$] ethanol  sample at 95 ℃ (d) and DCM sample (right) at 85 ℃ (e), second heating at 70 ℃ (f)and second heating at 90 ℃ (g).
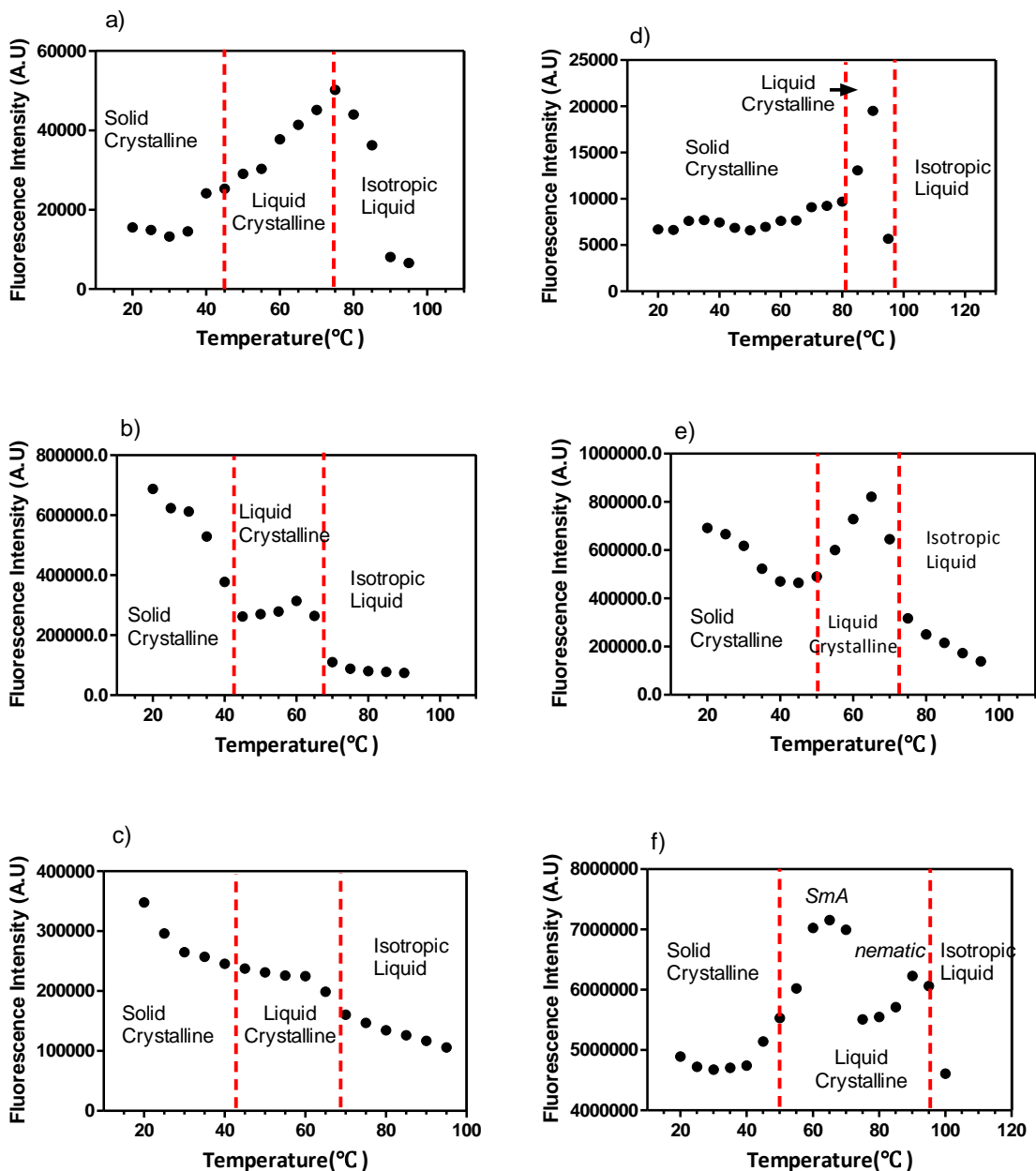
Figure3. 7 Temperature-dependent luminescence intensity from $^4F_{9/2}$ to $^6H_{15/2}$ transition (blue light emission, excitation at 366 nm) of [(-)EphC$_{16}$H$_{33}$]$_5$ [Dy(SCN)$_8$] ethanol sample (a); DCM sample (b); second heating (c); as well as of [(-)EphC$_{18}$H$_{37}$]$_5$[Dy(SCN)$_8$] ethanol sample (d); DCM sample (e) and second heating (f).

decrease in luminescence intensity in both the solid state with increasing temperature, due to the desolvation of trace DCM remaining in sample, as discussed before. In the liquid crystal state, the luminescence intensity displayed a linear increase with increasing temperature until a full liquid crystal state was achieved. Interestingly, $[(-)EphC_{18}H_{37}]_5[Dy(SCN)_8]$ exhibited two luminescence intensity increases at liquid crystal state during the second heating. This was because the sample first formed fan-shaped SmA phase and then formed nematic phase with increasing temperature. As the temperature increased, a dramatic decrease in luminescence intensity was observed at the liquid crystalline to isotropic liquid transition. Typically, the MFILCs in isotropic liquid state are non-fluorescent; this may be due to the hinderance of energy transfer due to the increased distance between the cations and the anions in liquid state. We believe that these MFILCs are potential candidates to be used in the construction of sensitive chemosensors or optoelectronic devices because of their specific linear response range with temperature and dramatically enhanced luminescence intensity at the liquid crystal state.

### 3.4 Conclusion

We have synthesized and characterized a group of novel MFILCs, which incorporated luminescence, chirality, paramagnetism, and mesophase in a single ion pair. The MFILCs retain the chirality of the starting material and may be used as reaction media for synthesis of chiroptically active compounds in combination with liquid crystalline and magnetic properties. The compounds show a structure and solvent dependent liquid crystalline mesophases below 100℃, and in turn show phase dependent luminescence intensity. A longer alkyl chain leads to an easier formation of the mesophase texture but reduces the mesophase window. Using DCM for recrystallization of the compounds results in SmA mesophase and the use of ethanol induces

nematic mesophases. Both compounds exhibit enhanced luminescence intensity at the liquid crystalline state and dramatically decreased luminescence in the isotropic liquid state. Based on their unique properties, these compounds have the potential to be used in optical devices.

## 3.5 References

1.      Binnemans, K. Ionic liquid crystals. *Chemical Reviews* **2005,** *105* (11), 4148-4204.


2.      Shin, J. H.; Henderson, W. A.; Passerini, S. PEO-based polymer electrolytes with ionic liquids and their use in lithium metal-polymer electrolyte batteries. *Journal of the Electrochemical Society* **2005,** *152* (5), A978-A983.


3.      Nakagawa, H.; Izuchi, S.; Kuwana, K.; Nukuda, T.; Aihara, Y. Liquid and polymer gel electrolytes for lithium batteries composed of room-temperature molten salt doped by lithium salt. *Journal of the Electrochemical Society* **2003,** *150* (6), A695-A700.


4.      Papageorgiou, N.; Athanassov, Y.; Armand, M.; Bonhote, P.; Pettersson, H.; Azam, A.; Gratzel, M. The performance and stability of ambient temperature molten salts for solar cell applications. *Journal of the Electrochemical Society* **1996,** *143* (10), 3099-3108.


5.      Taubert, A. CuCl nanoplatelets from an ionic liquid-crystal precursor. *Angewandte Chemie-International Edition* **2004,** *43* (40), 5380-5382.


6.      Getsis, A.; Balke, B.; Felser, C.; Mudring, A. V. Dysprosium-Based Ionic Liquid Crystals: Thermal, Structural, Photo- and Magnetophysical Properties. *Crystal Growth & Design* **2009,** *9* (10), 4429-4437.


7.      Lee, C. K.; Peng, H. H.; Lin, I. J. B. Liquid crystals of N,N '-dialkylimidazolium salts comprising palladium(II) and copper(II) ions. *Chemistry of Materials* **2004,** *16* (3), 530-536.


8.      Lin, I. J. B.; Vasam, C. S. Metal-containing ionic liquids and ionic liquid crystals based on imidazolium moiety. *Journal of Organometallic Chemistry* **2005,** *690* (15), 3498-3512.


9.      Neve, F. Transition metal based ionic mesogens. *Advanced Materials* **1996,** *8* (4), 277-289.

10.     Tosoni, M.; Laschat, S.; Baro, A. Synthesis of novel chiral ionic liquids and their phase behavior in mixtures with smectic and nematic liquid crystals. *Helvetica Chimica Acta* **2004,** *87* (11), 2742-2749.


11.     Pegot, B.; Vo-Thanh, G.; Gori, D.; Loupy, A. First application of chiral ionic liquids in asymmetric Baylis-Hillman reaction. *Tetrahedron Letters* **2004,** *45* (34), 6425-6428.


12.     Truong, T. K. T.; Olivier, N. V. B.; Aupoix, A.; Pegot, B.; Vo-Thanh, G. Chiral Ionic Liquids Derived from (-)-Ephedrine and Carbohydrates: Synthesis, Properties and Applications to Asymmetric Synthesis and Catalysis. *Curr. Org. Synth.* **2012,** *9* (1), 53-64.


13.     Pastre, J. C.; Genisson, Y.; Saffon, N.; Dandurand, J.; Correia, C. R. D. Synthesis of Novel Room Temperature Chiral Ionic Liquids. Application as Reaction Media for the Heck Arylation of Aza-endocyclic Acrylates. *Journal of the Brazilian Chemical Society* **2010,** *21* (5), 821-836.


14.     Prechtl, M. H. G.; Scholten, J. D.; Neto, B. A. D.; Dupont, J. Application of Chiral Ionic Liquids for Asymmetric Induction in Catalysis. *Current Organic Chemistry* **2009,** *13* (13), 1259-1277.


15.     Van Buu, O. N.; Aupoix, A.; Hong, N. D. T.; Vo-Thanh, G. Chiral ionic liquids derived from isosorbide: synthesis, properties and applications in asymmetric synthesis. *New Journal of Chemistry* **2009,** *33* (10), 2060-2072.


16.     Van Buu, O. N.; Aupoix, A.; Vo-Thanh, G. Synthesis of novel chiral imidazolium-based ionic liquids derived from isosorbide and their applications in asymmetric aza Diels-Alder reaction. *Tetrahedron* **2009,** *65* (11), 2260-2265.


17.     Wang, W.-H.; Wang, X.-B.; Kodama, K.; Hirose, T.; Zhang, G.-Y. Novel chiral ammonium ionic liquids as efficient organocatalysts for asymmetric Michael addition of aldehydes to nitroolefins. *Tetrahedron* **2010,** *66* (27-28), 4970-4976.


18.     Wang, Z. M.; Wang, Q.; Zhang, Y.; Bao, W. L. Synthesis of new chiral ionic liquids from natural acids and their applications in enantioselective Michael addition. *Tetrahedron Letters* **2005,** *46* (27), 4657-4660.


19.     Baudequin, C.; Bregeon, D.; Levillain, J.; Guillen, F.; Plaquevent, J. C.; Gaumont, A. C. Chiral ionic liquids, a renewal for the chemistry of chiral solvents? Design, synthesis and

applications for chiral recognition and asymmetric synthesis. *Tetrahedron-Asymmetry* **2005,** *16* (24), 3921-3945.


20.    Li, M.; Ganea, G. M.; Lu, C.; De Rooy, S. L.; El-Zahab, B.; Fernand, V. E.; Jin, R.; Aggarwal, S.; Warner, I. M. Lipophilic phosphonium-lanthanide compounds with magnetic, luminescent, and tumor targeting properties. *Journal of Inorganic Biochemistry* **2012,** *107* (1), 40-46.


21.    Getsis, A.; Balke, B.; Felser, C.; Mudring, A.-V. Dysprosium-Based Ionic Liquid Crystals: Thermal, Structural, Photo- and Magnetophysical Properties. *Crystal Growth & Design* **2009,** *9* (10), 4429-4437.

**CHAPTER 4 THEORETICAL STUDIES OF THE STRUCTRURAL, ELECTRONIC, AND OPTICAL PROPERTIES OF CARBAZOLE-IMIDAZOLIUM BASED GUMBOS**

## 4.1 Introduction

Ionic liquids (ILs) have been studied intensely in various fields and continue to gain the interest of researchers for the last two decades due to their unique and beneficial properties. [1, 2, 3, 4] One of the most attractive properties of ILs is their tunability. There is a tremendous amount of cations and anions, possessing a wide variety of properties that can be combined to form ILs with novel functions.[5, 6, 7, 8] In recent years, our group has introduced an improved class of materials termed GUMBOS (**G**roup of **U**niform **M**aterial **B**ased on **O**rganic **S**alts).[9, 10, 11, 12, 13, 14, 15, 16] GUMBOS are solid organic salts exhibiting a much broader range of the melting points (25–250 $^{\circ}$C) compared to traditional ILs. In addition to retaining the interesting properties of ILs such as tunability, high thermal stability, and non-flammability, GUMBOS have also been reported to have multifaceted applications in biomedical imaging,[17] photovoltaics,[15] chemotherapy,[18] and antimicrobial agents.[9] GUMBOS are of great interest to researchers because many organic molecules can be modified to possess a positive charge (cation) and undergo anion exchange to form GUMBOS. The modification of organic molecules can be achieved by quaternization or covalent linking to positively charged molecules, such as imidazolium, pyrrolidinium.

Carbazole is a π-conjugated heterocyclic compound, which has two benzene rings fused on either side of a five-membered nitrogen-containing ring. The existence of the nitrogen atom as an electron donor in the five-membered ring makes the 2-, 3-, 6-, 7-, and 9-H positions reactive sites, for further chemical modification.[19, 20, 21] Many carbazole derivatives with different structures and substituents have been widely exploited for their electronic and optical properties and they

can be used in optoelectronic devices.[22, 23, 24, 25, 26, 27, 28] Carbazole derivatives are suitable for these applications because of their semi-conductive nature, hole transporting ability, excellent photophysical properties, and high thermal stability. Research has demonstrated that carbazole based compounds with electron donor-π-acceptor (D-A) structures have a large electron delocalization length and allow internal charge transfer (ICT) from an electron-rich moiety to an electron deficient unit.[29, 30, 31] For many years, ICT between a donor and an acceptor has been used to obtain low band conjugated compounds.[19, 20, 32] Based on the ICT principle, many carbazole based derivatives with extended conjugation systems, as well as polymers, were synthesized as efficient emitting materials for OLED applications and as solar spectrum harvester for organic solar cells.[22, 23, 24, 25, 26, 27, 28] Most of the reported carbazole derivatives that have been reported in literature were long conjugated polymers, which led to an increased cost, as a result of the tedious and low-yield synthesis procedures. The studies of carbazole-based small molecules for OLEDs applications in literature are lacking. Previously, a small carbazole based conjugated organic molecule was reported by Tang and VanSlyke[33] for OLEDs. This work showed that small organic compounds can also be efficiently used as optoelectronic materials. Furthermore, research has demonstrated that significant improvement in OLED efficiency can be achieved by employing imidazolium ionic liquids.[34] Due to the significant contribution of imidazolium ionic liquids to optoelectronics and practicality of small organic for optoelectronics studies, a type of new compounds which were based on carbazole and imidazolium have been developed.[35]

Although carbazole cationic compounds have already been synthesized and experimentally characterized,[36, 37] their applications in OLEDs are limited. Recently, our group has synthesized four carbazole-imidazolium based GUMBOS and studied their electronic and optical

properties.[35] The studies found that these GUMBOS can potentially be used as emitters for OLEDs. Since the investigation of carbazole-based GUMBOS for applications in OLEDs is just unfolding, conducting theoretical studies of these GUMBOS is beneficial to provide structure-property relationship information for future design of carbazole-based GUMBOS for specific applications.

The major aim of this study was to combine the theoretical and experimental studies to provide a new strategy to develop low-cost and highly efficient fluorescent materials. The synthesis of carbazole-based GUMBOS is inexpensive, since carbazole-based GUMBOS are small molecules, and are easy to be prepared through a straightforward one-step synthesis procedure, followed by anion exchange. The computer aided design and selection of new dyes will help to save time and expense of materials in laboratory. Theoretical studies are able to provide insights into the dye properties, and predict the optical as well as electronic properties. Thus theoretical calculations are an alternative tool for molecular design, and can be used to guide synthesis of highly efficient dyes.

In this article, we performed theoretical calculations on our recently reported carbazole-imidazolium ($[CI]^+$) based GUMBOS by using density function theory (DFT) and time dependent DFT (TD-DFT) methods. The structures of the studied GUMBOS are outlined in figure 4.1. We discuss, in particular, the geometries of the GUMBOS at the ground state and the effects of anions on the modulation of the frontier molecular orbitals (MOs), ionization potential (IP) energies, electron affinity (EA) energies, and reorganization energies. In addition, we report the simulated absorption spectra in gas phase and in solution. To evaluate the calculation accuracy, the experimental data of GUMBOS were compared with the theoretical results.
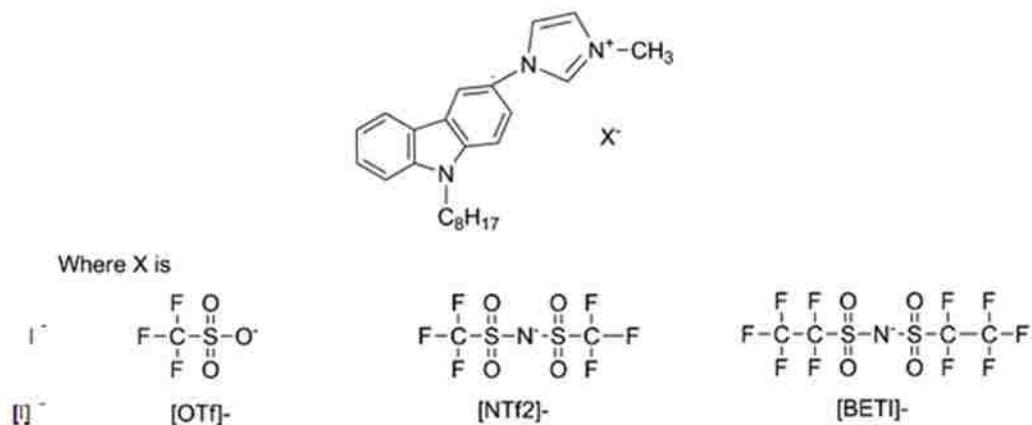
Figure4. 1 Structures of the studied GUMBOS

## 4.2 Computational Methods

The ground-state geometries as well as the ionic structures of four carbazole-imidazolium based GUMBOS were optimized at B3LYP level with the 6-31+G(d,p) or DGDZVP basis set. B3LYP is the most commonly used density function theory (DFT); DGDZVP is the basis set for iodide containing GUMBOS and 6-31+G (d,p) basis set for the other three GUMBOS. The vibrational frequencies and the frontier molecular orbitals were analysed on the optimized structures at the same level. The ionization potentials, electron affinities, reorganizations as well as the HOMO-LUMO gaps of these GUMBOS were calculated using the DFT method based on the optimized geometries. The absorption spectra were carried out using the TD-DFT method based on the optimized ground state structures. Solvent effects were also taken into account by using the polarized continuum model (PCM). All calculations were performed using the advanced computer facilities of high performance computing at Louisiana State University (LSU) with Gaussian 09 program package.

**4.3. Results and Discussion**

**4.3.1 Geometries and Electrostatic Potential Surface of Isolated Ions of GUMBOS**

Inorganic salts often show high melting points because of existence of ionic bonding between cations and anions; ionic liquids (ILs) or low melting point organic salt ion pairs have been considered to form H-bonding instead of ionic bonds.[38, 39] Research has found electrostatic potential surfaces (ESP) are an effective tool for analysing and predicting non-covalent interaction between cations and anions.[40] The structures of the isolated cation and anions of carbazole-imidazolium based GUMBOS as well as ESP properties have been calculated to qualitatively predict the H-bonding interaction within the ion pairs.

The optimized geometry of [CI]$^+$ is shown in Figure 4.2. The cation showed a distorted conformation with two planar segments, which are the imidazolium and carbazole rings. The dihedral angles C11-C6-N1-C2 and C11-C6-N1-C5 of two planar moieties were 52.55 and -126.78. Figure 4.3 shows the electrostatic potential surface maps of cation and anions. As shown in figure 4.3, the highest positively charged region was located around the imidazolium ring, including the C22-H, C21-H, C23-H and side methyl group. Among these high positively charged groups, C22-H had the highest positive charge and is considered to form an H-bond with the anion.

The negative regions of the anions are usually located on the electronegative atoms, such as N and O. The highest negatively charged region of [OTf]$^-$ was on the three O atoms and the three O atoms were equally negative charged. The highest negatively charged region of [BETI]$^-$ was around O and central N atoms and the O and N atoms possessed similar negative charges. The highest negatively charged region of [NTf$_2$]$^-$ was on the central nitrogen atom. Theoretically, H-bonding interaction between the cation and anion occurs at the more positively charged regions

and more negatively charged regions, respectively. It was concluded that the possible H-bond conformations within the GUMBOS ion pairs are I⋯H-C2 for [CI][I], O⋯H-C2 for [CI][OTf], O⋯H-C2 and/or N⋯H-C2 for [CI][BETI], and N⋯H-C2 for [CI][NTf$_2$], respectively.
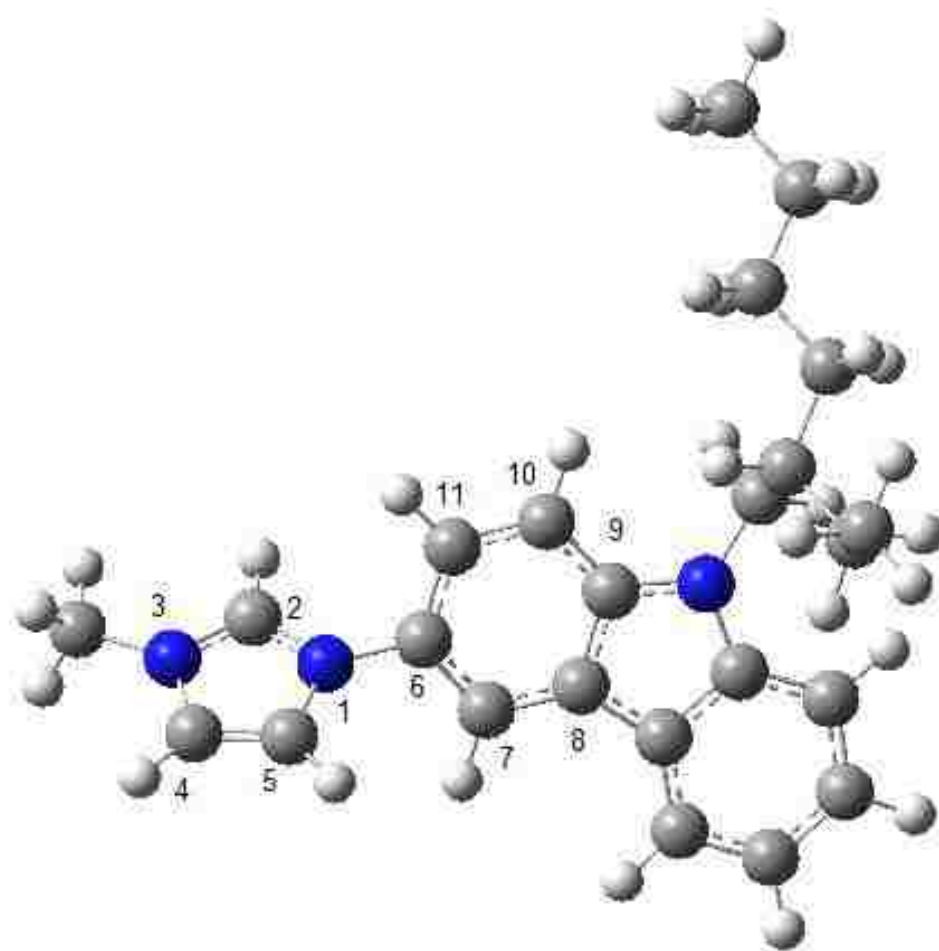


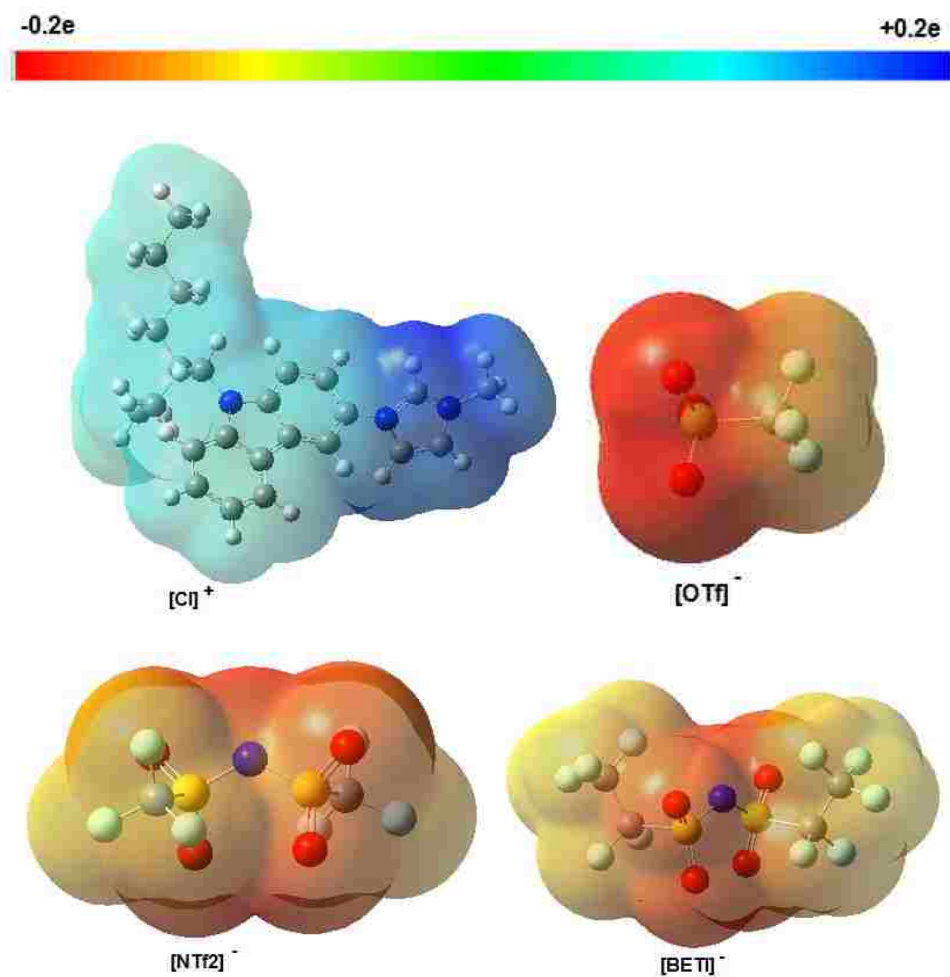Figure4. 2 Optimized geometry of isolated cation [CI]$^+$

Figure4. 3 Electrostatic potential surfaces of the isolated cation and anions (red and blue indicate regions more negative and positive charged, respectively)

### 4.3.2 The Optimized Ground State Geometries of the GUMBOS

The optimized geometries of four GUMBOS are shown in Figure 4.4 and the selected geometry parameters are summarized in Table 4.1. As expected, all the anions were located around the imidazolium ring, where atoms are more negatively charged close to the hydrogen atoms attached to imidazolium ring. Theoretical calculations indicated that there were more than one H-bonds formed between the anions and cation. Here we focus on the H-bonding interaction between C2-H and more negatively charged atoms of anions. The most stable conformation of [CI][BETI] ion pair showed an O···H-C2 H-bond rather than a N···H-C2 H-bond, and the rest of
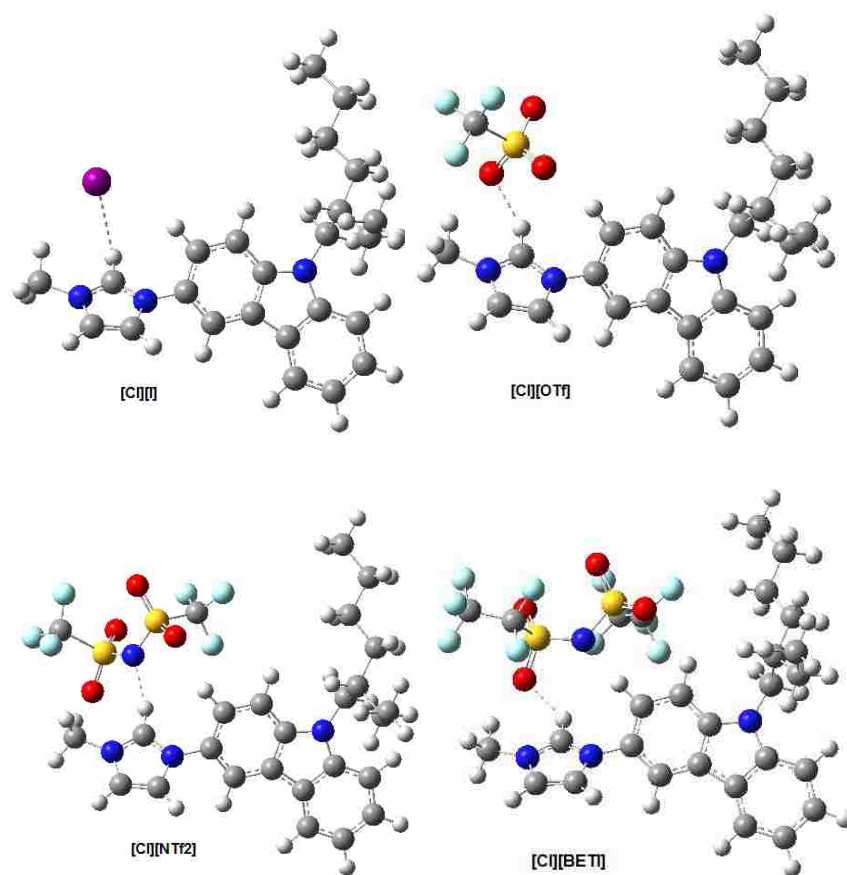
Figure4. 4 Optimized geometries of carbazole-imidazoulium based GUMBOS

Table4. 1 Selected important bond length (Å), bond angle (θ, deg) and dihedral angle (D, deg) of four GUMBOS ion pairs in gas phase

| | $[CI]^+$ | [CI][I] | [CI][OTf] | $[CI][NTf_2]$ | [CI][BETI] |
|---|---|---|---|---|---|
| R(N1-C2) | 1.341 | 1.347 | 1.343 | 1.346 | 1.344 |
| R(C2-N3) | 1.341 | 1.342 | 1.338 | 1.340 | 1.341 |
| r(X··H) | - | 2.764 | 2.042 | 2.07 | 2.172 |
| Θ(X··H-C2) | - | 118.46 | 142.78 | 161.54 | 137.36 |
| D(C2-N1-C6-C11) | 52.55 | 42.28 | 45.06 | 45.0 | 39.47 |
| D(X··H-C2-N3) | - | 70.44 | 25.64 | 32.26 | 17.26 |

GUMBOS ion pairs showed predicted H-bonds in agreement with our previous studies. The order of the H-bond length was found to be [CI][I]( I···H-C2, 2.764 Å) > [CI][NTf2]( N···H-C2, 2.07 Å) > [CI][OTf]( O···H-C2, 2.042 Å), which followed the trend of electronegativity (I=2.5, N=3.0, O=3.5). Although [CI][BETI] formed an O···H-C2 H-bond, its H-bond length was longer than that of [CI][NTf$_2$] but shorter than that of [CI][I]. This moderate H-bond length of [CI][BETI] was due to the collaboration of electronegativity of oxygen atom and the steric hindrance caused by the additional terminal methyl groups of the [BETI]$^-$. It is noticeable that I···H-C2 H-bond showed a much longer length than that of N···H-C2 and O···H-C2; this was due to the large size of iodide ion. The size of the atoms involved in the formation of H-bonds also plays an important role in determining position of the atoms. Atoms with a large size tend to be above the imidazolium ring. The dihedral angle of X···H-C2-N3 showed that iodide ion in [CI][I] was far out of the imidazolium ring plane whereas the H-bonding atoms in the other three GUMBOS were nearly in the plane.

### 4.3.3 Frontier Molecular Orbitals of GUMBOS in the Ground States

Theoretical studies of frontier molecular orbitals and the energy gap between the highest occupied molecular orbital (HOMO) and lowest unoccupied molecular orbitals (LUMO) play a significant role in prediction of the photovoltaic properties of the compound.[41] The electron density contours of the HOMO and LUMO have been plotted using Gaussview and Molden as shown in Figure 4.5. The band gaps between the HOMO and LUMO were obtainedfrom the density function theory (DFT) and time-dependent TDF calculations. The experimental band gap is the lowest transition energy from ground state to the first excited states obtained from the UV-vis absorption spectra. The calculated and experimental energy and energy gaps are listed in Table 4. 2.

As shown in Figure 4.5, the electron densities of the HOMO of [CI][OTf], [CI][NTf$_2$], [CI][BETI] were localized on the carbazole ring, whereas the locations of electron densities of the LUMO were varied with anions. The electron density of the LUMO of [CI][OTf] was largely localized on the carbazole ring, while the LUMO electron cloud of [CI][BETI] was mainly localized on imidazolium ring. For [CI][NTf$_2$], the LUMO electron density was almost equally distributed on both the carbazole and imidazolium rings as well as the bridge. One of the important features of carbazole derivatives is intramolecular charge transfer (ICT) from an electron rich unit to an electron deficient unit. [29, 30, 31] For our GUMOBS, the carbazole ring is the electron donating moiety and imidazolium ring is the electron accepting part. The electron transition from the HOMO localized electron donor (carbazole ring) to LUMO localized on electron acceptor (imidazolium ring) is more likely to lead to intramolecular charge transfer. We can conclude that the possibility of observing ICT occurring between HOMO to HOMO transition from high to low is as follows: [CI][BETI] > [CI][NTf$_2$] > [CI][OTf]. The HOMO of [CI][I] is the non-bonding orbital and the electron cloud was localized on iodide ion due to the presence of lone pair electrons, while the electron density of LUMO was mainly localized on the carbazole ring and shows an anti-bonding nature.

As shown in table 4.2, the calculated energies of the HOMOs of [CI][OTf], [CI][NTf$_2$], [CI][BETI] were -6.14, -6.22 and -6.11 eV, respectively. Since these HOMOs were all localized on the carbazole ring, the differences of the HOMOs were small. The HOMO energy of [CI][I] is about -4.64 eV, which was much higher than those of other three GUMBOS. This is because the HOMO of [CI][I] is a non-bonding orbital, which usually has higher energy than a bonding

[Cl][I] HOMO

[Cl][I] LUMO

[Cl][OTf] HOMO

[Cl][OTf] LUMO

[Cl][NTf2] HOMO

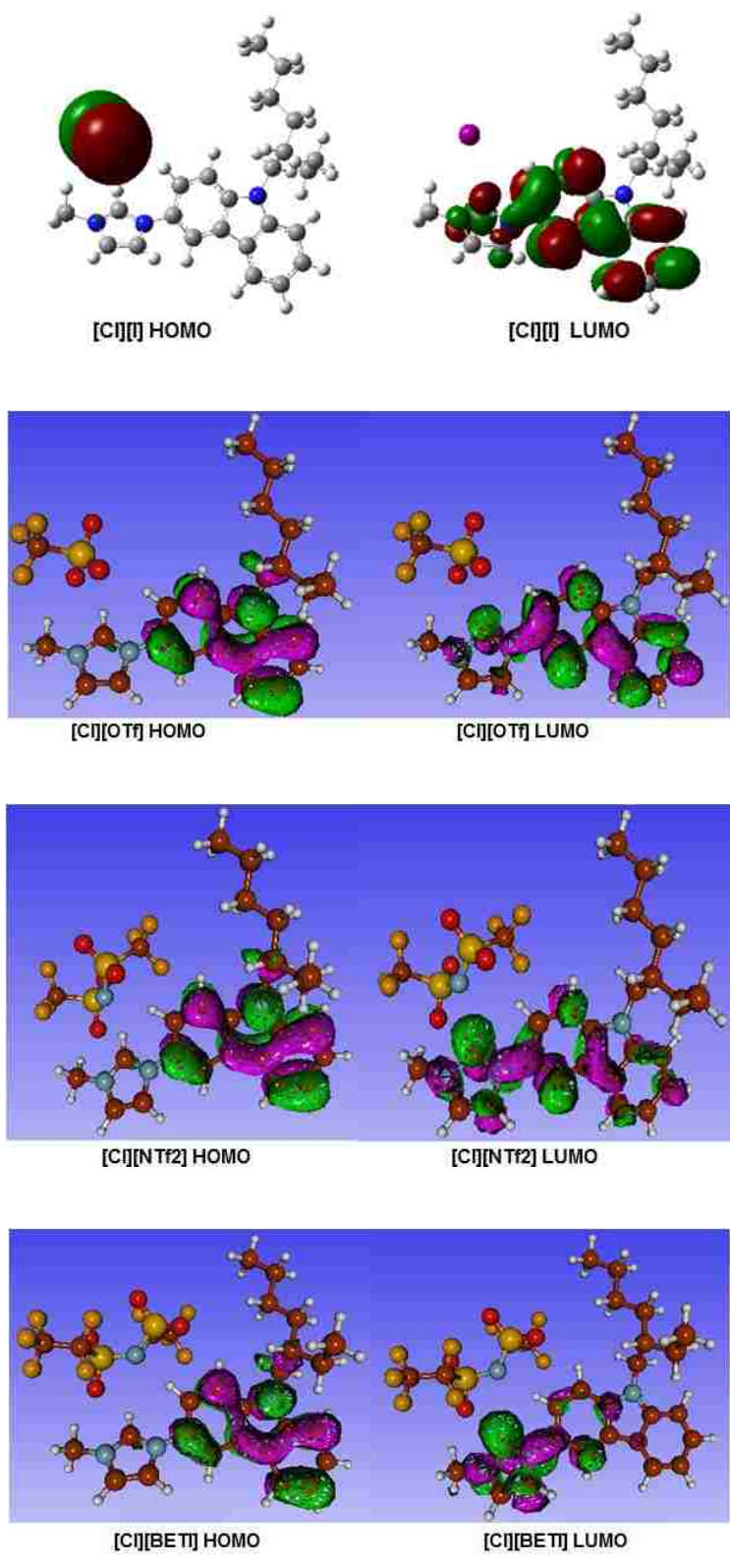[Cl][NTf2] LUMO

[Cl][BETI] HOMO

[Cl][BETI] LUMO

Figure4. 5 Calculated HOMOs and LUMOs structures of GUMBOS in the ground states

orbital. The energy of the LUMOs varied with the electron cloud position change, as a result, the LUMO's energy decreases with more electron density on imidazolium ring. The band gaps between the HOMO and LUMO were obtained by DFT and TDDFT. The results are compared to the experimental data as shown in Table 4.2. The band gaps predicted by the TDDFT method are very close to the experimental results, while the DFT calculations overestimated the HOMO-LUMO band gaps.

Table4.2 HOMO and LUMO energy levels, and band gaps of GUMBOS (in eV) obtained by DFT / TDDFT and experimental

|  | HOMO(DFT) | LUMO(DFT) | $\Delta E_{H-L}$(DFT) | Eg (TD) | Eg[a] |
|---|---|---|---|---|---|
| [CI][I] | -4.64 | -1.68 | 2.96 | 2.43 | 3.42 |
| [CI][OTf] | -6.14 | -1.74 | 4.40 | 3.78 | 3.41 |
| [CI][NTf$_2$] | -6.22 | -1.89 | 4.33 | 3.74 | 3.39 |
| [CI][BETI] | -6.13 | -2.03 | 4.10 | 3.59 | 3.42 |

Eg[a] Band gap is calculated by using onset wavelength

### 4.3.4 Charge Injection and Transport Properties of GUMBOS in the Ground States.

Charge injection and transportation ability of both holes and electrons are crucial parameters to obtain highly efficient OLEDs. Ionization potentials (IP) and electron affinities (EA) are used to evaluate the energy barriers for the holes and electrons injections. IP is the energy barrier of hole ejection, which can be calculated by taking the energy difference between the neutral molecule and molecule that lose one electron. The calculation procedure is illustrated in figure 4.5. IPv is the vertical IP energy obtained by the difference of the energies of both the neutral molecule and the cation at the optimal ground state geometry, whereas the IPa is the adiabatic ionization energy, which was calculated by the energy difference between the neutral molecule

and cation at their optimized geometries. Similarly, we calculated the electron affinity (EV) energy, which was calculated using neutral molecules and molecules that obtain one electron. The first IP and EV of GUMBOS are summarized in Table 5.3. Normally, the lower values of IP lead to easier injection of hole to hole-transporting layers (HTL); and the higher EV values of the electron-transporting layers (ETL), the easier the entrance of an electron from the cathode to the ETL. Similar to the HOMO and LUMO energies, the IP of [CI][OTf], [CI][NTf$_2$], [CI][BETI] were at the same energy level, while the EVs of four GUMBOS increased from 0.76 eV to 1.199 eV. This indicated that the anions of the GUMBOS played a role in the determination of the electron injection ability.

The charge mobility (electron and hole) for organic emitting layer materials is estimated by incoherent hoping model,[42] in which the charge transport rate is given by:

$$k_{\frac{hole}{electron}} = \frac{4\pi^2}{h} \frac{1}{\sqrt{4\pi\lambda_{hole/electron}k_BT}} t^2 \exp\left(-\frac{\lambda_{hole/electron}}{4k_BT}\right)$$

where T is the temperature, $h$ is Planck's constant, k$_B$ is Boltzmann's constants, $t$ is the electronic transfer integral between the donor and acceptor molecules, and $\lambda$ is the reorganization energy for hole or electron transfer between both molecules. Therefore the charge transport rate is determined by $t$ and $\lambda$, and a small $\lambda$ is favourable for obtaining a higher charge transport rate.

As shown in Figure 5.6, the $\lambda_{hole}$ is the sum of $\lambda_+$ and $\lambda_0$ :

$$\lambda_{hole} = \lambda_+ + \lambda_0$$
$$= [E^+(M) - E^+(M^+)] + [E(M^+) - E(M)]$$
$$= [E^+(M) - E(M)] + [E^+(M^+) - E(M^+)]$$

Similarly, the $\lambda_{electron}$ is given by:

$$\lambda_{electron} = \lambda_- + \lambda_0$$

$$= [E^-(M)-E^-(M^-)]+[E(M^-)-E(M)]$$
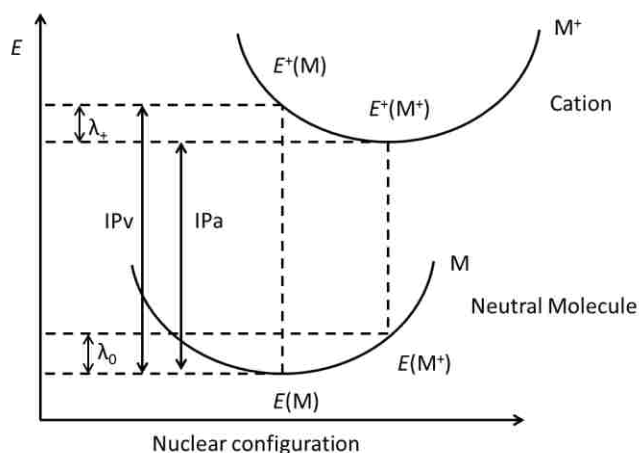$$=[E(M^-)-E^-(M^-)]+[E(M)-E^-(M)]$$



Figure4.6 Ionization potential (IP) and reorganization energy for hole transport

The calculated reorganization energies for both electron or hole transport are listed in Table 4.3. All of the GUMBOS showed lower $\lambda_{hole}$ values than $\lambda_{electron}$. This result demonstrated that the GUMBOS favour hole transport over electron transport. Considering [CI][OTf], [CI][NTf$_2$], [CI][BETI] have much lower $\lambda_{hole}$ values than that of [CI][I], these three GUMBOS can potentially be used for hole transportation applications.

Table4.3 Ionization potentials (IP), electron affinities (EA) and reorganization energies of GUMBOS obtained by DFT/6-31+G(d,p) or DGDZVP

|            | IPv   | IPa   | $\lambda_{hole}$ | EAv   | EAa   | $\lambda_{ele}$ |
|------------|-------|-------|-------|-------|-------|-------|
| [CI][I]    | 6.630 | 6.410 | 0.862 | 0.360 | 0.760 | 1.252 |
| [CI][OTf]  | 7.460 | 7.361 | 0.356 | 0.468 | 0.883 | 1.163 |
| [CI][NTf2] | 7.591 | 7.332 | 0.389 | 0.619 | 1.150 | 1.383 |
| [CI][BETI] | 7.480 | 7.342 | 0.268 | 0.685 | 1.199 | 1.355 |

The suffixes (v) and (a) respectively indicate vertical and adiabatic values

**4.3.5 Optical Properties**

The spectra shown in Figure 4.7 are the observed UV-Vis absorption spectra of [CI][OTf], [CI][NTf$_2$], [CI][BETI] recorded in tetrahydrofuran (THF). The spectrum of [CI][BETI] exhibited high intensity peaks at 238 nm and 275 nm as well as at lower intensity, at 335 and 351 nm. Our previous study has assigned the peaks at 335 and 275 nm to singlet-singlet electronic transitions from the ground state (S$_0$) to the first excited state (S$_1$) and second excited state (S$_2$), respectively.[35] The lower energy electronic transition that occurred at 335 nm is attributed to the S$_0$ to S$_1$ transition. The peak at 335 nm was difficult to observe in [CI][OTf] and [CI][NTf$_2$] solutions due to the weak absorption. The orders of the peak intensity at 335 nm of GUMBOS are [CI][OTf]<[CI][NTf$_2$]<[CI][BETI]. This observation confirms the calculated HOMO and LUMO configuration.

In order to investigate in detail the nature of electronic transitions, the absorption and emission spectra of GUMBOS were calculated using TDDFT methods in both gas phase and in solvent. The calculated results are displayed in Tables 4. 4 to 4.6 and are compared to the experimental data. Table 4.4 lists the vertical electronic transition energies of S$_0$ to S$_1$ and S$_0$ to S$_2$ as well as their oscillator strengths, configuration of orbitals, and experimental results. As shown in Table 4.4, all the transitions, except for S$_0$ to S$_1$ transition of [CI][I], are $\pi$ to $\pi^*$ transitions and agree well with experimental data. The S$_0$ to S$_1$ transition of [CI][I] was a non-bonding to anti-bonding transition and was prohibited with a very low oscillator of 0.0008. Thus, we did not observe the absorption peak at 510 nm calculated by TDDFT.
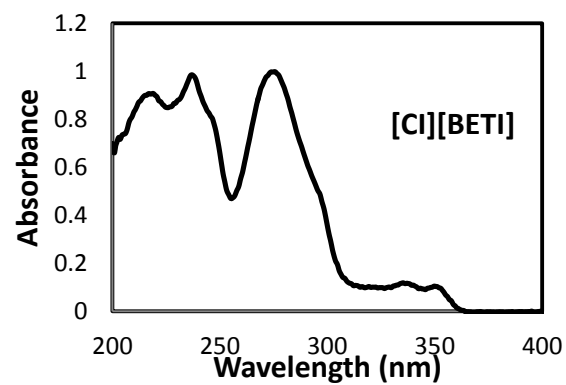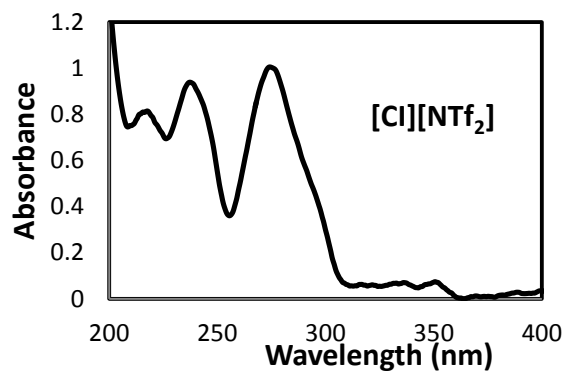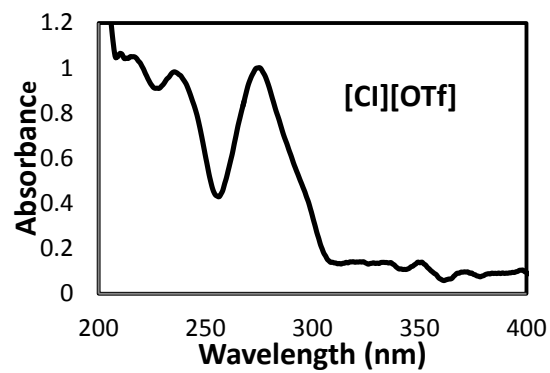
Figure4. 7 Absorption spectra of [CI][OTf], [CI][NTf₂], [CI][BETI] in THF

Table4. 4 The most representative calculated wavelength and transitions of GUMBOS

| | E(eV) | $\lambda$ (nm) | Exp (nm) | $f$ | Main Transition Configuration |
|---|---|---|---|---|---|
| [CI][I] | 2.43 | 510 | - | 0.0008 | HOMO → LUMO |
| | 4.42 | 281 | 275 | 0.437 | HOMO-4 → LUMO |
| [CI][OTf] | 3.78 | 328 | 335 | 0.023 | HOMO → LUMO |
| | 4.34 | 290 | 275 | 0.327 | HOMO-1 → LUMO |
| [CI][NTf$_2$] | 3.74 | 331 | 336 | 0.0306 | HOMO → LUMO |
| | 4.60 | 270 | 275 | 0.1737 | HOMO → LUMO+2 |
| [CI][BETI] | 3.59 | 345 | 336 | 0.0891 | HOMO → LUMO |
| | 4.43 | 280 | 275 | 0.2791 | HOMO-1 → LUMO+1 |

The oscillator strengths of transitions also confirm the experimental results. The oscillator strengths of $S_0$ to $S_1$ transitions of GUMBOS were much lower than those of $S_0$ to $S_2$ transitions, which led to low absorption intensity at 335 nm and high absorption intensity at 275 nm. Furthermore, the oscillator strength trend of $S_0$ to $S_1$ transitions also reflected the peak intensity trend of GUMBOS at 335 nm, which was [CI][OTf]< [CI][NTf$_2$]< [CI][BETI]. The polarizable continuum model (PCM) was used to calculate the solvent effects on absorption spectra. Our calculations were conducted in the methanol, tetrahydrofuran, and dichloromethane. The electronic transitions of $S_0$ to $S_2$ are shown in Table 4.5. All the calculated vertical excitation energies of GUMBOS were lower than those of experimental value in corresponding solvents. The absorption wavelength was related to the polarity of the solvents. For example, methanol has the highest polarity and led to a shortest absorption wavelength for both calculations and experimental studies. This result is in agreement with previous studies.[43]

Table4. 5 Electronic spectra obtained by TD-DFT with solvent MeOH, THF and DCM for GUMBOS at the B3LYP/6-31+G(d,p)/ optimized geometries.

| | Solvent | Cal. Wavelength(nm) | Exp. Wavelength (nm) |
|---|---|---|---|
| [CI][I] | Methanol | 282 | 275 |
| | Tetrahydrofuran | 284 | 275 |
| | Dichloromethane | 284 | 280 |
| [CI][OTf] | Methanol | 284 | 273 |
| | Tetrahydrofuran | 286 | 275 |
| | Dichloromethane | 286 | 280 |
| [CI][NTf$_2$] | Methanol | 285 | 273 |
| | Tetrahydrofuran | 288 | 275 |
| | Dichloromethane | 288 | 281 |
| [CI][BETI] | Methanol | 286 | 273 |
| | Tetrahydrofuran | 290 | 275 |
| | Dichloromethane | 289 | 280 |

## 4.4 Conclusion

In this study, four carbazole-imidazolium based GUMBOS with different anions were theoretically calculated by use of DFT and TDDFT methods. These calculations indicated that anions play an important role in modulation of the electronic and optical properties of GUMBOS by affecting the structure of HOMOs and LUMOs of the GUMBOS at the ground state. The LUMO and HOMO of [CI][BETI] was separately localized on the imidazolium ring and the carbazole ring, and allows $S_0$ to $S_1$ transition to occur, while this transition in other three

GUMBOS was forbidden. The calculated absorption wavelengths correlated well with the experimental data. The calculated reorganization energy for hole/electron pair indicated that these compounds favor the hole transport over electron transport.

**4.5 References**

1.      Parvulescu, V. I.; Hardacre, C. Catalysis in ionic liquids. *Chemical Reviews* **2007,** *107* (6), 2615-2665.

2.      Plechkova, N. V.; Seddon, K. R. Applications of ionic liquids in the chemical industry. *Chemical Society Reviews* **2008,** *37* (1), 123-150.

3.      van Rantwijk, F.; Sheldon, R. A. Biocatalysis in ionic liquids. *Chemical Reviews* **2007,** *107* (6), 2757-2785.

4.      Welton, T. Room-temperature ionic liquids. Solvents for synthesis and catalysis. *Chemical Reviews* **1999,** *99* (8), 2071-2083.

5.      Hayashi, S.; Hamaguchi, H. O. Discovery of a magnetic ionic liquid bmim FeCl4. *Chemistry Letters* **2004,** *33* (12), 1590-1591.

6.      Mallick, B.; Balke, B.; Felser, C.; Mudring, A.-V. Dysprosium room-temperature ionic liquids with strong luminescence and response to magnetic fields. *Angewandte Chemie-International Edition* **2008,** *47* (40), 7635-7638.

7.      Tang, S.; Babai, A.; Mudring, A.-V. Europium-based ionic liquids as luminescent soft materials. *Angewandte Chemie-International Edition* **2008,** *47* (40), 7631-7634.

8.      Zheng, Y.-Z.; Lan, Y.; Wernsdorfer, W.; Anson, C. E.; Powell, A. K. Polymerisation of the Dysprosium Acetate Dimer Switches on Single-Chain Magnetism. *Chemistry-a European Journal* **2009,** *15* (46), 12566-12570.

9.      Cole, M. R.; Li, M.; El-Zahab, B.; Janes, M. E.; Hayes, D.; Warner, I. M. Design, Synthesis, and Biological Evaluation of beta-Lactam Antibiotic-Based Imidazolium- and Pyridinium-Type Ionic Liquids. *Chemical Biology & Drug Design* **2011,** *78* (1), 33-41.

10.     Das, S.; Bwambok, D.; El-Zahab, B.; Monk, J.; de Rooy, S. L.; Challa, S.; Li, M.; Hung, F. R.; Baker, G. A.; Warner, I. M. Nontemplated Approach to Tuning the Spectral Properties of Cyanine-Based Fluorescent NanoGUMBOS. *Langmuir* **2010,** *26* (15), 12867-12876.

11.     Das, S.; de Rooy, S. L.; Jordan, A. N.; Chandler, L.; Negulescu, I. I.; El-Zahab, B.; Warner, I. M. Tunable Size and Spectral Properties of Fluorescent NanoGUMBOS in Modified Sodium Deoxycholate Hydrogels. *Langmuir* **2012,** *28* (1), 757-765.

12.     de Rooy, S. L.; Das, S.; Li, M.; El-Zahab, B.; Jordan, A.; Lodes, R.; Weber, A.; Chandler, L.; Baker, G. A.; Warner, I. M. Ionically Self-Assembled, Multi-Luminophore One-Dimensional Micro- and Nanoscale Aggregates of Thiacarbocyanine GUMBOS. *Journal of Physical Chemistry C* **2012,** *116* (14), 8251-8260.

13.     de Rooy, S. L.; El-Zahab, B.; Li, M.; Das, S.; Broering, E.; Chandler, L.; Warner, I. M. Fluorescent one-dimensional nanostructures from a group of uniform materials based on organic salts. *Chemical Communications* **2011,** *47* (31), 8916-8918.

14.     Dumke, J. C.; El-Zahab, B.; Challa, S.; Das, S.; Chandler, L.; Tolocka, M.; Hayes, D. J.; Warner, I. M. Lanthanide-Based Luminescent NanoGUMBOS. *Langmuir* **2010,** *26* (19), 15599-15603.

15.     Jordan, A. N.; Das, S.; Siraj, N.; de Rooy, S. L.; Li, M.; El-Zahab, B.; Chandler, L.; Baker, G. A.; Warner, I. M. Anion-controlled morphologies and spectral features of cyanine-based nanoGUMBOS - an improved photosensitizer. *Nanoscale* **2012,** *4* (16), 5031-5038.

16.     Lu, C.; Das, S.; Magut, P. K. S.; Li, M.; El-Zahab, B.; Warner, I. M. Irradiation Induced Fluorescence Enhancement in PEGylated Cyanine-Based NIR Nano- and Mesoscale GUMBOS. *Langmuir* **2012,** *28* (40), 14415-14423.

17.     Bwambok, D. K.; El-Zahab, B.; Challa, S. K.; Li, M.; Chandler, L.; Baker, G. A.; Warner, I. M. Near-Infrared Fluorescent NanoGUMBOS for Biomedical Imaging. *Acs Nano* **2009,** *3* (12), 3854-3860.

18.     Magut, P. K. S.; Das, S.; Fernand, V. E.; Losso, J.; McDonough, K.; Naylor, B. M.; Aggarwal, S.; Warner, I. M. Tunable Cytotoxicity of Rhodamine 6G via Anion Variations. *Journal of the American Chemical Society* **2013,** *135* (42), 15873-15879.

19.     Agarwal, N.; Nayak, P. K.; Ali, F.; Patankar, M. P.; Narasimhan, K. L.; Periasamy, N. Tuning of HOMO levels of carbazole derivatives: New molecules for blue OLED. *Synthetic Metals* **2011,** *161* (5-6), 466-473.


20.     Blouin, N.; Leclerc, M. Poly(2,7-carbazole)s: Structure-property relationships. *Accounts of Chemical Research* **2008,** *41* (9), 1110-1119.


21.     Sonntag, M.; Strohriegl, P. Novel 2,7-linked carbazole trimers as model compounds for conjugated carbazole polymers. *Chemistry of Materials* **2004,** *16* (23), 4736-4742.


22.     Brunner, K.; van Dijken, A.; Borner, H.; Bastiaansen, J.; Kiggen, N. M. M.; Langeveld, B. M. W. Carbazole compounds as host materials for triplet emitters in organic light-emitting diodes: Tuning the HOMO level without influencing the triplet energy in small molecules. *Journal of the American Chemical Society* **2004,** *126* (19), 6035-6042.


23.     Ding, J. Q.; Gao, J.; Cheng, Y. X.; Xie, Z. Y.; Wang, L. X.; Ma, D. G.; Jing, X. B.; Wang, F. S. Highly efficient green-emitting phosphorescent iridium dendrimers based on carbazole dendrons. *Advanced Functional Materials* **2006,** *16* (4), 575-581.


24.     Li, J. Y.; Ma, C. W.; Tang, J. X.; Lee, C. S.; Lee, S. T. Novel starburst molecule as a hole injecting and transporting material for organic light-emitting devices. *Chemistry of Materials* **2005,** *17* (3), 615-619.


25.     Lin, S.-L.; Chan, L.-H.; Lee, R.-H.; Yen, M.-Y.; Kuo, W.-J.; Chen, C.-T.; Jeng, R.-J. Highly Efficient Carbazole-pi-Dimesitylborane Bipolar Fluorophores for Nondoped Blue Organic Light-Emitting Diodes. *Advanced Materials* **2008,** *20* (20), 3947-+.


26.     Lu, J.; Xia, P. F.; Lo, P. K.; Tao, Y.; Wong, M. S. Synthesis and properties of multi-triarylamine-substituted carbazole-based dendrimers with an oligothiophene core for potential applications in organic solar cells and light-emitting diodes. *Chemistry of Materials* **2006,** *18* (26), 6194-6203.


27.     Shih, P.-I.; Chiang, C.-L.; Dixit, A. K.; Chen, C.-K.; Yuan, M.-C.; Lee, R.-Y.; Chen, C.-T.; Diau, E. W.-G.; Shu, C.-F. Novel carbazole/fluorene hybrids: Host materials for blue phosphorescent OLEDs. *Organic Letters* **2006,** *8* (13), 2799-2802.


28.     Zhu, W. H.; Hu, M.; Yao, R.; Tian, H. A novel family of twisted molecular luminescent materials containing carbazole unit for single-layer organic electroluminescent devices. *Journal of Photochemistry and Photobiology a-Chemistry* **2003,** *154* (2-3), 169-177.

29.     Castex, M. C.; Olivero, C.; Pichler, G.; Ades, D.; Cloutet, E.; Siove, A. Photoluminescence of donor-acceptor carbazole chromophores. *Synthetic Metals* **2001,** *122* (1), 59-61.


30.     Duan, C.; Chen, K.-S.; Huang, F.; Yip, H.-L.; Liu, S.; Zhang, J.; Jen, A. K. Y.; Cao, Y. Synthesis, Characterization, and Photovoltaic Properties of Carbazole-Based Two-Dimensional Conjugated Polymers with Donor-pi-Bridge-Acceptor Side Chains. *Chemistry of Materials* **2010,** *22* (23), 6444-6452.


31.     Jenekhe, S. A.; Lu, L. D.; Alam, M. M. New conjugated polymers with donor-acceptor architectures: Synthesis and photophysics of carbazole-quinoline and phenothiazine-quinoline copolymers and oligomers exhibiting large intramolecular charge transfer. *Macromolecules* **2001,** *34* (21), 7315-7324.


32.     Bouchard, J.; Belletete, M.; Durocher, G.; Leclerc, M. Solvatochromic properties of 2,7-carbazole-based conjugated polymers. *Macromolecules* **2003,** *36* (12), 4624-4630.


33.     Tang, C. W.; Vanslyke, S. A. ORGANIC ELECTROLUMINESCENT DIODES. *Applied Physics Letters* **1987,** *51* (12), 913-915.


34.     Martin, R.; Teruel, L.; Aprile, C.; Cabeza, J. F.; Alvaro, M.; Garcia, H. Imidazolium ionic liquids in OLEDs: synthesis and improved electroluminescence of an 'ionophilic' diphenylanthracene. *Tetrahedron* **2008,** *64* (27), 6270-6274.


35.     Siraj, N.; Hasan, F.; Das, S.; Kiruri, L. W.; Steege Gall, K.; Baker, G. A.; Warner, I. M. Carbazole-Derived GUMBOS: Solid State Fluorescent Analogs of Ionic Liquids for Potential Applications in Organic-Based Blue Light-Emitting Diodes. *The Journal of Physical Chemistry C* **2014**.


36.     Baran, A.; Plotniece, A.; Sobolev, A.; Vigante, B.; Gosteva, M.; Olkhovik, V. Synthesis and photoluminescent properties of new cationic carbazole-containing luminophores. *Chemistry of Heterocyclic Compounds* **2012,** *48* (2), 287-295.


37.     Liu, X.; Sun, Y.; Zhang, Y.; Zhao, N.; Zhao, H.; Wang, G.; Yu, X.; Liu, H. A Series of Carbazole Cationic Compounds with Large Two-Photon Absorption Cross Sections for Imaging Mitochondria in Living Cells with Two-Photon Fluorescence Microscopy. *Journal of Fluorescence* **2011,** *21* (2), 497-506.

38.     Dong, K.; Zhang, S.; Wang, D.; Yao, X. Hydrogen bonds in imidazolium ionic liquids. *Journal of Physical Chemistry A* **2006,** *110* (31), 9775-9782.


39.     Elaiwi, A.; Hitchcock, P. B.; Seddon, K. R.; Srinivasan, N.; Tan, Y. M.; Welton, T.; Zora, J. A. HYDROGEN-BONDING IN IMIDAZOLIUM SALTS AND ITS IMPLICATIONS FOR AMBIENT-TEMPERATURE HALOGENOALUMINATE(III) IONIC LIQUIDS. *Journal of the Chemical Society-Dalton Transactions* **1995,** (21), 3467-3472.


40.     Zhang, S.; Qi, X.; Ma, X.; Lu, L.; Zhang, Q.; Deng, Y. Investigation of cation-anion interaction in 1-(2-hydroxyethyl)-3-methylimidazolium-based ion pairs by density functional theory calculations and experiments. *Journal of Physical Organic Chemistry* **2012,** *25* (3), 248-257.


41.     Belletete, M.; Morin, J. F.; Leclerc, M.; Durocher, G. A theoretical, spectroscopic, and photophysical study of 2,7-carbazolenevinylene-based conjugated derivatives. *Journal of Physical Chemistry A* **2005,** *109* (31), 6953-6959.


42.     Marcus, R. A. ELECTRON-TRANSFER REACTIONS IN CHEMISTRY - THEORY AND EXPERIMENT. *Reviews of Modern Physics* **1993,** *65* (3), 599-610.


43.     Shi, H.-p.; Xu, L.; Cheng, Y.; He, J.-y.; Dai, J.-x.; Xing, L.-w.; Chen, B.-q.; Fang, L. Experimental and theoretical study of three new benzothiazole-fused carbazole derivatives. *Spectrochimica Acta Part a-Molecular and Biomolecular Spectroscopy* **2011,** *81* (1), 730-738.

# CHAPTER 5 CONCLUSION AND FUTURE WORK

## 5.1 Conclusion

The synthesis, characterization, and theoretical studies of several fluorescent GUMBOS were presented in this dissertation. The first chapter discussed the background information of GUMBOS and fluorescence spectroscopy, and introduced cyanine dyes, lanthanide trivalent ions, carbazole derivatives, ionic liquid crystals, and computational chemistry on GUMBOS. Additionally, analytical techniques used in this dissertation were also discussed.

Synthesis and characterization of PEGylated IR786 GUMBOS were reported in the second chapter, The synthesis of this material was accomplished using a three step protocol: (1) substitution of chloride on the cyclohexenyl ring in the heptamethine chain of IR786 by 6-aminohexanoic acid, (2) grafting of methoxy poly ethyleneglycol (MeOPEG) onto the 6-aminohexanoic acid via an esterification reaction, and (3) anion exchange between [PEG786][I] and lithium bis(trifluoromethylsulfonyl)imide (LiNTf$_2$) or sodium bis(2-ethylhexyl)sulfosuccinate (AOT) in order to obtain PEG786 GUMBOS. It was observed that this PEG786 GUMBOS associates in aqueous solution to form nano- and meso-scale self-assemblies with sizes ranging from 100 to 220 nm. NTf$_2$ and AOT play a significant role in improving the photostability of PEG786 GUMBOS. Irradiation-induced J-aggregation of [PEG786][NTf$_2$] and to some extent in [PEG786][AOT] produced enhanced photostability. In addition, these nano- and meso-scale GUMBOS are also able to resist nonspecific binding to proteins. PEGylation of the original IR786 leads to reduced cytotoxicity. The results demonstrated that these nano and meso-scale GUMBOS are suitable for biomedical imaging applications.

In the third chapter, the synthesis and characterization of multifunctional ionic liquid crystals which possess chiral, fluorescent behaviors, as well as mesomorphic and magnetic properties were reported. (1R, 2S) (-)-N-Methylephedrine ((-)MeEph) was linked with an alkyl chain containing 14, 16, 18 carbons to afford chiral cations and liquid crystalline properties. The anion was a complex ion consisting of trivalent dysprosium ($Dy^{3+}$) and thiocyanate ($SCN^-$), where $Dy^{3+}$ provides fluorescent and magnetic properties. These compounds were found to have melting points below 100℃ and show liquid crystalline behavior by using differential scanning calorimetry (DSC) and hot-stage polarizing optical microscopy (POM). Using an excitation wavelength of 366 nm, the compounds showed two characteristic emission peaks, which are due to the transitions from $^4F_{9/2}$ to $^6H_{15/2}$ and $^4F_{9/2}$ to $^6H_{13/2}$ both in acetonitrile solution and solid states. The emission intensities were sensitive to the phase changes when the compounds experienced the process of phase transitions from solid states to liquid crystal states, then to isotropic liquid states with increased temperature.

The fourth chapter discussed theoretical studies of carbazole-imidazolium based GUMBOS by using DFT and TDDFT calculations. The dihedral angles between the carbazole ring and imidazolium ring were anion dependent. A smaller dihedral angle led to a larger LUMO electron density localizing on the imidazolium ring, which induced an intra-molecular charge transfer. The ionization potential and electron affinity studies suggested these GUMBOS are better hole transport materials than electron transport materials. The TDDFT calculated absorption spectra were in agreement with experimental data.

## 5.2 Future Work

The TDDFT calculations on the excited states of carbazole-imidazolium (CI) based GUMBOS will be performed. TDDFT calculations in this dissertation were conducted on the ground states of CI-based GUMBOS. From these calculations, the absorption spectra were obtained. However, the emission spectra of CI-based GUMBOS are still lacking. To obtain the emission spectra, the TDDFT calculation will be performed on the first excited state, second excited state and any other excited states as needed to find the low-lying excited state. The geometries of the excited states will be optimized and compared to the geometries of the ground states to determine out how the geometry change influences the emission behavior of the CI-based GUMBOS.

# APPENDIX: LETTERS OF COPYRIGHT PERMISSION

## 1. Permission of using published material from American Chemical Society (Langmuir)



**Copyright Clearance Center**  **RightsLink**  Home | Account Info | Help

**ACS Publications**
MOST TRUSTED. MOST CITED. MOST READ.

**Title:** Irradiation Induced Fluorescence Enhancement in PEGylated Cyanine-Based NIR Nano- and Mesoscale GUMBOS

**Author:** Chengfei Lu, Susmita Das, Paul K. S. Magut, Min Li, Bilal El-Zahab, and Isiah M. Warner

**Publication:** Langmuir

**Publisher:** American Chemical Society

**Date:** Oct 1, 2012

Copyright © 2012, American Chemical Society

Logged in as:
Chengfei Lu
Account #:
3000741986

LOGOUT

### PERMISSION/LICENSE IS GRANTED FOR YOUR ORDER AT NO CHARGE

This type of permission/license, instead of the standard Terms & Conditions, is sent to you because no fee is being charged for your order. Please note the following:

- Permission is granted for your request in both print and electronic formats, and translations.
- If figures and/or tables were requested, they may be adapted or used in part.
- Please print this page for your records and send a copy of it to your publisher/graduate school.
- Appropriate credit for the requested material should be given as follows: "Reprinted (adapted) with permission from (COMPLETE REFERENCE CITATION). Copyright (YEAR) American Chemical Society." Insert appropriate information in place of the capitalized words.
- One-time permission is granted only for the use specified in your request. No additional uses are granted (such as derivative works or other editions). For any other uses, please submit a new request.

2. Permission of using published material from Springer (Basic Research in Cardiology)

This is a License Agreement between Chengfei Lu ("You") and Springer ("Springer"). The license consists of your order details, the terms and conditions provided by Springer, and the payment terms and conditions.

Get the printable license.

| | |
|---|---|
| License Number | 3420830634747 |
| License date | Jul 02, 2014 |
| Licensed content publisher | Springer |
| Licensed content publication | Basic Research in Cardiology |
| Licensed content title | Near-infrared fluorescent probes for imaging vascular pathophysiology |
| Licensed content author | Jan Klohs |
| Licensed content date | Jan 1, 2008 |
| Volume number | 103 |
| Issue number | 2 |
| Type of Use | Thesis/Dissertation |
| Portion | Figures |
| Author of this Springer article | No |
| Original figure numbers | Fig.1 |
| Title of your thesis / dissertation | SYNTHESIS, CHARACTERIZATION, AND THEORETICAL STUDIES OF FLUORESCENT GUMBOS AND NANOGUMBOS |
| Expected completion date | Aug 2014 |
| Estimated size(pages) | 126 |
| Total | 0.00 USD |

3. Permission of using published material from Elsevier (Synthetic Metals)

Dear Mr. Chengfei Lu,

Thank you for placing your order through Copyright Clearance Center's RightsLink service. Elsevier has partnered with RightsLink to license its content. This notice is a confirmation that your order was successful.

Your order details and publisher terms and conditions are available by clicking the link below:
http://s100.copyright.com/CustomerAdmin/PLF.jsp?ref=61c3afb0-4747-4b8f-a2b9-5fcc6321b046

**Order Details**
Licensee: Chengfei Lu
License Date: Jul 1, 2014
License Number: 3420370639683
Publication: Synthetic Metals
Title: Tuning of HOMO levels of carbazole derivatives: New molecules for blue OLED
Type Of Use: reuse in a thesis/dissertation
Order Reference: 123456
Total: 0.00 USD

To access your account, please visit https://myaccount.copyright.com.

Please note: Online payments are charged immediately after order confirmation; invoices are issued daily and are payable immediately upon receipt.

To ensure that we are continuously improving our services, please take a moment to complete our customer satisfaction survey.

B.1:v4.2

4. Permission of using published material from Royal Society of Chemistry (Chemical Communication)

## Thank You For Your Order!

Dear Mr. Chengfei Lu,

Thank you for placing your order through Copyright Clearance Center's RightsLink service. Royal Society of Chemistry has partnered with RightsLink to license its content. This notice is a confirmation that your order was successful.

Your order details and publisher terms and conditions are available by clicking the link below:
http://s100.copyright.com/CustomerAdmin/PLF.jsp?ref=4cc4e899-8581-4f4f-a24b-9f4531bb434c

Order Details
Licensee: Chengfei Lu
License Date: Apr 9, 2014
License Number: 3364860597502
Publication: Chemical Communications (Cambridge)
Title: Modelling room temperature ionic liquids
Type Of Use: Thesis/Dissertation
Total: 0.00 USD

To access your account, please visit https://myaccount.copyright.com.

Please note: Online payments are charged immediately after order confirmation; invoices are issued daily and are payable immediately upon receipt.

To ensure that we are continuously improving our services, please take a moment to complete our customer satisfaction survey.

B.1:v4.2

116

5. Permission of using published material from Royal Society of Chemistry (Chemical Society Reviews)

6. Permission of using published material from Multidisciplinary Digital Publishing Institute (Materials)

*Review*

## Thermotropic Ionic Liquid Crystals

**Kirill V. Axenov** * ✉ **and Sabine Laschat** * ✉

+ Authors' affiliation

# VITA

Chengfei Lu was born in Meishan, Sichuan, People's Republic of China, to Guiqing Lu and Zhongying Tao. Chengfei attended Gongyi and Qingfeng elementary schools prior to enrollment at Tudi middle school. Chengfei graduated from Meishan First High School in 1997. He received his Bachelor of Science Degree in Chemistry in July 2001 from East China Normal University. From 2001 to 2003, he worked in the Pharmacy Department of Chongqing Medical University as an Assistant Experimentalist. In 2003, he was admitted into a master's program in pharmaceutics in Shanghai Jiao Tong University. During his three years study, he participated in a research project which involved development of linear and star-shaped poly(ethylene glycol)-block–poly - ($\varepsilon$-caprolactone) copolymers (PEG-PCL copolymers) for the application of micellar drug delivery. From 2006 to 2008, Chengfei worked in the Pharmacy Department of Chongqing Medical University as an Experimentalist. He began his doctoral studies in analytical chemistry in August 2008 at Louisiana State University (LSU) under the mentorship of Prof. Isiah. M. Warner. His research interest was development and theoretical studies of fluorescent GUMBOS. Alongside his doctoral studies, Chengfei pursued master in applied statistics from Louisiana State University in August 2012. Chengfei graduated with the degree of Doctor of Philosophy in chemistry and Master of Applied Statistics from Louisiana State University in May 2014.